

INFORMATION TO USERS

This manuscript has been reproduced from the microfilm master. UMI films the text directly from the original or copy submitted. Thus, some thesis and dissertation copies are in typewriter face, while others may be from any type of computer printer.

The quality of this reproduction is dependent upon the quality of the copy submitted. Broken or indistinct print, colored or poor quality illustrations and photographs, print bleedthrough, substandard margins, and improper alignment can adversely affect reproduction.

In the unlikely event that the author did not send UMI a complete manuscript and there are missing pages, these will be noted. Also, if unauthorized copyright material had to be removed, a note will indicate the deletion.

Oversize materials (e.g., maps, drawings, charts) are reproduced by sectioning the original, beginning at the upper left-hand corner and continuing from left to right in equal sections with small overlaps. Each original is also photographed in one exposure and is included in reduced form at the back of the book.

Photographs included in the original manuscript have been reproduced xerographically in this copy. Higher quality 6" x 9" black and white photographic prints are available for any photographs or illustrations appearing in this copy for an additional charge. Contact UMI directly to order.



University Microfilms International
A Bell & Howell Information Company
300 North Zeeb Road, Ann Arbor, MI 48106-1346 USA
313/761-4700 800/521-0600



Order Number 9325041

**Vibrational spectroscopic studies of olivines, pyroxenes, and
amphiboles at high temperatures and pressures**

Mohanan, Kakkala, Ph.D.

University of Hawaii, 1993

U·M·I
300 N. Zeeb Rd.
Ann Arbor, MI 48106



VIBRATIONAL SPECTROSCOPIC STUDIES OF OLIVINES, PYROXENES,
AND AMPHIBOLES AT HIGH TEMPERATURES AND PRESSURES

A DISSERTATION SUBMITTED TO THE GRADUATE DIVISION OF THE
UNIVERSITY OF HAWAII IN PARTIAL FULFILLMENT OF THE
REQUIREMENTS FOR THE DEGREE OF

DOCTOR OF PHILOSOPHY
IN GEOLOGY AND GEOPHYSICS
MAY 1993

BY

Kakkala Mohanan

Dissertation Committee:

Shiv K. Sharma, Chairperson
George Walker
David Muenow
Paul Lucey
Edward Scott

To Lekshmi, my Mother

with love

ACKNOWLEDGEMENTS

I would like to take this opportunity to thank the people who have assisted me in various aspects of this dissertation. I wish to express my sincere thanks to Dr. Shiv K. Sharma, my committee chairperson, who has helped me very much through out my studies by giving me direction in my search and financially supporting me for making my stay pleasant. I consider myself very fortunate to work under/with him that I learned the true art of searching for the scientific truth. I am grateful to Dr. David Muenow for supplying me with mineral samples, and allowing me to use his laboratory equipment. I want to covey my gratitude to Dr. George Walker and Dr. Paul Lucey for their assistance and suggestions. I am indebted to Dr. L. C. Ming for serving in my committee and his invaluable critical comments on my research and manuscripts. I like to extend my special thanks to Dr. Edward Scott for agreeing to serve on my committee on a short notice. I am also thankful to Dr. Scott Rowland for his assistance in preparing my slides related to my dissertation. My appreciations go to shouyu Wang for helping me to conduct high pressure research in the Raman Lab and David Foss for doing the Microprobe analysis on my samples. My special thanks to Ms. Joann Sinton for her invaluable help and patience in preparing samples for infrared measurements. Also, I like to acknowledge Dr. Thomas Cooney and Diane Anderson for their creative suggestions on my manuscripts. Finally, I wish to offer my thanks to Eric Miller and Joe Urmos for their suggestions on my technical writings.

I want to thank my parents for their support, encouragement and patience for through out my studies. I also want to thank my brother Gopal and his wife, Vijay, for their support. Finally, I wish to express my sincere thanks to Ann Palmer, Janet Palmer and Barbara Duke for their support and love whenever I needed.

Abstract

Structural properties of olivines, pyroxenes, and amphibole crystals are investigated using Raman and infrared spectroscopy. Raman spectra of olivine crystals are measured along the forsterite-monticellite solid solution series in the 100-1200 cm⁻¹ region. In the spectrum of Fo, strong Si-O- symmetric stretching bands appear at 824 and 855 cm⁻¹, and a medium intensity anti-symmetric Si-O- stretching band appears at 964 cm⁻¹. These bands show a systematic frequency variation with composition and are attributed to decreased distortion of SiO₄ tetrahedra. The mixing characteristics of v₁ and v₃ modes in orthosilicates were found to strongly depend on the ratio of average inter-(O-O) to (Si-O) bond lengths. In the low-frequency region of the spectra, Fo-rich compositions show progressive broadening of the bands with the addition of up to 16 wt% monticellite and is attributed to increasing positional disorder caused by the substitution of large calcium ions into the M1 octahedral sites.

Structural properties of several pyroxene crystals have been investigated using Raman spectroscopy at various temperatures. The strong band around 700 cm⁻¹ appears in all pyroxenes, is the characteristic feature of single chain pyroxenes and it increases with the addition of smaller cations. Intensity ratio of Si-O- to stretching modes to Si-O-Si symmetric stretching mode suggests that the Si-O--M (M=cation) bonds in diopside and hedenbergite are more in ionic character than spodumene and jadeite. The high-temperature spectra of spodumene indicates that above 700 C, it's structure becomes metastable. Ortho-to-proto phase transition in enstatite takes place around 1320 K as indicated by the appearance of a new band at 98 cm⁻¹. High temperature results indicate that the force constants of the silicate bonds in pyroxene decrease with temperature.

Raman and infrared spectra of cummingtonite, actinolite, and several Ti-rich amphibole crystals from various locations in the United States have been measured in the 100-4000 cm⁻¹ region. Raman spectra of cummingtonite and actinolite shows a strong symmetric stretching band at 662 and 671 cm⁻¹, respectively. The Raman bands above 1000 cm⁻¹ are assigned to the anti-symmetric stretching of the Si-O-Si bonds and in the hydroxyl region up to four bands appear at about 3675 cm⁻¹ indicating different cation environment of hydroxyl ions in these two minerals. In Ti-rich amphibole crystals the symmetric and anti-symmetric bands appear broad and weak and they vary in their frequencies and intensities with MgO and TiO content respectively. In the hydroxyl stretching region both Raman and IR spectra have only one broad band and its intensity varies linearly with the total H₂O and shifts toward high-frequency with increasing MgO content. With the present experimental setup up to 0.5 wt% water in minerals can be detected. The presence of broad band indicates random distribution of cation in M1, M2, M3, M4, and A sites resulting in increased positional disorder.

TABLE OF CONTENTS

ACKNOWLEDGEMENTS	iv
ABSTRACT	v
LIST OF TABLES	ix
LIST OF FIGURES	x
 Chapter 1 INTRODUCTION	 1
1.1 Raman and infrared spectroscopy	3
1.2 Study of olivines	4
1.3 Study of pyroxenes	5
1.4 Study of amphiboles	6
 Chapter 2 EXPERIMENTAL TECHNIQUES IN VIBRATIONAL SPECTROSCOPY	 8
2.1 Infrared spectroscopy	10
2.2 Fundamental theory of infrared spectroscopy	11
2.3 Fourier transform infrared (FT-IR) spectroscopy	13
2.4 Advantages of using FT-IR over conventional spectroscopy	15
2.5 Raman Spectroscopy	15
2.6 Theory of spontaneous (normal) Raman effect	16
2.7 Effect of temperature on the intensities of Raman bands	18
2.8 Polarization studies	20
2.9 Multichannel micro-Raman spectroscopy	23
2.10 Calibration of the micro-Raman spectrometer	23
2.11 Advantages of micro-Raman spectroscopy	27
2.12 High-temperature Raman studies	38
2.13 High-pressure Raman and ir studies	38
2.14 Low-temperature micro-Raman studies	44
 Chapter 3 A RAMAN AND INFRARED STUDY OF THE FORSTERITE- MONTICELLITE SOLID SOLUTION SERIES	 47
3.1 Experimental methods	48
3.2 Factor group analysis	49
3.3 Results and discussion	55
3.3.1 High-frequency Raman spectra	55
3.3.2 Low-frequency Raman spectra	66
 3.4 High pressure studies of Fo-Mo series using Raman and infrared spectroscopy	 72
3.5 Experimental details	73
3.6 Sample description	73
3.7 Results and Discussions	74
3.7.1 Raman spectra	74
3.7.2 Infrared spectra	80

3.8	Low temperature Raman spectral studies	85
3.9	Experimental setup	85
3.10	Results and discussion	86
Chapter 4:	RAMAN STUDIES OF PYROXENES	92
4.1	Experimental setup	96
4.2	Theoretical calculations	97
4.3	Results and discussion	97
4.4	High-temperature Raman spectra of diopside and α -spodumene	103
4.5	Results and discussion	103
4.6	High temperature studies of enstatite	109
4.7	Results and discussion	109
Chapter 5:	RAMAN AND IR SPECTROSCOPIC STUDY OF AMPHIBOLE CRYSTALS	136
5.1	Experimental methods	138
5.2	Description of the samples	139
5.3	Theoretical analysis	141
5.4	Results and Discussion	143
5.4.1	Raman spectra of amphibole crystals	143
5.4.2	Infrared spectra of amphibole crystals	158
5.5	High pressure Raman spectra of cummingtonite	163
5.6	Suggestions for future work	167
APPENDIX	Alignment of the micro-Raman spectrometer	168
REFERENCES	171

LIST OF TABLES

Table 1: Description of various spectroscopic techniques, their frequency range, and the information gained	9
Table 2: Vibrational lines indene used for the calibration of the spectrometer	32
Table 3: Some frequently used laser lines and their corresponding wave numbers in air	33
Table 4: Plasma lines from an Ar+ laser used for spectrometer calibration	34
Table 5: Plasma lines of a Kr+ laser	35
Table 6: Plasma lines of Helium-Neon laser	36
Table 7: Table showing the space group, ions, sites, various Raman and infrared modes in olivine crystal structure	51
Table 8: Experimentally observed Raman bands in various olivines, their mode assignments and Gruenesian parameters	52
Table 9: Observed Raman frequencies of the Fo-Mo solid solution series	53
Table 10: Table containing observed Raman frequencies, bond length, and bond ratio	62
Table 11: List of the coefficients of the linear fit obtained for the high pressure data of the FO6% sample	78
Table 12: Table containing pressure derivatives and Gruenesian parameters for the olivines	83
Table 13: The curve fitted results for enstatite and clino-enstatite Raman bands	126
Table 14: Name of the amphiboles, their thickness, chemical composition and the observed vibrational bands	140
Table 15: Observed Raman bands for the amphiboles in the 100-1200 cm ⁻¹ region	150

LIST OF FIGURES

Figure 1:	Energy level diagram representing Raman and infrared transitions	12
Figure 2:	Schematic diagram showing components of a Michelson interferometer	14
Figure 3:	Typical interferogram formed by an interferometer	14
Figure 4:	Stoke and anti-Stoke lines of carbon tetrachloride (CCl_4)	19
Figure 5:	Experimental configuration for depolarization measurements	21
Figure 6:	Depolarized (trace 1) and polarized (trace 2) spectra of carbon tetrachloride (CCl_4)	22
Figure 7:	Block diagram of the micro-Raman setup utilized in the Department of Geophysics, at the University of Hawaii	24
Figure 8:	Block diagram of the pre-monochromator showing the optical path taken by the laser	25
Figure 9:	Spectrum of calcite in the 100-1200 cm^{-1} region	28
Figure 10:	Raman spectrum of indene used for calibration of the spectrometer	29
Figure 11:	Plasma lines from an Ar ⁺ laser for the calibration	30
Figure 12:	Block diagram of the setup used for the plasma line calibration	31
Figure 13:	Furnace used for conducting high temperature Raman spectroscopy experiments	39
Figure 14:	Schematic diagram showing optical path in a Diamond Anvil Cell (DAC) used for conducting high pressure Raman spectroscopy experiments	40
Figure 15:	Details of the DAC showing position of the sample, ruby, and metal gasket	42
Figure 16:	Systematic variation of the fluorescence line R1 of the ruby with respect to the applied pressure	43
Figure 17:	Various components used for the low temperature Raman scattering experiments	46
Figure 18:	Crystal structure of the Pbnm type olivine structure showing the tetrahedral and octahedral sites	50

Figure 19:	Miscibility gap at 5 kbar and 10 kbar in the forsterite-monticellite system	54
Figure 20:	Raman spectra of the forsterite - monticellite (Fo100%-Fo6%) solid solution series in the 100-1000 cm ⁻¹ region	56
Figure 21:	a) Schematic diagram showing the position of silicon with respect to the various oxygen and the cations in the M1 and M2 octahedral coordinations. b) This diagram illustrates the symmetric and anti-symmetric stretching of the silicon and oxygen atoms in an isolated SiO ₄ tetrahedral unit	57
Figure 22:	Details of the Raman spectra of Fo-Mo solid solution series in the high frequency region (700-1000 cm ⁻¹)	58
Figure 23:	Plot of the high frequency bands vs unit cell volume.	59
Figure 24:	Plot of the three major Raman modes of three olivines with respect to the corresponding Si-O bond lengths	63
Figure 25:	The 855 cm ⁻¹ of Fo100% band is fitted to a parabolic curve	64
Figure 26:	Coupling behavior of the high-frequency modes (A _g and B _{1g} modes) in olivine crystals	65
Figure 27:	The dependence of high frequency bands in olivines on the sum of the ratio of Si-O bond lengths to the Si-O(1) bond length and the ratio of inter-tetrahedralbond lengths	67
Figure 28:	Raman spectra of the forsterite-monticellite SS series in the low frequency region (100-700 cm ⁻¹)	69
Figure 29:	Behavior of the half width of two low frequency Raman bands 434 cm ⁻¹ and 544 cm ⁻¹ bands	71
Figure 30:	Unit cell volume of natural olivine in the Mg ₂ SiO ₄ .Fe ₂ SiO ₄ joint	71
Figure 31:	High-pressure Raman spectra of the Fo6% in the high frequency region (700-1100 cm ⁻¹) between 1 bar and 167 kbar.	75
Figure 32:	High-pressure Raman bands of the Fo6% in the low- frequency region (100-700 cm ⁻¹)	76
Figure 33:	Plot of the variation of Raman frequency with pressure	77
Figure 34:	Five ir spectra of Fo6%, between pressure 1 bar and 197 kbar, in the 450-1200 cm ⁻¹ region	81
Figure 35:	Plot of the variation of IR frequency with pressure	82

Figure 36:	Low-temperature (293-100 K) Raman spectra of Fo6% in the 100-700 cm ⁻¹ region	87
Figure 37:	Low-temperature (75-35 K) Raman spectra of Fo6% in the 100-700 cm ⁻¹ region	88
Figure 38:	Variation of the Raman frequency with temperature(<273K)	89
Figure 39:	Variation of band width of the 390 cm ⁻¹ peak with temperature	90
Figure 40:	Schematic diagram of four pyroxene crystal structures belonging to four different space groups	93
Figure 41:	The crystal structure of C2/c pyroxene projected on to the (110) plane	95
Figure 42:	The Raman spectra of acmite, diopside, and hedenbergite at ambient conditions	98
Figure 43:	The Raman spectra od CaTs, Jadeite, and spodumene crystal at ambient conditions	99
Figure 44:	Plot of the ratio of anti-symmetric (Si-O-) to symmetric (Si-O-Si) stretch vs Si-O bond length in pyroxenes	102
Figure 45:	The Raman spectra of diopside between 298 K and 773 K	104
Figure 46:	Variation of the Raman frequency vs temperature in diopside	105
Figure 47:	Variation of the Raman frequency with temperature in α -spodumene	107
Figure 48:	The Raman spectra of proto-enstatite, clino-enstatite, and ortho-enstatite at 293 K	110
Figure 49:	The high-temperature Raman spectra of ortho-enstatite at high-temperature	112
Figure 50:	The plot of the variation of Raman frequency in ortho-enstatite with temperature	113
Figure 51:	This plot indicates the transition of MgSiO ₃ from the low-clino-enstatite to the high-clino-enstatite	114
Figure 52:	The Raman spectra of ortho-enstatite between 293 K and 1273 K	115
Figure 53:	The Raman spectra of ortho-enstatite between 293 K and 1273 K	116

Figure 54:	The curve fitted spectra of enstatite at various temperatures in the 600-750 cm ⁻¹ region (293-873 K)	117
Figure 55:	The curve fitted spectra of enstatite at various temperatures in the 600-750 cm ⁻¹ region (1003-1273 K)	118
Figure 56:	Stretching frequencies due to the Si-O ⁻ shows linear variation in the Raman frequency with temperature	120
Figure 57:	The band width of the stretching modes also show linear trend in its changes with temperature	121
Figure 58:	A plot of the behavior of the 666.5 cm ⁻¹ and 688.9 cm ⁻¹ bands with temperature	122
Figure 59:	The variation of band width of the symmetric stretching modes	123
Figure 60:	The transition from the ortho-to-clino enstatite is marked by a sudden change in the Raman frequency 85 cm ⁻¹	124
Figure 61:	Band width of peak 85 cm ⁻¹ . It is fitted to a polynomial equation	125
Figure 62:	The Raman spectra of clino-enstatite at high temperature	127
Figure 63:	The Raman spectra of clino-enstatite at high temperature	128
Figure 64:	The Si-O ⁻ stretching bands in the 950-1000 cm ⁻¹ region is resolved with the help of a curve fitting program (273-473 K)	129
Figure 65:	The Si-O ⁻ stretching bands in the 950-1000 cm ⁻¹ region is resolved with the help of a curve fitting program (1003-1273 K).	130
Figure 66:	Variation of the Raman frequency of resolved peaks in the high frequency region	132
Figure 67:	The band width of high frequency bands show linear variation	133
Figure 68:	The variation of Si-O ⁻ stretching frequencies with temperature	134
Figure 69:	In the high-frequencies region, the 1015 cm ⁻¹ peak shows a large increase in the band width with temperature compared to the 1037 cm ⁻¹ peak, which varies quite linear	135
Figure 70:	Crystal structure of the monoclinic C2/c amphibole projected on to the a axis	142
Figure 71:	Detailed schematic diagram showing the location and direction of OH ⁻ vector with respect to the M1 and M3 cations.	144

CHAPTER 1

INTRODUCTION

In this study vibrational spectroscopy is utilized for investigating the structural and vibrational spectral properties of three different groups of silicate minerals, e.g. olivines, pyroxenes, and amphiboles, at ambient conditions, low-temperature as well as at high temperature and high pressure. Silicate minerals and melts exist in the interior of the earth under extreme physical conditions and have different thermodynamical and physical properties. For earth scientists it is important to know the properties of relevant minerals as accurately as possible to provide a better understanding of the earth's interior.

Written documentation on study of the minerals dates back to 372 B.C., by the Greek philosopher Theophrastus (Klein and Huburt, 1977). The first mile-stone in mineralogy was laid by Nicolas Steno in 1669 for his studies on the physical properties of minerals, especially the angles between different faces (Klein and Hurlbut, 1977). The invention of the goniometer in 1809 by Wollaston permitted highly accurate studies of crystal phases. However, the most important contributions to mineralogy were due to the invention of the X-ray diffractometer by Max Von Laue in 1912.

Since the invention of X-ray diffraction methods, structures of hundreds of minerals have been studied. During the last twenty years structures of various rock forming minerals have been examined at elevated temperatures up to 1325 K. Minerals investigated in this way include olivines, pyroxenes and feldspars (Brown and Prewitt, 1973; Hazen, 1976; Smyth and Hazen, 1973; Lager and Meagher, 1978; Camerron, et. al., 1973; Sueno, et. al., 1976; Prewitt, 1976). These studies have helped us to understand the cation environments in the crystal. However, despite great successes,

there are several unanswered questions. For, example, the effect of high temperature on bonding forces in minerals is yet to be understood. Cameron, et. al., (1973) have shown that in pyroxenes the octahedrally coordinated M-O bonds expand significantly more than the tetrahedrally coordinated T-O bonds (where T = Si⁴⁺ or Al³⁺). It has been suggested on the basis of high temperature X-ray diffraction data that the T-O bond length decreases slightly with temperature. Winter et. al., (1977) have, however, pointed out that the apparent slight decrease in the bond length is an artifact due to the errors in the bond length calculations caused by the thermal motion of the atoms. Furthermore, molecular dissociation, heat content, and heat capacity cannot be explained with the harmonic vibrational approach alone. Anharmonic vibrations of different atoms in the crystal structure lead to differential thermal expansion. Therefore, more realistic explanations of the physical properties demand anharmonic approach. Vibrational spectroscopy, especially Raman spectroscopy, at elevated temperatures could provide more accurate and valuable information on the bond characteristics (bond lengths, bond angles, etc.). Also, half widths at half maxima of the Raman bands give information about the anharmonicity of the thermal vibrations at high temperatures. Therefore, the inconsistency in the bond parameters observed in the X-ray diffraction data, and cation coordination and its environment have both to be understood in greater depth. Above all, the thermodynamic data such as heat capacity and entropy, have to be accurately determined in order to model the earth's interior. These cannot be achieved by X-ray diffraction methods alone. Vibrational spectroscopy, on the other hand, can be used to determine all of the above parameters not only at room temperature, but at high temperature and high pressure.

The following sections summarize the contents of each chapter of this thesis. The nature of the scientific problems and the experiments that have been undertaken to solve them are briefly described.

1.1 Raman and infrared spectroscopy

Chapter 2 briefly discusses the instrumentation used to conduct experiments in vibrational spectroscopy. First, an attempt is made to discuss briefly the fundamental theories of Raman and infrared (IR) spectroscopy. Then a comparison of these two spectroscopic technique is made. Next, the instrumentation necessary to conduct high temperature, high pressure and low-temperature experiments are discussed. Advantages of modern scientific development to the conventional system are also briefly discussed.

In the last decade or two, the application of vibrational spectroscopy to study of problems important to earth science has taken a great step (white 1975). Rather than studying the basic properties of crystalline minerals, attention has focused on the near and subsurface processes and kinetics of silicate melts and glasses (McMillian and Hofmeister, 1988). Spectroscopic techniques have expanded into the area of high-pressure and high-temperature enabling scientists to accurately study the properties of minerals at extreme physical conditions. At the center of the planet the pressure exceeds 350 GPa and the temperature may be as high as 7000 K. Ultra high pressures exceeding those that exist in the center of the earth, have been achieved in the Diamond Anvil Cell (DAC) (e.g., Xu, et al., 1986). Results of these high pressure experiments have provided evidence that chemical reactions could take place at the boundaries of the silicate mantle and liquid-iron core. Melting properties of iron foil in a silicate perovskite matrix have been observed in DAC. Temperature up to 3500 K and pressure exceeding 70 GPa has been achieved in the cell (e.g., Knittle and Jeanloz, 1991). These scientific developments have opened several arenas of research in the earth as well as in material sciences.

Raman and infrared spectroscopy are very sensitive to the interatomic forces. Data from these techniques can reveal minute changes in structural parameters

resulting from differences in composition, temperature, or pressure. Farmer (1974) has reported the use of IR spectra for qualitative and quantitative analysis. Bismayer (1974) has summarized the use of soft mode in the Raman spectra in the identification of the phase transition points in crystals with temperature. Recently, Hofmeister, et al., (1989) and Chopelas (1991) identified structural transformation in olivines at high-pressure by monitoring the pressure derivatives of Raman and IR modes. Thus, the high-temperature and high-pressure techniques in vibrational spectroscopy have provided further insight into the structure and vibrational properties of earth's materials.

1.2 Study of olivines

In chapter 3 a detailed study of the properties of the Raman and infrared spectra of forsterite-monticellite (Mg_2SiO_4 - $CaMgSiO_4$) solid solution series is presented. The aim of this study is twofold: 1) to measure the Raman and IR spectra of the sample at ambient condition and at high pressures and investigate the systematic spectral variations with composition and pressure and 2) to address the cation disorder in the crystallographic sites of this series of solid solutions. In the past, isotopic experiments by Servoin and Piriou (1973) have found that substitution of different cations results in the mixing of different vibrational modes. Various models explaining this behavior have been put forth, but not with any success (McMillian, 1985). However, recent theoretical calculations by Lam et al., (1990) predict the effect of inter-tetrahedral oxygen interaction on the vibrational frequencies by the cation. Their calculations theoretically explain the vibrational mode behavior in olivine crystals. But, this has not been experimentally tested or verified. Huggins (1973) has used IR spectrometry to quantitatively discuss the cation disorder in olivine minerals. Ca-Mg exchange parameter among olivine, orthopyroxenes, and clinopyroxenes has been suggested as a

potential tool for geobarometry (Warner and Luth, 1973, Adams and Bishop, 1982). Therefore a deeper understanding of the order-disorder phenomena is demanded. Adams and Bishop (1985) have synthesized and studied the crystal structure of the forsterite-monticellite solid solution using X-ray diffraction studies. They have reported that there is only a small amount of disorder in the M1 and M2 crystallographic sites. Vibrational spectroscopy is very a sensitive tool to study the minute changes in the crystal structure. Therefore, a detailed study of vibrational mode behavior, cation disorder, and the effect of pressure on Ca-containing olivines are attempted. Also, the effect of composition by different cation substitutions on the Raman spectra are discussed in detail and an attempt is made to correlate the Raman data to the existing X-ray diffraction data.

1.3 Study of pyroxenes

In chapter 4 the vibrational spectral properties of several pyroxene crystals at ambient and high temperature are investigated. Different spectroscopic techniques used to study pyroxene have been discussed by Rossman (1980). Lazarev (1972) and Farmer (1974) have discussed the infrared spectroscopy of pyroxene. Most of the spectra were measured and used for mineral identification purposes. Iron containing samples have been studied using Mossbauer spectroscopy (Bancroft, 1973). A comparative study of the Raman spectra of crystalline and glassy diopside has been done by Etchepare (1972). Also, Tomisaka and Iishi (1980) have theoretically calculated the number of vibrational modes in diopside. X-ray diffraction studies by Cameron, et al., (1973) suggest that the mean Si-O bond length does not vary much compared to the mean M-O distances. In fact it has been suggested that there is a small negative expansion for the Si-O bonds. The differential expansion of the pyroxene structure is accommodated by the extension of the silicate tetrahedral chains and distortion of the

silicate tetrahedra. Vibrational spectroscopy is an excellent tool to study minute structural changes, such as bond lengths and bond angles, and therefore the above mentioned parameters can be verified. However, vibrational spectra of pyroxenes at high temperature do not exist. Because of the differential expansion it may be possible to distinguish between Si-O and M-O bonds. Therefore, high temperature Raman spectra of pyroxenes including the metastable nature of α -spodumene crystal have been investigated. Also, high temperature properties of different polymorphs of enstatite are studied and the spectral properties at the phase transition temperatures are discussed.

1.4 Study of amphiboles

In chapter 5 a vibrational spectroscopic study of hydroxyl ions in amphibole crystals are discussed. Raman spectra of amphiboles in the literature are very rare. The reason for this is the difficulty in measuring spectra mainly with high fluorescence and signal strength of the hydroxyl ions. But, modern advancement in spectroscopy has improved the high sensitivity and quality of the spectroscopic techniques. IR spectra of several amphibole have been reported by Farmer (1974) and Burns and Sterns (1966). Burns and Sterns have studied the effect on cation substitution on the IR spectra. They reported that the IR frequency decreases systematically with the addition of iron for magnesium. Recent work on Ti-rich richerite suggest that the intensity of the high frequency bands originating from the vibration of the silicate tetrahedra increases with increasing Ti content. Low-temperature Raman measurement on some of the hydroxyl bands showed that its frequency decreases with decreasing temperature (Wang, et al., 1988). The present study investigates the limit of detection of the hydroxyl component in amphibole crystals. Also, this study of hydroxyl in amphiboles is expected to help our understanding of the cation environments in the crystal

structure, and structural implications of the hydroxyl ions in amphiboles are also attempted to⁷ by measuring Raman spectra at high pressure and low temperature.

CHAPTER 2

EXPERIMENTAL TECHNIQUES IN VIBRATIONAL SPECTROSCOPY

Better understanding of the thermodynamic properties of minerals is extremely important for the modeling of petrological and geophysical problems. Thermodynamic properties, such as heat capacity and entropy, can be calculated from the vibrational frequencies of the crystals (Kieffer, 1985; McMillian, 1985). Lattice vibrational properties of a mineral can be studied using Raman, infrared (IR), and inelastic neutron scattering techniques. Vibrational spectroscopy involves the use of photons and neutrons, either by its scattering or absorption. Table 1 lists some of the optical spectroscopy techniques used in this area of research and the kind of information obtained with the vibrational spectroscopy. IR and Raman spectroscopy provide information about the frequency of the optical lattice and internal vibrational modes at the center of the Brillouin zone wave vector $\mathbf{k}=0$. However, for complete lattice vibrational properties of a mineral inelastic neutron scattering has to be performed. Neutron scattering requires large a single crystal but can provide information about the frequency of both acoustic and optic modes across the Brillouin zone from $0 < \mathbf{k} < \mathbf{k}_{\max}$, where the zone boundary wave vector stretch from $-p/a$ to p/a and a is the lattice parameter (To label energy uniquely it is sufficient to use only \mathbf{k} 's in the primitive cell of the reciprocal lattice. This cell in phase-space is called a Brillouin Zone (Kittle, 1966 and Sze, 1969). Acoustic modes have zero frequency at $\mathbf{k}=0$, and therefore, are not observed in the Raman and IR spectra. This chapter deals with the fundamental theory of Raman and IR spectroscopy, as well as describes various instruments used by the author during the course of this work.

Table 1. Type of optical spectroscopy and the kind information obtained from it

Type of spectroscopy	Range of energies			Type of molecular energy	Information obtained
	Frequency	(cm-1)	kJ.mol-1		
Microwave	10^9 - 10^{11}	0.03-3	4×10^{-4} -4×10^{-2}	Rotation of heavy molecules	Interatomic distances, dipolemolecules, nuclear interactions
Far Infrared	10^{11} - 10^{13}	3-300	4×10^{-2} -4	Rotation of light molecules vibrations of heavy molecules	Interatomic distances, bond force constants
Infrared	10^{13} - 10^{14}	300-4000	4-40	vibrations of light molecules, vibration rotation	interatomic distances, force constants, charge distributions
Raman	10^{11} - 10^{14}	3-4000	4×10^{-2} -40	pure rotation or vibration vibration -rotation	interatomic distances, force constants, charge distribution
Visible, UV	10^{14} - 10^{16}	3x103-3x105	40-4000	electronic transition	bond dissociation energies

2.1 Infrared spectroscopy

In infrared spectroscopy the fundamental vibrations are observed as absorption bands when the sample is exposed to polychromatic infrared radiation. The radiation having frequencies corresponding to those of vibrational motion of molecule associated with change in the permanent dipole moment get absorbed by the sample. Both Raman and infrared spectroscopy provide vibrational information about the vibrational energy levels of the molecules. But the quantum mechanical selection rules governing the photon transitions are different. Infrared and Raman techniques are complementary. For a thorough vibrational spectral study of a sample, one has to measure both Raman and IR spectra of the sample (see Table 1). One of the important applications of the vibrational spectral study is qualitative and quantitative analysis of minerals at the molecular level. For example, White (1974) has used infrared spectroscopy to qualitatively determine the degree of disorder in minerals. Burns and Sterns (1966), Stoppler (1987) and Rossman (1990) have used IR spectroscopy to quantitatively determine the amount of hydroxyl ions present in the mineral and glass of mineral compositions.

The number of lines in the vibrational spectrum depends on the symmetry of the molecular species and, in the case of crystalline minerals, on the space group of the sample. The position of the vibrational line depends on inter-atomic forces between various atoms and on the reduced mass of the atoms responsible for the vibrational modes. The vibrational frequencies are very sensitive to the interatomic forces and thus are capable of revealing small changes in composition, temperature, or pressure. In vibrational spectrum, band positions depend on the interatomic forces between the atoms, and their band frequencies vary within the crystal structure of the sample, and the above parameters are very sensitive to the bond lengths and bond angles. Vibrational

spectroscopy is, therefore, an excellent tool to study the effect of high temperature and high pressure on the structure and thermodynamic properties of minerals.

2.2 Fundamental theory of infrared spectroscopy

Theory of infrared spectroscopy is discussed in great detail by several authors (Farmer, 1974, Colthop, 1966). The following is only a short description of the theory. In the infrared spectroscopy the probing light gets absorbed giving set of absorption peaks establishing a vibrational spectrum (Fig. 1). For a normal mode to be infrared active there must be a change in the dipole moment, m , during the course of molecular vibration. Two equal electric charges, Q units, of opposite polarity separated by distance d is given by

$$m = Q \times d. \quad (2.1)$$

For a vibrating polyatomic molecule the net dipole moment can be written as

$$m(r) = m(r_0) + (dm/dr) \times \delta r \quad (2.2)$$

where δr is the displacement due to the vibration from the equilibrium position. Since vibrational state is oscillatory this gives raise to oscillating electric field. The transition moment resulting from the interaction of the induced electric field and the external electric field can be written as

$$M_{n'n'} = \text{Inte. } U_{n'} \times m(r) U_n dr \quad (2.3)$$

$$= m_0 \text{ Int. } U_{n'} \times U_n dr + \\ \text{Int. } U_{n'} Q \times dr U_n dr. \quad (2.4)$$

where U_n and $U_{n'}$ are the wavefunctions. By the properties of orthogonality functions the first term is always zero. So, an infrared transition to take place is when $Q=0$. For this

reason for a homonuclear molecule (no permanent dipole moment) there is no infrared transition. But in some special cases due to the introduction of foreign species, infrared

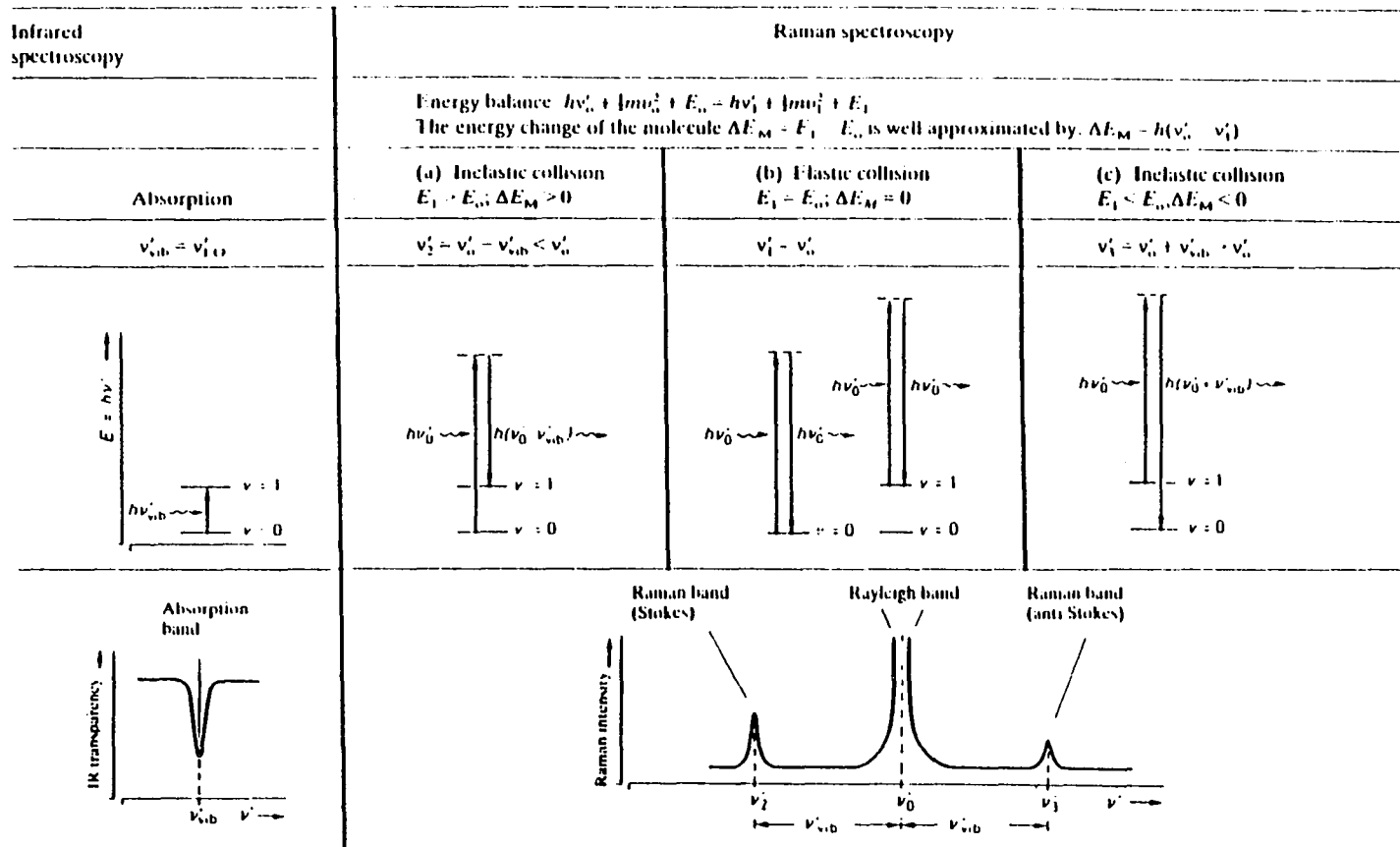


Figure 1: Energy level diagram representing Raman and infrared transitions.

transition occurs due to the changes in dipole moment as were shown in the case of MgO, CaO and Mg₂SiO₄ giving infrared transitions (Martens and Freund, 1976; Freund, 1981; Freaund and Wengeler, 1981; Freund et al.,1983).

Presence and various amount of molecular species can be determined quantitatively from their respective infrared absorption bands. The intensity of the radiation I , as it penetrates through a sample of thickness t , according to Beer's law, is proportional to I_0 , the incoming radiation intensity, to C the molar concentration and to the path length t . If the absorption coefficient is A , we can write the equation as

$$I = I_0 e^{-Act.} \quad (2.5)$$

The above equation can be used to determine quantitatively the amount of volatiles such as H₂O, CO₂, CH₄ etc., in the rocks with great accuracy. In the present work IR spectroscopy is used for two purposes: 1)to detect and quantify the hydroxyl group (OH-) in amphibole crystals, and 2) infer structural properties of olivine minerals at high pressure.

2.3 Fourier transform infrared (FT-IR) spectroscopy

The essential component of an interferometer is a system for splitting a beam of radiation into two and then recombining the two beams. This is achieved by sending the incident light beam through a beam splitter, which directs 50% of each components (reflected and transmitted) to two mirrors placed 90° to each other as shown in Fig. 2. One part of the beam goes to a fixed mirror and the other part to a back and forth moving mirror. The reflected light from each mirror is recombined at the beam splitter and sent to a detector. When the two beams recombine at the beam splitter, constructive and destructive interference fringes occurs depending on the position of the moving mirror, as dictated by the wave theory. For a single wavelength of light, the intensity at the detector versus time gives a sinusoidal wave and is called an interferogram (Fig. 3). This is the Fourier Transform of a delta function at the laser frequency. In Fourier

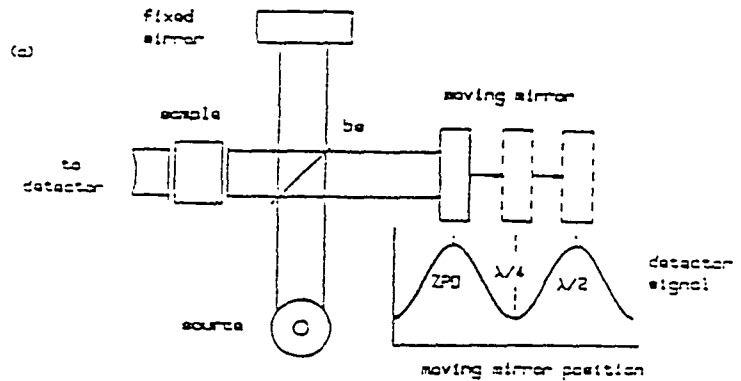


Figure 2: Schematic diagram showing components of a Michelson interferometer.

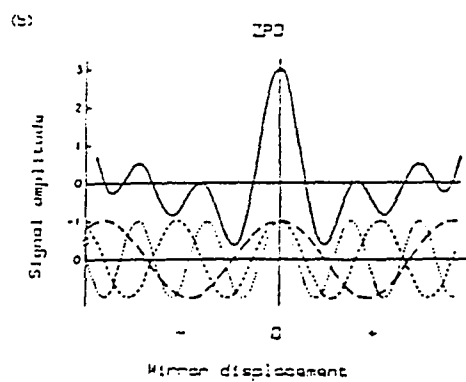


Figure 3: Typical interferogram formed by an interferometer.

transform spectroscopic experiments the light intensity is measured at the detector in the time domain then converted to energy units using Fourier Transform and, then graphically displayed or plotted versus peak intensity.

When the source emits a wide range of frequencies of light, the resulting sine wave from each frequency adds constructively only when the moving mirror exactly the same distance from the fixed mirror (Fig. 3). Thus, every data point of the resulting interferogram contains information on the entire frequency range of the source. In FT-IR experiments, Helium-Neon (He-Ne) laser is used as a reference beam which passes through the beam splitter to monitor the exact position of the moving mirror.

2.4 Advantages of using FT-IR over conventional spectroscopy

- 1) A single scan by the moving mirror (<1 sec) contains all the spectral information. Signal to noise ratio is improved by averaging multiple scans (Fellgett's advantage).
- 2) The energy reaching the detector is only a function of source strength and sample absorbance, not a function of slit-width (Jaquinot advantage).
- 3) Use of He-Ne laser as a standard provides an accurate measurements of the frequency of the bands. (resolution up to 0.01 cm^{-1}).
- 4) Resolution of the spectrum is determined by the distance through which the mirror moves, not the slit width as in the case with dispersive instruments.
- 5) Stray light does not affect the signal, since it is not part of the interferogram.

2.5 Raman spectroscopy

Inelastic scattering of light was discovered in 1928 by Sir C. V. Raman during a series of experiments on light scattering in fluids and was first observed in benzene and toluene (Raman, 1928 and Krishan, 1978). Raman and his co-workers filtered

sunlight using a violet filter, focus the violet beam using a condensing lens, and passed through purified organic liquids. In the scattered light they detected light rays in the green region of the electromagnetic spectrum. Also, they noticed that the new radiation they observed was partially polarized. Raman called this new radiation "Secondary Radiation" and published his findings in "Nature". Later on this radiation was recognized to originate from the molecular vibration of the sample and this scattering phenomena was named after Sir. C. V. Raman as the Raman Effect. There is ample literature available on the theory and use of Raman Effect (e.g. Hertzberg, 1945., Colthop, et al., 1964; Farmer, 1974; Barnes and Thomas, 1977; Grasselli, et al., 1981; Strommen and Nakamoto, 1984; Richards and Scott, 1985; Fadini and Schnepel, 1989; Gardiner and Graves, 1989). In the following the fundamental theory of Raman effect is described.

2.6 Theory of spontaneous (normal) Raman effect

In Raman scattering the exciting monochromatic light, a laser radiation, is inelastically scattered by the vibrating molecules giving rise to a set of lines in the spectrum of scattered light as a function of energy, at frequencies corresponding to the allowed vibrational levels in the sample. For a molecular vibration to be Raman active, there must be a change in the induced dipole moment resulting from the change in the polarizability of the molecule. Raman effect can be briefly explained using simple theories of electromagnetic phenomena. Assume the electric field of the incident electromagnetic wave is represented by

$$E = E_0 \sin 2\pi v_0 t \quad (2.6)$$

where v_0 is the frequency of the incident wave. Upon interacting with an atom in the sample this field produces an induced dipole μ in the atom and it is given by

$$\mu = \alpha E \quad (2.7)$$

where α is the polarizability of the atom. In a non-symmetrical atom, for small displacements the polarizability can be written as

$$\alpha = \alpha_0 + d\alpha/d(\Delta r)x \Delta r \quad (2.8)$$

where α_0 is the equilibrium polarizability and Δr is the difference between the internuclear distance at any time. Since, for small vibrations Δr can be considered as harmonic, we can write,

$$\Delta r = a \sin 2\pi v't,$$

where a is the amplitude and v' is the frequency of oscillation.

Thus, we get

$$\mu = aE \quad (2.9)$$

$$= (\alpha_0 + dr/d(\Delta r). a \sin 2\pi v't)x(E_0 \sin 2\pi v_0 t) \quad (2.10)$$

Upon simplifying, we get,

$$\begin{aligned} \mu = E_0 \sin 2\pi v_0 t &+ (\alpha_0 E_0/2) d\alpha/d(\Delta r)x [\cos 2\pi(v_0 - v')t \\ &- \cos 2\pi(v_0 + v')t]. \end{aligned} \quad (2.11)$$

The first term represents unchanged incident frequency (Rayleigh Scattering), the second and third term represent the frequencies shifted to lower and higher frequencies by the same amount (Fig. 1). The bands at lower frequencies are called Stokes-Raman shifts and those on higher frequencies are referred as Anti-Stokes Raman shifts. For a molecular vibration to be Raman active there must be a change in the polarizability of the molecule resulting in an induced dipole moment.

An energy level diagram may be used to represent the Raman transitions (Fig. 1). In the table, $n=0$ and $n=1$ represents the energy levels of the molecule. When a photon interacts with the molecule in the ground state it acquires more energy and momentarily goes to a meta-stable higher energy level. Since this is an unstable state,

the molecule returns to the ground state giving off excess energy it acquired during the excitation process. This molecule has the same energy as the incident photon and give rise to Rayleigh scattering. But, if the molecule only drops to the intermediate state $n=1$ then the energy irradiated is less than the incident photon energy and is termed as Stoke-Raman line. If the transition occurs from $n=1$ state to the ground state, as shown in Fig. 1, then the energy given off has more energy than the incident radiation, then the band is called anti-Stoke Raman line. Evidently the anti-Stoke Raman lines have higher frequency relative to the frequency of the excitation source and the Stoke-Raman lines appear at lower frequency.

2.7 Effect of temperature on the intensities of Raman bands

At room temperature, the ground state is more populated than the excited state hence more molecules are available to pump to higher levels. Therefore, the intensity of the Stoke-Raman lines are stronger than anti-Stoke Raman lines at ambient conditions (Fig. 4). However, at high temperature, higher energy states get populated resulting in a stronger Raman radiation for the anti-Stoke lines. This phenomena can be made use of to determine the vibrational temperature of the sample. Assume that the measured intensity of Stoke and anti-stoke lines of the sample, under the same experimental conditions, be I_S and I_{AS} . Then the following expression can be used to determine the temperature of the sample:

$$I_S/I_{AS} = [(v_o - v_k)/(v_o + v_k)]^4 * \exp(hcv_k/kT) \quad (2.12)$$

v_o and v_k are the incident and the scattered frequencies, h is the Planck's constant, c is the speed of the light, k is the Boltzman's constant and T is the absolute temperature.

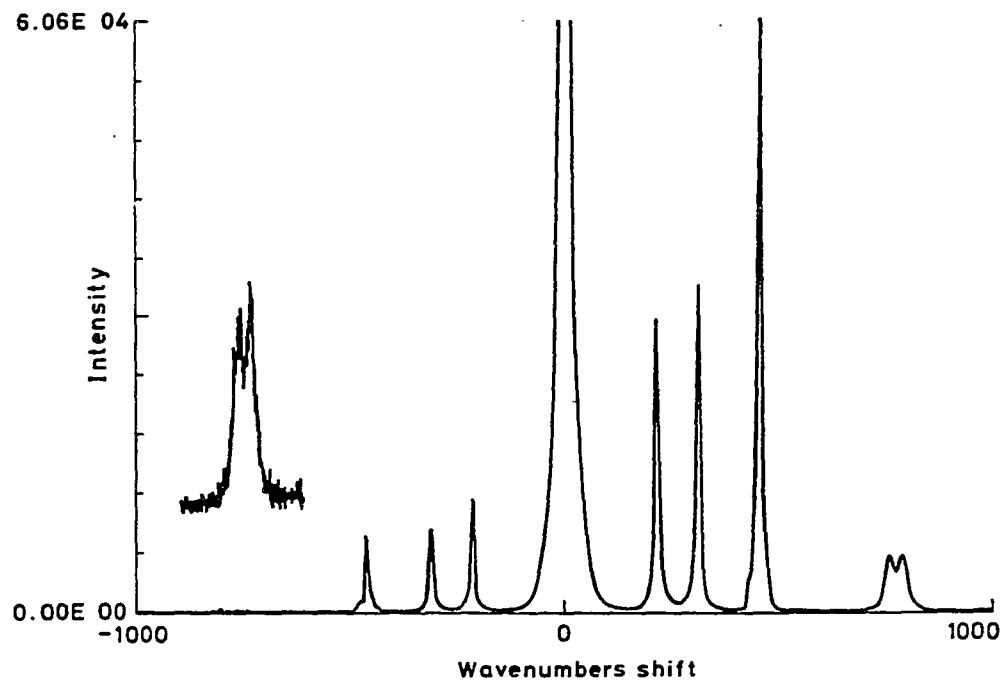


Figure 4: Stokes and Anti-Stokes lines of carbon tetrachloride (CCl₄)
(after Gardiner and Graves, 1989).

2.8 Polarization studies

Symmetric and antisymmetric vibrations can be distinguished by measuring the depolarization ratio of the Raman bands. Totally symmetric vibrations give rise to polarized Raman bands in the spectra, while antisymmetric vibrations give rise to unpolarized bands. The ratio of intensities of the scattered radiation with their plane of polarization parallel and perpendicular to that of the laser beam is termed as depolarization ratio ρ . Mathematically it is written as

$$\rho = I_{\text{perpendicular}}/I_{\text{parallel}} = 6 \beta^2/(45 \alpha^2 + 7 \beta^2) \quad (2.13)$$

where α and β are the terms related to the isotropic and anisotropic part of the polarizability tensor, respectively (Colthop, 1964). The minimum and maximum value of the depolarization ratio lies between $\rho=0$ and $6/7$. $\rho=0$ (polarized) corresponds to completely symmetric vibration while $\rho=6/7$ (depolarized) corresponds to completely anti-symmetric vibration. In reality, due to the presence of off-diagonal elements in the b term, intensity of total symmetric vibration is not completely zero (Fadini and Schnebel, 1989).

The depolarization ratio is measured by placing an analyzer in between the sample and the spectrometer in two different orientation as shown in Fig. 5 (Colthup, et al., 1964). An example of the measurement of depolarization ratio of carbon tetrachloride is given in Fig. 6.

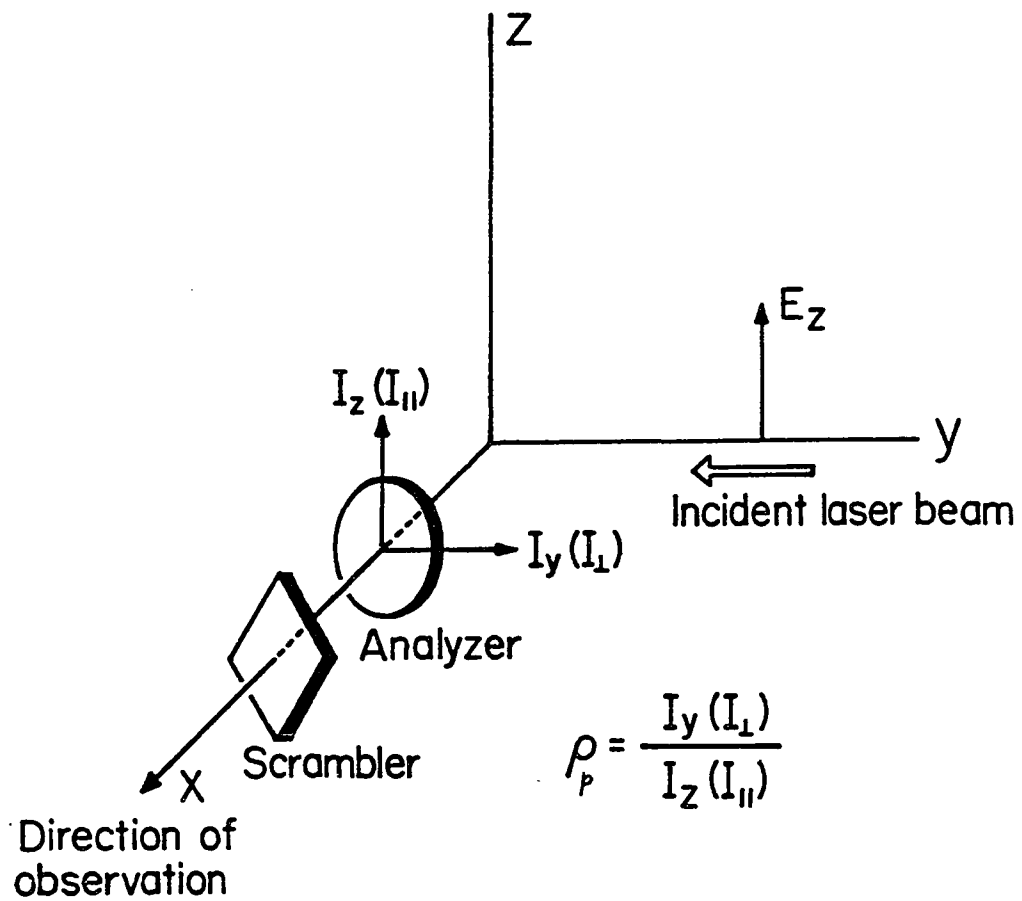


Figure 5: Experimental configuration for depolarization measurements
(after Strommen and Nakamoto, 1984).

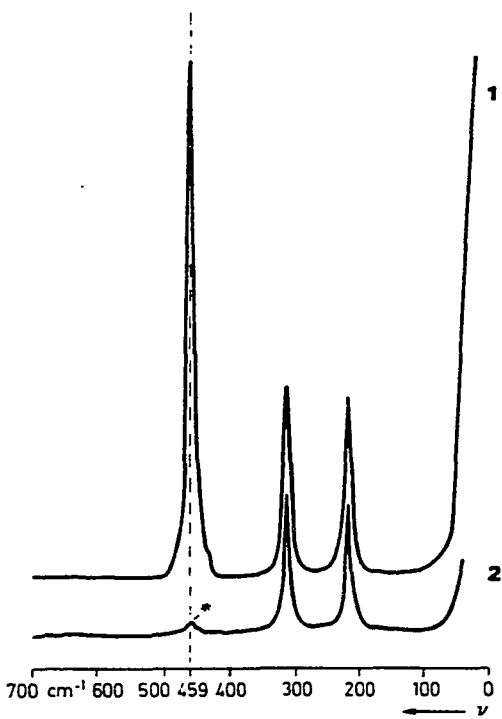


Figure 6: Depolarized (trace 1) and polarized (trace 2) spectra of carbon tetrachloride (CCl_4). The band at 459 cm^{-1} has a depolarization almost zero, therefore assigned to totally symmetric vibration of the molecule.

2.9 Multichannel micro-Raman spectroscopy

A micro-Raman multichannel experimental setup utilized at the Hawaii Institute of Geophysics Lab, (HIG 107), is shown in Fig. 7. The main components of the experimental setup consists of a laser source (e.g. Spectra Physics Model# 2020), a pre-monochromator, a Leitz microscope, a 0.6 meter Spex Triple mate Spectrograph (1877 Series), an intensified Diode array or a liquid N₂ cooled CCD detector, and a computer that is connected to the detector as well as to a plotter. First, the laser beam is passed through a pre-monochromator to eliminate all the plasma lines (Fig. 8). Then using prisms and mirrors the beam is directed to the microscope for 135° or 180° scattering geometry. The beam is focused on to the sample either at 135° using a convex lens or at 180° using a microscope objective (back scattering geometry). The scattered beam is collected by the microscope objective and focused on to the entrance slit of the spectrometer. The Raman signal is analyzed with a diffraction grating preselected by the operator from a set of three gratings (600, 1200 or 1800 groves/mm) based on the spectral resolution requirements. The signal is collected with either a thermo-electrically cooled intensified diode array detector (OMA: Optical Multichannel Analyzer with 1024 pixels) or a nitrogen cooled Charge Coupled Devices (CCD) detector with 1024 x 256 pixels. Finally, the signal from the detector is digitally processed with a computer, and the data is stored on to a computer disk or plotted on to a paper for detailed analysis.

2.10 Calibration of the micro-Raman spectrometer

On starting of the data acquisition routine (computer program) the computer screen displays the x-axis in pixel numbers. In order to display and record the collected spectra in the correct energy units (usually Raman Shift, cm⁻¹), the spectrometer has to be calibrated in the required frequency range. First, the diffraction grating is

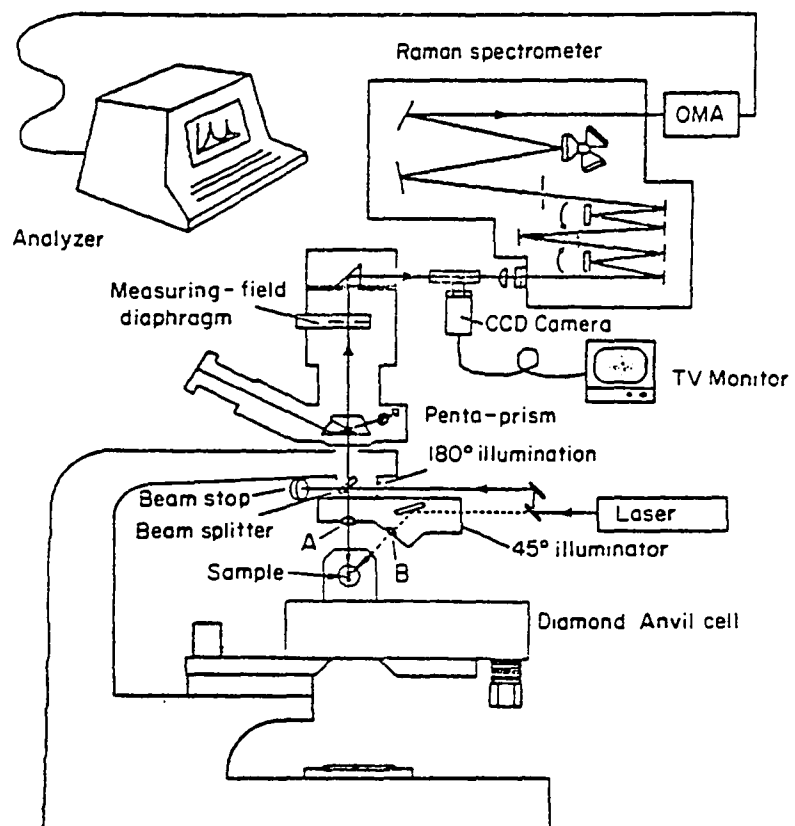


Figure 7: Block Diagram of the micro-Raman setup utilized in the Hawaii Institute of Geophysics, at the University of Hawaii.

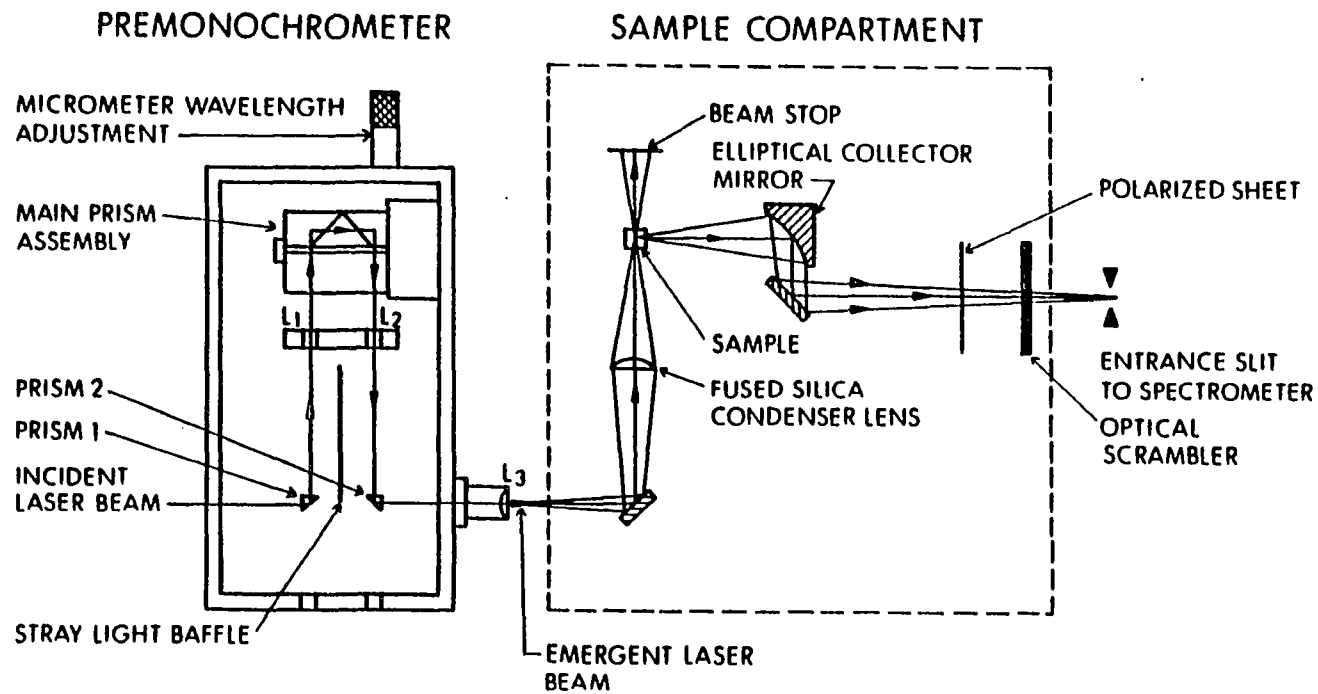


Figure 8: Block diagram of the pre-monochromator showing the optical path taken by the laser.

selected required by the resolution of the data. There are three gratings (600, 1200, and 1800 grooves/mm) available in the triple mate. 600 grooves/mm grating has the lowest resolution, but has the highest frequency span. 1800 grooves/mm on the other hand has the highest resolution and lowest frequency span. For example, for the identification of different mineral components in a sample rock, 600 grooves/mm grating may be a better choice, because it covers a wide frequency range. On the other hand, for high temperature structural studies of a mineral, since the changes in the Raman bands are very small, 1800 grooves/mm grating is the proper selection. It is noted that the final resolution of the spectra is also a function of the entrance slit width and the excitation source.

In order to calibrate the instrument in the low frequency region, for example, first a spectrum of calcite with high signal to noise ratio is collected and stored in to the computer memory or on to the computer disk. Then for each peak of the calcite spectra, with corresponding pixel number, the known Raman shift is entered into the computer as requested by the calibration routine. At the final step, the calibration program converts the pixel numbers to Raman shift (cm^{-1}) in the frequency region chosen. The calibration is always tested by acquiring the spectra of the same sample used for calibration and checking for any shift in the band position. In the event of a large shifts the calibration has to be repeated.

<u>Frequency Range</u>	<u>Calibration Source</u>	<u>Information Obtained</u>
100 - 1400 cm ⁻¹	Calcite or Indene	Lattice modes, silicate bending and stretching
700 - 2000 cm ⁻¹	Indene	Bending Modes of H ₂ O (~1600 cm ⁻¹)
2000 -3000 cm ⁻¹	Mercury lines or Plasma lines	C-H Stretching of methane
3000 - 4000 cm ⁻¹	Plasma lines	stretching modes of water and hydroxyl ions

In Figs. 9,10, and 11 sample spectra of calcite, indene and plasma lines from the Ar+ used for spectrometer calibration are shown. In Table 2 some of the major peaks of Indene, in the 300-3200 cm⁻¹, used for the calibration of the spectrometer are listed. Some frequently used laser lines and list of plasma lines with their relative intensities (for easier identifications) are listed in Tables 3, 4, 5, and 6. When using mercury arc lamp or plasma lines from a laser extreme care has to be taken not to damage the detector, because these sources are very intense. The beam entering the spectrometer should be carefully controlled using adjustable apertures and slits. Calibration of the spectrometer with plasma lines is easily done with a fiber optic setup. The schematic diagram showing the details of the fiber optic set up is given in Fig. 12. This arrangement allows one to calibrate the spectrometer with out much optical alignment.

2.11 Advantages of micro-Raman spectroscopy

Several authors have discussed the advantages of micro-Raman setup in detail (McMillian, 1985). There are several advantages in using a micro-Raman spectrometer in conjunction with a multichannel detector (OMA or CCD) over a

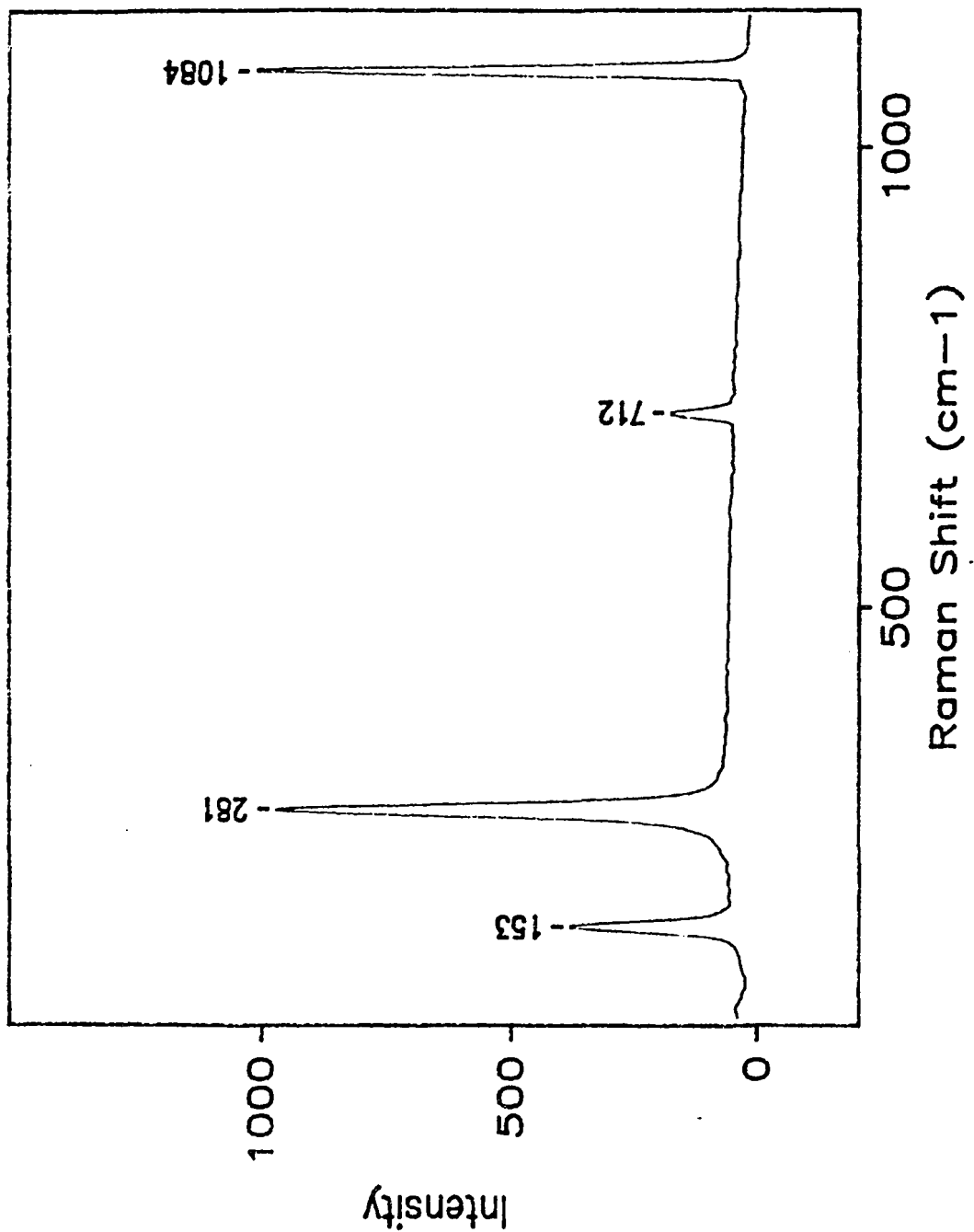


Figure 9: Spectrum of calcite in the 100-1200 cm^{-1} region.

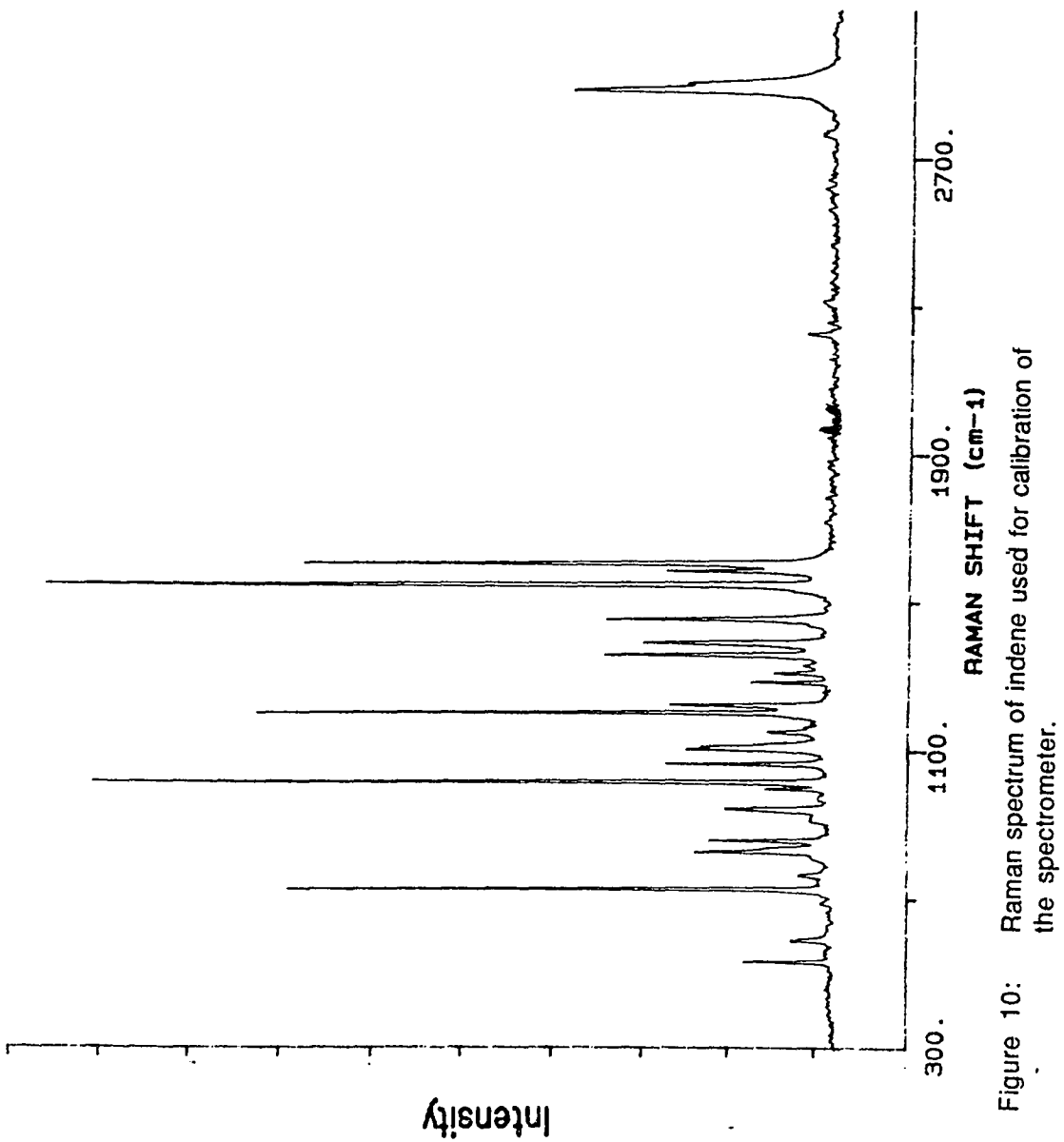


Figure 10: Raman spectrum of indene used for calibration of the spectrometer.

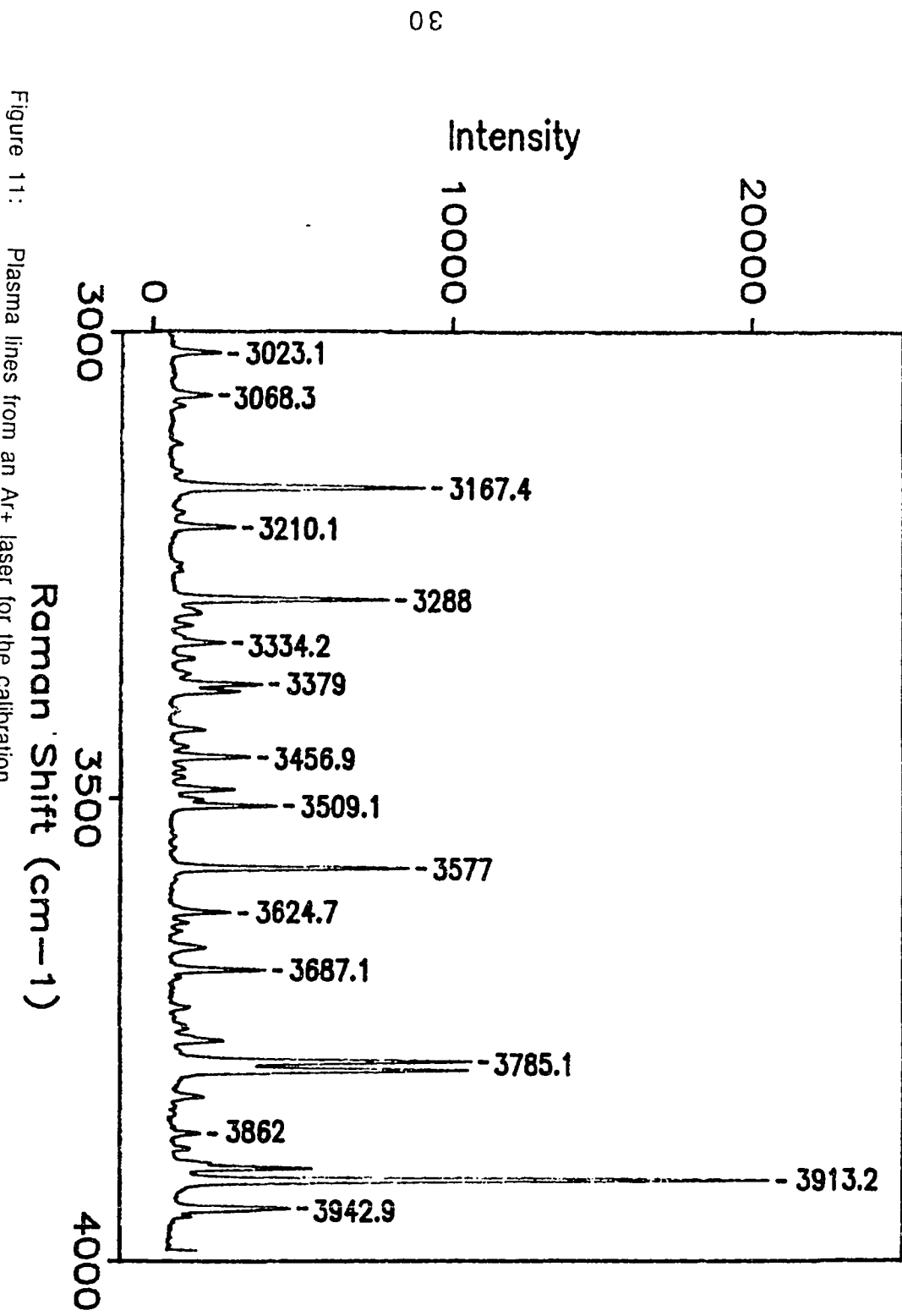


Figure 11: Plasma lines from an Ar⁺ laser for the calibration.

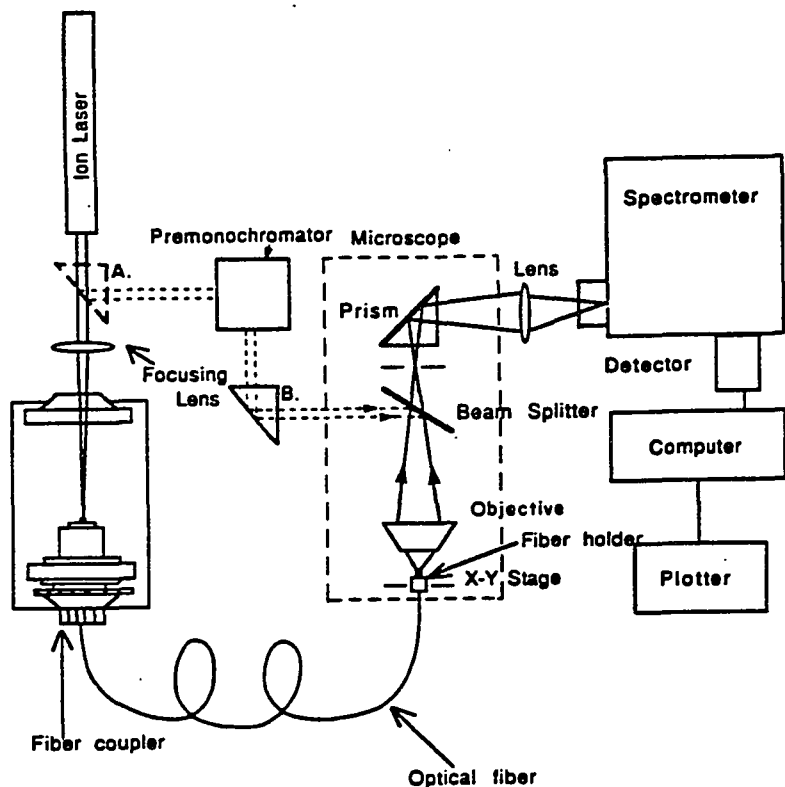


Figure 12: Block diagram of the set up used for the plasma line calibration.

Table 2 Indene vibrational lines used for the calibration
of the Raman spectrometer.

Line	Best (cm ⁻¹)	Source of values ^a	Calibration lines ^b
1	205.0 ± 2	N	
2	533.7 ± 0.5	N	↔
3	593.0 ± 2	N	
4	730.1 ± 0.2	I	↔
5	830.5 ± 0.2	I	
6	861.3 ± 0.2	I	
7	947.2 ± 0.3	I	
8	1018.6 ± 0.2	I	↔
9	1067.9 ± 0.2	I	↔
10	1108.9 ± 1	N	
11	1154.5 ± 0.5	I	
12	1205.2 ± 0.2	I	↔
13	1226.2 ± 0.2	I	↔
14	1287.8 ± 0.2	I	
15	1361.3 ± 0.4	I	↔
16	1393.2 ± 1	I	↔
17	1457.8 ± 0.5	I	↔
18	1553.3 ± 0.5	I	↔
19	1589.8 ± 1	N	
20	1609.6 ± 0.2	I	↔
21	2892.2 ± 1	N	↔
22	2901.2 ± 1	N	↔
23	3054.7 ± 1	N	↔
24	3068.5 ± 2.5	I	↔
25	3112.7 ± 0.5	N	↔

Table 3: Some frequently used laser lines and their corresponding wavenumbers in air

Laser	Wavelength in Air(nm)	Wavenumber in Air(cm ⁻¹)	Typical Power(mW)
Ar-ion ^a	457.9(violet)	21838.8	300
	465.8	21468.4	130
	472.7	21155.1	250
	476.5(blue)	20986.4	600
	488.0(blue)	20491.8	1300
	496.5	20141.0	600
	501.7(green)	19932.2	300
	514.5(green)	19436.3	1700
	528.7(yellow-green)	18914.3	300
Kr-ion ^b	476.2	20999.6	60
	482.5	20725.4	45
	520.8	19201.2	90
	530.9	18835.9	200
	568.2	17599.4	200
	647.1(red)	15453.6	500
	676.4	14784.2	120
	752.5	13289.0	100
	799.3	12510.9	30
He-Ne ^c	632.8(red)	15802.8	50

a. Power value for Spectra-Physics Model 164-08.

b. Power value for Spectra-Physics Model 164-01.

c. Power value for Spectra-Physics Model 125A.

Table 4 Plasma lines from an Ar+ laser used for Raman spectrometer calibration

Wavelength in Air (nm)	Relative Intensity	Wavelength in Air (nm)	Relative Intensity
487.9860	5000	569.1650	27
488.9033	200	572.4325	23
490.4753	130	573.95207	16
493.3206	970	577.2326	69
494.2915	14	578.6560	16
495.5111	10	581.2746	49
496.5073	960	584.3781	18
497.2157	330	587.0443	12
500.9334	1500	588.26250	11
501.7160	620	588.85851	18
506.2036	1400	591.20861	38
509.0496	10	592.88124	10
514.1790	360	595.0905	11
514.5319	1000	598.5920	23
516.2745	8	598.9339	20
516.5774	38	603.21291	57
517.6233	41	604.32254	37
521.6816	20	604.4468	14
528.6895	150	604.6894	14
530.5690	12	604.9072	14
539.7522	18	605.93735	15
540.2604	11	607.7431	11
540.7348	12	610.3546	91
545.4307	19	611.4929	< 1750
549.5876	14	612.3368	100
549.8185	14	613.8660	97
550.0334	14	617.2290	1400
555.4050	22	618.7136	26
555.87031	30	623.9713	26
557.25428	12	624.3125	590
557.7689	18	632.4414	16
557.8518	11	638.47189	11
560.67341	48	639.6614	14
562.5684	14	639.9215	160
563.5882	14	641.63075	50
565.07054	29	643.7604	27
565.4450	27	644.1908	22
567.2952	22	644.3858	16

Table 5 Plasma lines of a Kr+ laser

Wavelength in Air (nm)	Relative Intensity	Wavelength in Air (nm)	Relative Intensity	Wavelength in Air (nm)	Relative Intensity
521.60	350	591.17	110	731.05	80
522.49	20	596.75	100	733.78	60
522.95	600	599.22	1000	736.16	90
527.65	220	601.00	90	737.30	60
530.87	2300	602.24	200	740.70	800
532.28	200	603.72	10	743.58	400
533.24	2000	609.45	50	744.38	150
534.68	300	611.96	70	748.68	280
535.55	80	616.88	160	749.36	180
541.84	200	630.37	160	751.26	400
543.86	400	631.28	10	752.45	600
544.63	900	639.11	100	755.57	180
546.82	1100	640.98	70	756.54	250
549.95	450	641.66	150	758.74	550
552.29	1050	624.02	700	760.15	600
555.30	400			768.52	400
556.22	200	647.09	250	769.45	250
556.86	1000	651.09	430	773.57	200
557.03	550	657.01	1000	775.07	200
563.50	1400	660.30	160	778.94	130
565.04	250	662.50	30	781.25	250
566.99	300	662.86	160	782.60	450
567.28	570	663.50	110	783.58	190
567.45	400	664.45	100	784.07	520
568.19	3500	665.25	100	785.48	500
569.03	2000	668.40	60	790.76	120
569.41	400	676.44	330	791.01	190
569.99	400	677.12	100	791.45	70
571.72	180	687.08	110	793.14	130
575.30	1000	694.41	30	797.36	100
577.14	1700	707.40	100	799.32	700
577.80	400	713.40	170	799.80	300
586.07	270	721.31	600	801.86	110
587.09	750	728.98	900	805.95	600

Table 6 Plasma lines of Helium-Neon laser

Wavelength in Air (nm)	Relative Intensity	Wavelength in Air (nm)	Relative Intensity
638.299	53	706.519	31
640.108	>100	717.394	4
640.975	31	724.517	5
644.472	30	728.135	11
650.653	50	748.887	0.5
659.895	41	753.577	0.4
667.815		754.405	0.3
667.828}	91	777.730	5
671.704	36	794.318	0.1
692.947	19	813.641	0.2

conventional Raman scattering technique with a scanning spectrometer attached to a single channel photon counting detector system. In micro-Raman the laser beam is focused to a small spot size ($\sim 10 \mu\text{m}$), and therefore, requires only a very small amount of sample. In normal Raman scattering experiments beam size is much larger and usually requires a larger amount (volume) of sample. In micro-Raman spectrometry the laser power at the sample is of the order of 10 mW or few micro watts in some cases, while in normal Raman scattering the laser power could be as high as 500 mW. Higher laser power results in local laser heating of the sample, which in turn could alter the structure of the sample during the measurements itself. Also, if the beam diameter is very small one can study very sharp phase boundaries. Multichannel detection system is extremely fast and scans a wide frequency range at the same time. This is a great advantage to high temperature and high pressure experiments. With increasing pressure and temperature minerals undergo structural changes and phase transitions at critical P and T, and requires a fast scan over a wide range of frequencies to detect the structural changes in the sample. Therefore, kinetics of a sample can be studied with a multichannel micro-Raman system which otherwise is extremely difficult to measure with a conventional setup. Also, fast measurements also help prolong life time of the experimental components such as high temperature furnace, laser source, etc. One notable advantage of conventional scanning spectrometer over multichannel micro-Raman setup is that it can be used to do very high resolution spectroscopy work, and can measure frequencies with an accuracy of with in 0.2 cm^{-1} .

2.12 High-temperature Raman studies

In the recent years conventional as well as micro-Raman high- temperature spectroscopy has been used widely in earth sciences (Hemley et al., 1987; Sharma, 1989, Sharma, 1991, Ghose, 1985). At high-temperature certain vibrational modes in some minerals (e.g. quartz, cristobolite, etc.) tend towards at critical temperature and produce instability in the crystal. Such a vibrational mode is called Soft Mode. Phase transition in minerals can be studied accurately by monitoring the soft mode in crystalline minerals (Salje, 1988).

High-temperatures in minerals are achieved by heating the sample in a windowless furnace as shown in the Fig. 13. The furnace is heated with platinum - 10% rhodium wire and a temperature up to 1400 K can be achieved. It is designed such a way that it can be used in conjunction with 0° , 90° or 180° scattering geometries, which is useful for polarization studies. The sample is placed in the furnace and the laser beam is focused on to the sample using a converging lens. The scattered beam is collected using a large convex lens and focused at the entrance slit of the spectrometer.

Blackbody radiation at $T < 1073$ K cause a problem in high temperature experiments. However, this can be circumvented by proper selection of excitation wavelength (towards blue end of the visible spectrum 488.0 nm or 459.7 nm). Time-resolved techniques using 532 nm line of a frequency-doubled pulse laser system (Nd:YAG) in conjunction with a dual box-car signal integrator system are an excellent way to do high-temperature spectroscopy.

2.13 High-pressure Raman and ir studies

Raman and infrared spectra of minerals at high-pressure studies are performed with a Diamond Anvil Cell (DAC) as shown in Fig. 14. There are two sets of DACs in use in the Raman spectroscopy laboratory: the one set for conducting Raman scattering

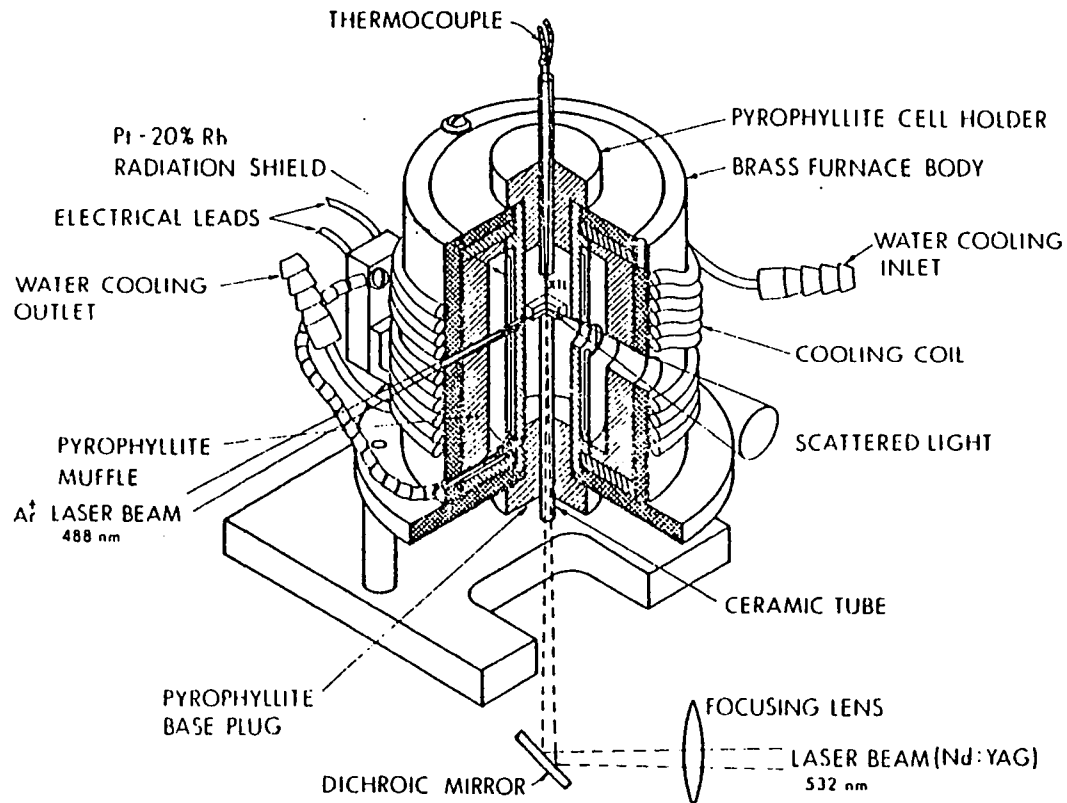


Figure 13: Furnace used for conducting high temperature Raman spectroscopy. Temperature as high as 1200 K may be achieved using this furnace.

40

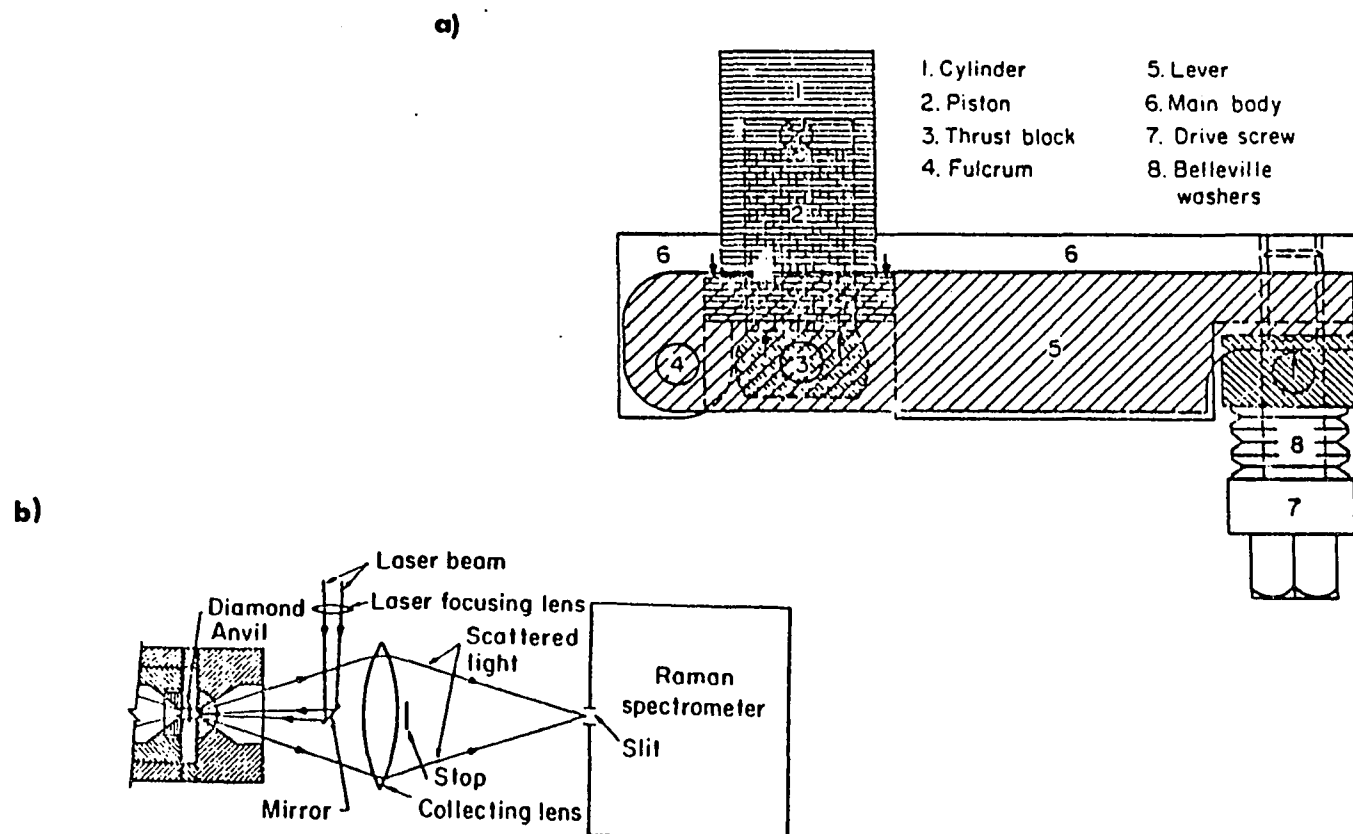


Figure 14: Schematic diagram showing optical path in a Diamond Anvil Cell (DAC) used for conducting high pressure Raman spectroscopy.

experiments and the other one for IR experiments. In both cases high quality type II diamonds were used for the experiments. The experimental setup in both cases are somewhat similar. In Raman scattering experiments, the incident beam brought in to the sample chamber at about 45° to the vertical, while in the case of IR experiments the infrared beam enter the sample chamber in the line as of the emerging beam (transmission spectra).

The diamond anvil cell consists of two diamonds with parallel flat faces facing each other. In Fig. 15, the details of the DAC including the sample chamber, ruby, and the metal gasket are shown. Sample is placed on a metal gasket with a $300 \mu\text{m}$ hole in it. The pressure is increased by bringing the two diamonds closer with the sample sandwiched between them. For uniform distribution of pressure throughout the sample chamber, a suitable pressure transmitting medium, such as methanol-ethanol-water (16:3:1) mixture, or argon or xenon gas are used. One part of water is added to the methanol-ethanol mixture to avoid condensation of methanol at approximately 125 kbar (Sharma, et al., 1990). The pressure is determined by monitoring the ruby fluorescence line (R_1). In order to achieve this, a small ruby chip is placed in the sample chamber along with the sample. The fluorescence signal from the ruby crystals resulting from the laser beam excitation is collected using a fiber optic probe placed under the lower diamond. This signal is analyzed with a Spex double monochromator (Model 1403) and the shift in the R_1 fluorescence line with pressure is recorded. The pressure in the DAC at any given time can be calculated using the following formula

$$P(\text{kb}) = 3808 [(\lambda/\lambda_0)^5 - 1] \quad (2.14)$$

where λ_0 (nm) is the wavelength of the R_1 ruby line at 1 bar and λ is its wavelength at pressure P (Sharma, et al., 1992). Fig. 16 shows variation of R_1 line with increasing applied pressure.

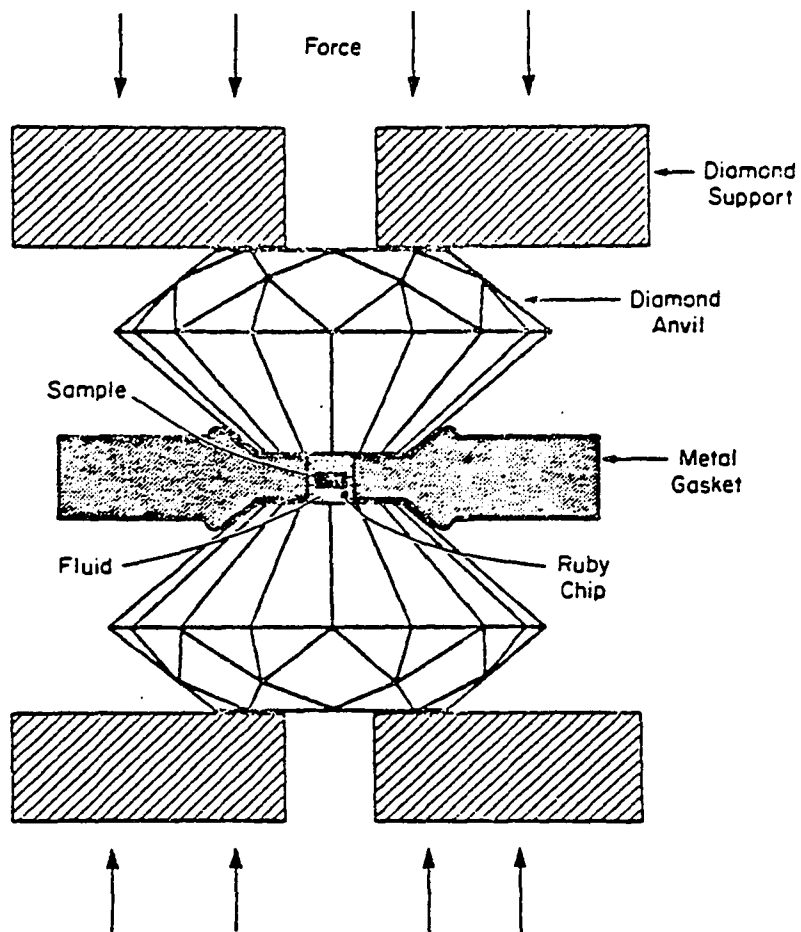


Figure 15: Details of the DAC showing position sample, ruby, and metal gasket. Direction of applied force is perpendicular to the diamond as shown by the arrow mark.

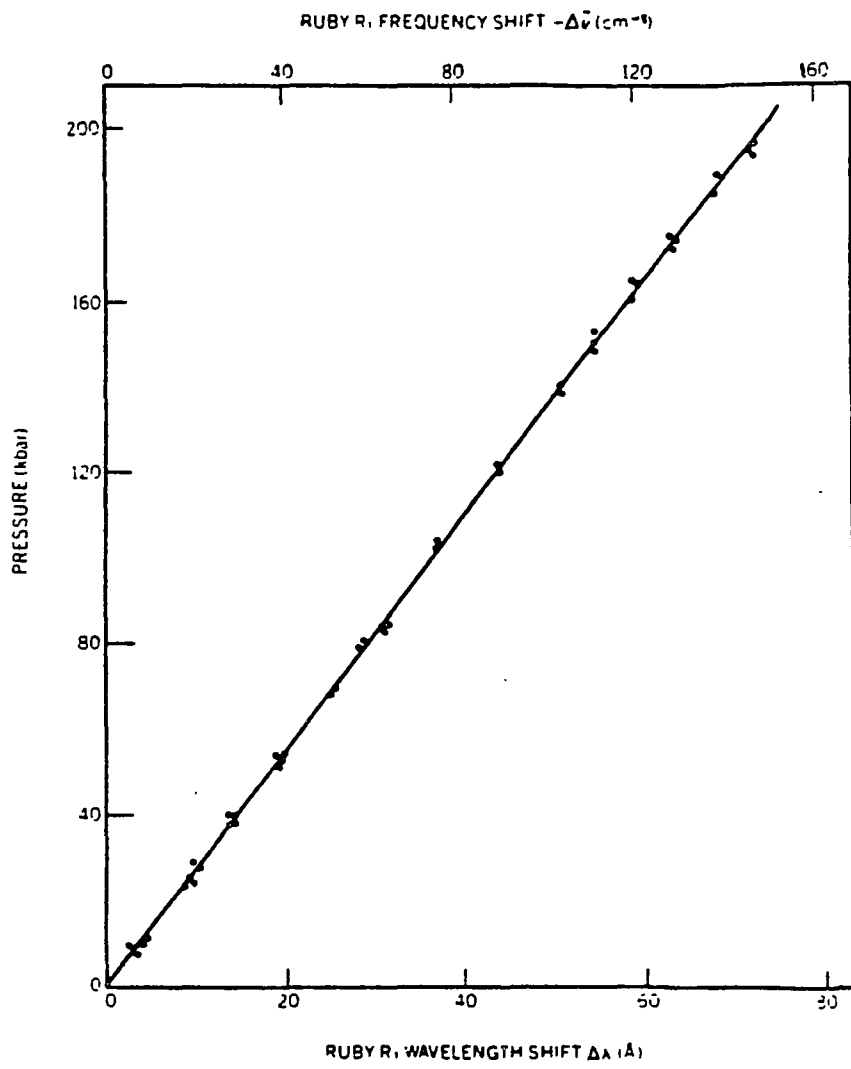


Figure 16: Systematic variation of fluorescence lines R1 of the ruby with respect to the applied pressure.

High-pressure experiments have to be performed with extreme care not only for the sake of dependable, reliable, and reproducible data, but also since any mishandling of the DAC will result in breaking of the diamond anvils. The diamond anvils are easily breakable if the faces of the diamonds are not perfectly aligned. Perfect alignment of anvil surfaces can be achieved with the help of the adjusting screws located on the sides of DAC. Under a microscope, illuminated with white light, interference fringes can be observed when the two diamond faces are nearly parallel to each other. On the other hand the appearance of Newton's rings indicate inclination between diamond surfaces. Newton's rings are concentric interference fringes (rings) formed by the construction and destruction of light waves from a monochromatic source.

The high-pressure Raman spectra shows band broadening and reduction of peak intensity as the pressure is increased (eg. Besson, et al., 1982., Kubicki, et al. 1992; Hofmeister, et al. 1989). Besson, et al; (1982) argued that the reduction in intensity in olivine is due to the small size of the sample in the diamond cell, low scattering efficiency of the samples and due to the choice of scattering geometry. The band broadening could be due the non-hydrostatic pressure in the sample chamber.

2.14 Low-temperature micro-Raman studies

Low-temperature experiments are conducted with a refrigeration system from CTI-Cryogenics (Model 22C Crydyne 1988). The main components of the refrigeration unit consists of a model SC/SCW compressor, a model 22 cold head and necessary cables and connectors (Fig. 17). Compressor uses helium as the refrigerant and filled with He to a pressure 230 psi before operation. Cold head is connected to the compressor and upon operation super cooled helium is circulated through the cold head, thus cooling it by taking away the heat from the tip of the head, like in a refrigerator. Tap water is used to cool the compressor. Temperature as low as 15 K can be achieved by this way. A

temperature controller attached to the tip of the cold head near the sample is used to monitor the temperature of the sample very accurately.

Cold head is enclosed in a vacuum seal in an aluminum case and placed under the microscope. Exciting laser beam is brought to the sample at 45 degree scattering geometry to the vertical through the window. The scattered Raman signal is collected using a 20x microscope objective focused at the sample vertically and focused onto the entrance slit of the spectrometer.

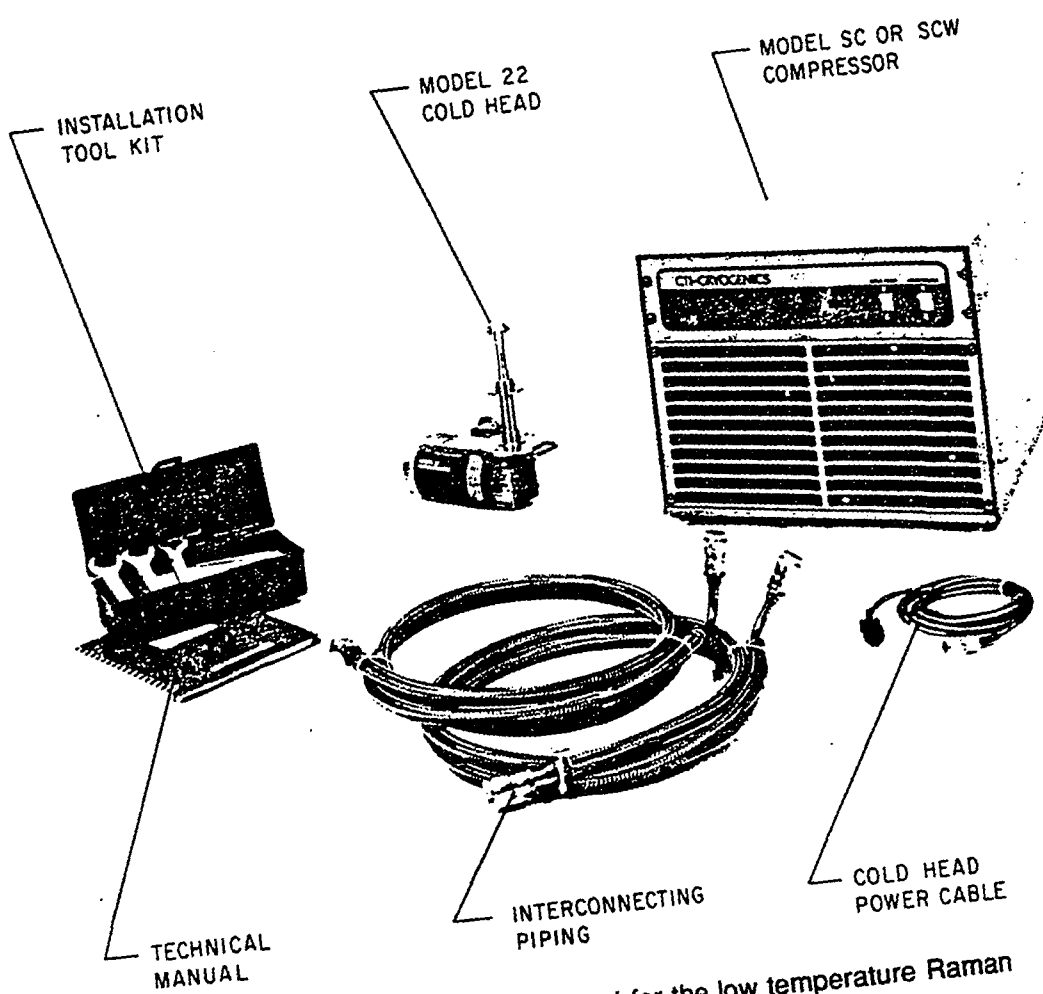


Figure 17: Various components used for the low temperature Raman scattering experiments.

CHAPTER 3

A RAMAN AND INFRARED STUDY OF THE FORSTERITE-MONTICELLITE SOLID SOLUTION SERIES

Olivines are considered to be one of the important constituents of the Earth's upper mantle and of meteorites. Among this large well-studied class of orthosilicates, forsterite is one of the most common mineral. In the ternary system containing forsterite (Mg_2SiO_4), fayalite (Fe_2SiO_4), and calcium olivine (Ca_2SiO_4), forsterite forms a complete solid solution with fayalite but not with the Ca-olivine. In fact, under ambient conditions, it does not form a complete solid solution series with the intermediate isostructural monticellite, $CaMgSiO_4$ (Biggar and O'Hara, 1969; Brown 1980). Knowledge of the structural behavior, such as cation disorder caused by cation substitution, is important to our understanding of geochemical and petrological systems. Adams and Bishop (1985) have studied poly-crystalline samples of Fo-Mo solid solution series samples with X-ray diffraction techniques and detected only a small degree of Ca-Mg disorder.

As mentioned in chapter 1, vibrational frequencies are very sensitive to the interatomic forces. Raman and infrared (IR) spectroscopy could thus reveal small changes in bond lengths and bond angles of crystals responding to changes in composition, temperature, and pressure. These techniques have been used for both quantitative and qualitative analyses of minerals (Farmer, 1974; White, 1976), and especially the vibrational spectra of olivine have been extensively studied. Tarte (1963) and Burns and Huggins (1972) investigated IR spectra of several olivines. Huggins (1973) used vibrational spectra as a tool to study cation ordering in olivine. Servoin and Piriou (1973) investigated both IR and Raman spectra of the solid solutions of $(Mg_{1-x}Ni_x)_2SiO_4$ and $Mg_2(Si_{1-x}Ge_x)O_4$ and identified various vibrational modes. Piriou and

McMillan (1983) studied the high frequency Raman spectra of several orthosilicates and investigated the nature of the ν_1 and ν_3 mixing characteristics. Iishi (1978) and Lam et al., (1990) modeled interatomic forces in Fo using single crystal vibrational data. Chopelas (1991) measured polarized single crystal spectra of forsterite, fayalite, and monticellite and refined the existing observed vibrational data, but little work has been done on the effect of cation disorder on Raman spectra. Isotopic exchange experiments on orthosilicates (Paques-Ledent and Tarte, 1973) showed inconsistency in the assignments of the high frequency vibrational modes. These workers concluded that there is strong coupling between the ν_1 and ν_3 modes in the vibrational spectra of orthosilicates. Recent theoretical work by Lam et al. (1990) showed that the ν_1 and ν_3 mixing in orthosilicates could be explained by considering both the corresponding average Si-O bond length ($\langle \text{Si-O} \rangle$) and the ratio of the average intra O-O distance ($\langle \text{O-O} \rangle$) to the corresponding $\langle \text{Si-O} \rangle$ bond distance. In this work the fo-mo samples used in the previous X-ray studies have been studied with Raman spectroscopy to determine structural implications of systematic variations of composition, mixing characteristics of the high frequency modes, and order-disorder phenomena. Raman spectroscopy has been used for the analysis of the samples along the fo-mo join because the Raman spectra of crystalline materials usually give rise to well defined narrow bands and, therefore, both the frequencies and band widths can be used for examining effect of composition and degree of disorder.

3.1 Experimental methods

The samples were synthesized under high pressure in a piston-cylinder solid media apparatus and characterized with X-ray diffraction analysis (Adams and Bishop, 1985). Raman spectra of six polycrystalline forsterite-monticellite solid solution samples, ranging from 100 to 6 mol% Fo, were measured with a multichannel micro-

Raman spectrometer. The spectra were collected at a scattering geometry of 135° (Sharma and Urmos, 1987, Sharma, 1989). The samples were excited using a 488 nm laser line from a Spectra Physics Model 165 Ar+ ion laser. Laser power at the sample was 20 mW. A spectral resolution of 4 cm⁻¹ was used. Detailed of the experimental set up is described in chapter 2.

3.2 Factor group analysis

Olivine has an orthorhombic structure and belongs to the space group Pbnm (point group D_{2h}; Z=4). The crystal structure of olivine with Pbnm space group is given in Fig. 18. Factor group analysis predicts the following 84 normal modes for this structural group (e.g., Lam et al., 1990):

$$\Gamma_{\text{total}} = 11 \text{ A}_g (\text{R}) + 11 \text{ B}_{1g} (\text{R}) + 7 \text{ B}_{2g} (\text{R}) + 7 \text{ B}_{3g} (\text{R}) + 10 \text{ A}_u (\text{ia}) + 10 \text{ B}_{1u} (\text{IR}) + 14 \text{ B}_{2u} (\text{IR}) + 14 \text{ B}_{3u} (\text{IR})$$

where R indicates Raman active; IR, infrared active, and the ia, inactive modes. Table 7 gives the normal vibrational modes and their assignments predicted by factor group analysis. Table 8 lists all the observed bands in some of the major olivine crystals. The frequencies of the observed Raman spectra of polycrystalline powdered samples of Fo-Mo solid solution series are given in Table 9. Observation of fewer than anticipated Raman bands of the powdered samples is attributed to the weak intensities of some bands, as well as to accidental degeneracies of the bands, including the tendency of weak bands to merge with adjacent bands. As mentioned earlier, samples between Fo 18 wt% and Fo 84 wt% are not stable (Fig. 19). To the best of the author's knowledge no vibrational data has been reported for these compositions.

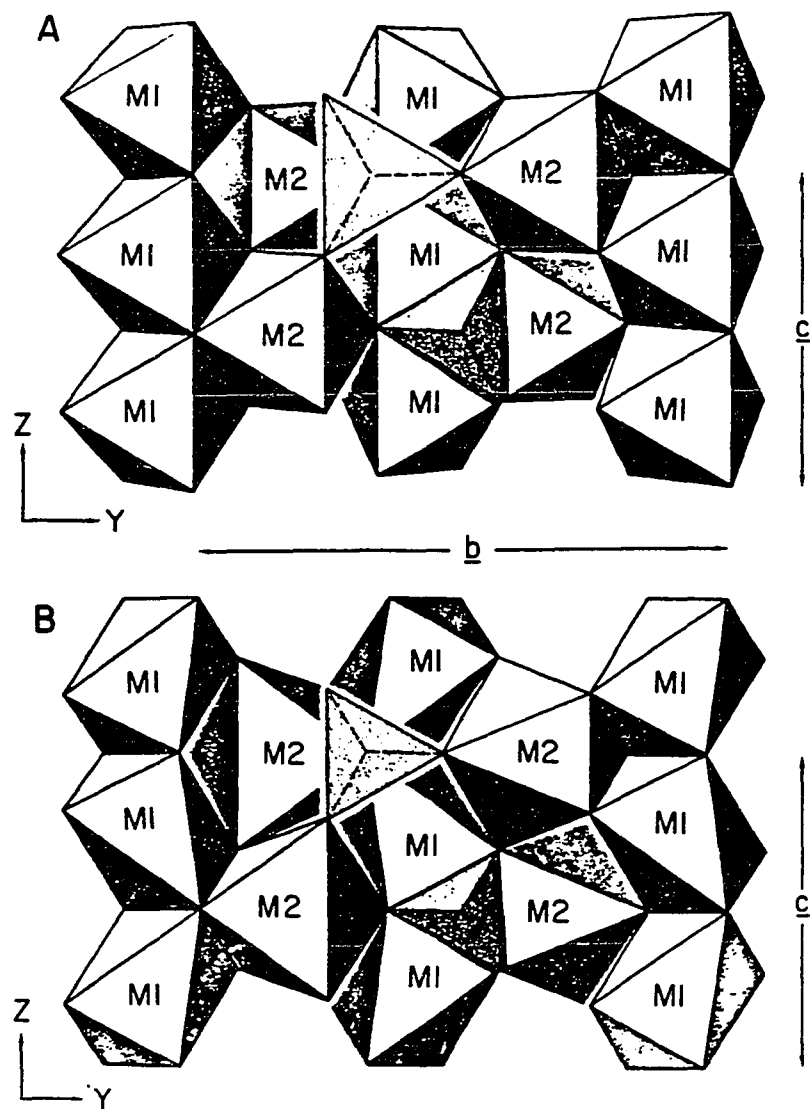


Figure 18: Crystal structure of Pbnm type Olivine structure showing the tetrahedral and octahedral sites. a)ideal case b) real case.

Table 7: Table showing the space group, ions, sites, various Raman and infrared modes in olivine crystal structure

Space Group			$Pbnm(D_{2h}^{16}), Z=4$							
Ions	Site	Modes	Raman				i.a.	Infrared		
			A_g	B_{1g}	B_{2g}	B_{3g}		B_{1u}	B_{2u}	B_{3u}
Mg I	C_i	A_g	-	-	-	-	-	-	-	-
		A_u	-	-	-	-	3	3	3	3
Mg II	C_s	A'	8	8	-	-	-	-	8	8
Si		A''	-	-	4	4	4	4	-	-
20	C_1	A	3	3	3	3	3	3	3	3
Number of Modes			11	11	7	7	10	10	14	14

Table 8 Experimentally observed Raman bands in
various olivines, their mode assignment
and Gruenesian parameters

$F_{O_{100}}$	γ_i	$F_{O_{90}}$	Mo	Fa	Ts	$\gamma \cdot Ca_2$	Assignment
A_{1g}							
965	0.66	961	949	932	935	925	ν_3
856	0.44	854	851	840	840	839	$\nu_1 + \nu_3$
824	0.48	822	818	814	808	814	$\nu_1 + \nu_3$
608	0.70	606	589	562	575		ν_4
545	0.53	542	534	505	515		ν_4
422	1.48	417	402	369	389		ν_2
339	1.87	334	275	237	258		M2 translation
329	1.16	326	307	289	291		SiO ₄ rotation
304	1.63	301	258	259	244		M2 translation
228	0.67	222	172	171	167		SiO ₄ translation
183	2.1	181	145	119	124		SiO ₄ translation
B_{1g} (xy)							
975		973	954	947	—		ν_3
866		864	855	851	—	849	$\nu_3 (+ \nu_1)$
838		836	828	822	820		$\nu_1 (+ \nu_3)$
632		630	600	577	588		ν_4
582	0.66	578	560	524	546		ν_4
434	1.4	429	407	384	393		ν_2
383		379	333	312	307		M2 translation
351		348	303	2777	288		M2 translation
318		314	266	260	271		SiO ₄ rotation
274		—	215	193	203		SiO ₄ translation
220		215	164	154	155		SiO ₄ translation
B_{1g} (xz)							
881	0.44	880	879	860	—		ν_3
586		582	572	553	553		ν_4
439	1.6	433	411	405	401		ν_2
365		355	327	309	319		mix (SiO ₄ , rot)
323		314	263	290	274		mix (M2 trans)
242	1.21	236	243	189	188		mix (SiO ₄ , rot)
175		—	141	102	119		mix (SiO ₄ , trans)
B_{3g} (yz)							
920	0.38	917	899	900	892	887	ν_3
592		589	578	549	555		ν_4
435		427	332	—	304		mix (SiO ₄ , rot)
410	0.99	404	399	376	378		ν_2
374	1.75	368	266	281	276		mix (M2 trans)
315		312	251	188	223		mix (SiO ₄ , rot)
286		282	216	113	137		mix (SiO ₄ , trans)
43.65			51.58	46.15	48.61	59.11	V_0^{eq} ($\text{cm}^2 \text{ mol}^{-1}$)**
0.203			0.189	0.178	0.134	0.158	$1/\sqrt{M}$

Table 9 Observed Raman frequencies for the Fo-Mo
solid solution series

Mode	Fo ₁₀₀	Fo ₉₃	Fo ₈₈	Fo ₈₄	Fo ₁₈	Fo ₁₄	Fo ₆	Mo*
Ag	964.0 (m)	963.1 (m)	961.7 (m)	961.7 (m)	949.7 (m)	949.7 (m)	948.4 (m)	949.0
B3g	919.0 (w)	917.7 (w)	916.3 (w)	915.0 (w)	901.6 (m)	900.2 (m)	898.9 (m)	900.0
Ag	855.0 (vs)	854.5 (vs)	853.2 (vs)	851.8 (vs)	847.8 (vs)	847.8 (vs)	850.5 (vs)	851.0
Ag	824.0 (s)	822.0 (s)	819.5 (s)	818.1 (s)	816.8 (s)	816.8 (s)	816.8 (s)	818.0
Ag	608.0 (w)	606.0 (w)	604.0 (w)	603.9 (w)	595.0 (w)	592.0 (w)	589.0 (w)	589.0
B1g+B2g+B3g	589.0 (w)	586.8 (w)	586.1 (w)	586.3 (w)	575.2 (w)	580.0 (w)	580.0 (w)	560.0
Ag	544.0 (w)	544.0 (w)	543.7 (w)	544.3 (w)	575.3 (w)	578.0 (w)	578.0 (w)	534.0
B1g+B2g+B3g	433.5 (w)	432.1 (w)	429.4 (w)	427.9 (w)	415.0 (s)	413.0 (s)	409.5 (s)	407.0
B3g	374.0 (w)	369.1 (w)	368.0 (w)	367.8 (w)	-----	-----	-----	266.0
Ag	337.0 (w)	333.0 (w)	327.4 (w)	327.3 (w)	336.3 (w)	337.0 (w)	337.0 (w)	275.0
Ag	329.0 (w)	-----	-----	-----	-----	-----	-----	307.0
B3g	314.0 (vw)	-----	-----	311.6 (w)	313.6 (w)	313.6 (w)	307.5 (w)	251.0
Ag	303.0 (w)	298.6 (w)	297.2 (w)	295.9 (w)	261.6 (m)	260.9 (m)	256.8 (m)	258.0
Ag	225.0 (w)	223.0 (w)	216.5 (w)	216.5 (w)	-----	-----	214.4 (w)	172.0

vs=very strong; s=strong; m= medium; w=weak; vw=very weak

*Data from Chopelas (1991)

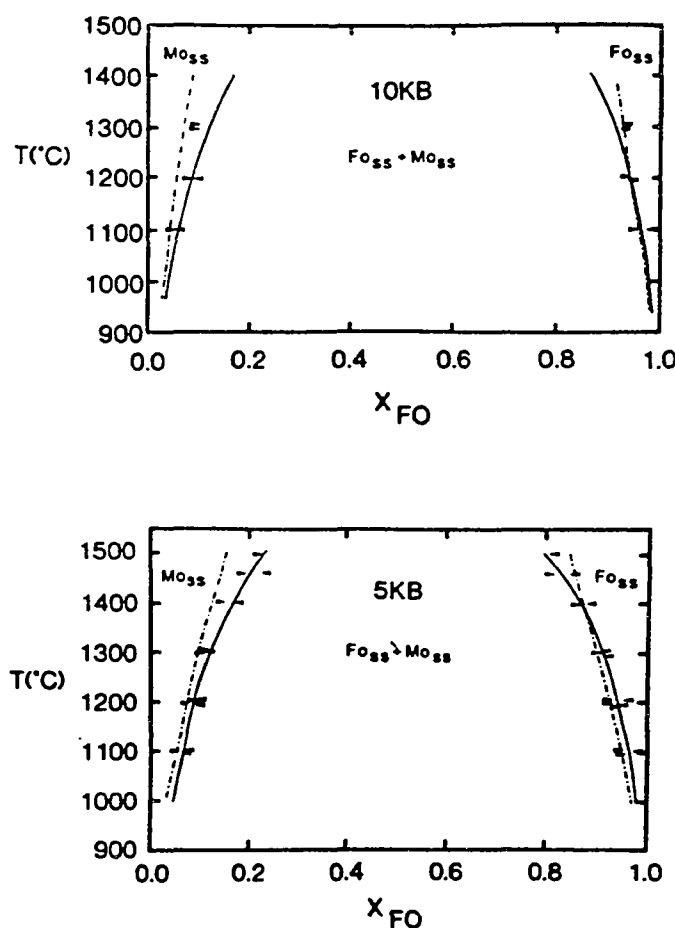


Figure 19: Miscibility gap at 5 kbar and 10 kbar in the forsterite-monticellite system (after Adams and Bishop, 1985).

3.3 Results and discussion

3.3.1 High-frequency Raman spectra

The Raman spectra of Fo-Mo solid solution series in the 100-1000 cm⁻¹, are shown in Fig. 20. For better understanding of the vibrational spectra, a detailed configuration of the olivine crystal structure is considered in Figs. 21a and 21b. Fig. 21a shows a schematic diagram of the SiO₄ tetrahedra and its immediate cation environment. In Fig 21b various vibrational modes of SiO₄ tetrahedra are shown. Fig. 22 gives the expanded portion of the Raman spectra in the 700-1000 cm⁻¹ region. A very weak shoulder at 880 cm⁻¹ is visible in the spectra of the Fo-rich end, but it merges with the 855 cm⁻¹ band in the Mo-rich end. Another weak feature seen at 749 cm⁻¹ in the Mo-rich end is not present in the Fo-rich olivine (Fig. 21). The striking feature of these bands is the systematic variation of the frequency with composition. For example, starting from Fo-rich olivine to Mo-rich olivine, the bands at 824, 855 and 964 cm⁻¹ shift toward lower frequencies by approximately 5.4, 8.1, and 16 cm⁻¹, respectively. This systematic frequency shift is largely due to the increase in the inter-tetrahedral O-O bond lengths as a result of the substitution of larger cations in the M2 sites (see below). The X-ray data (Adams and Bishop, 1985) indicate an increase up to 19% in the unit cell volume from the Fo-rich to Mo-rich olivine. Replacement of Mg cations with Ca at the M2 site causes increases in the unit cell parameters; in turn, the inter-tetrahedral O-O distance increases and SiO₄ tetrahedra become more 'relaxed' (Lam et al., 1990). At the forsterite end, Raman frequency decreases linearly with composition, whereas in the monticellite end the Raman frequency increases, resulting in a reverse trend (Fig. 23).

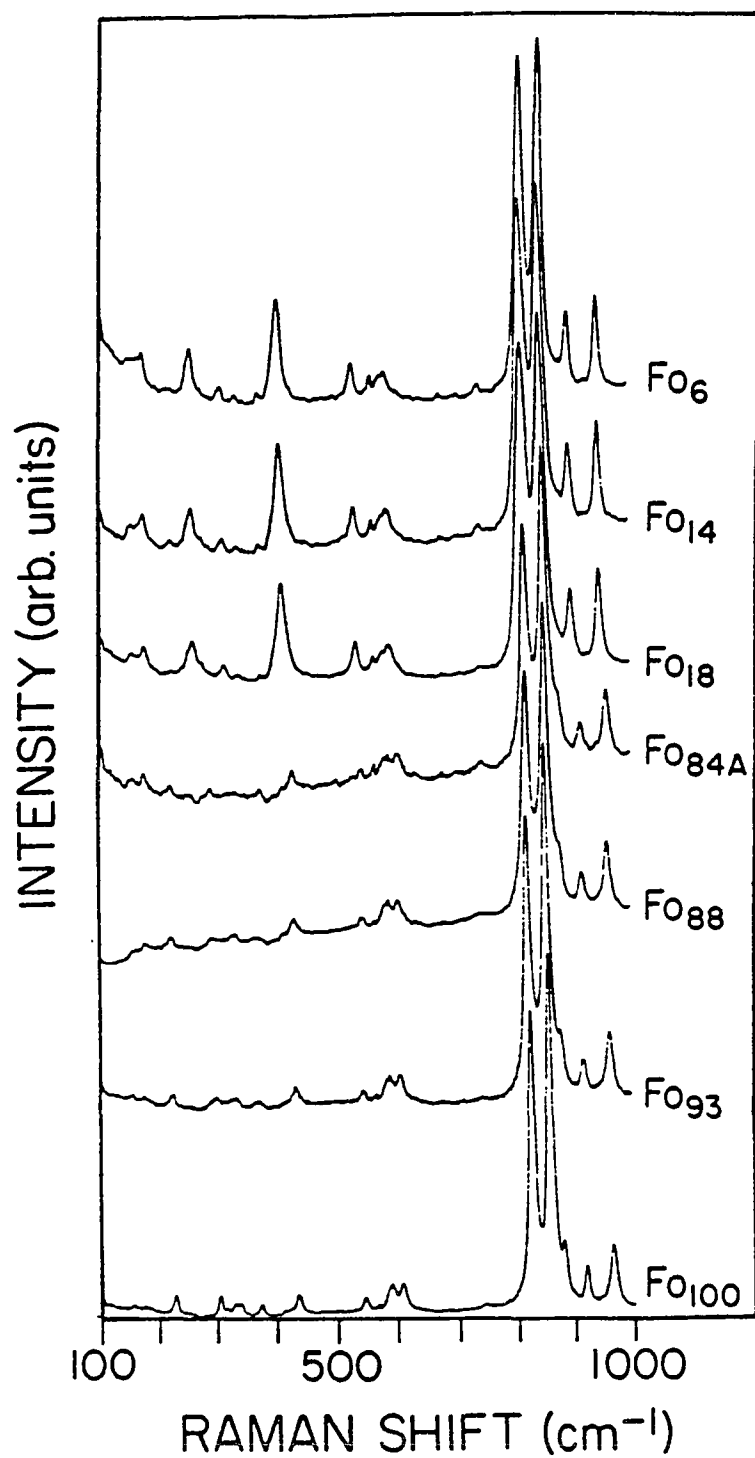


Figure 20: Raman spectra of Forsterite - Monticellite (Fo100%-Fo6%) solid solution series in the 100-1000 cm⁻¹ region.

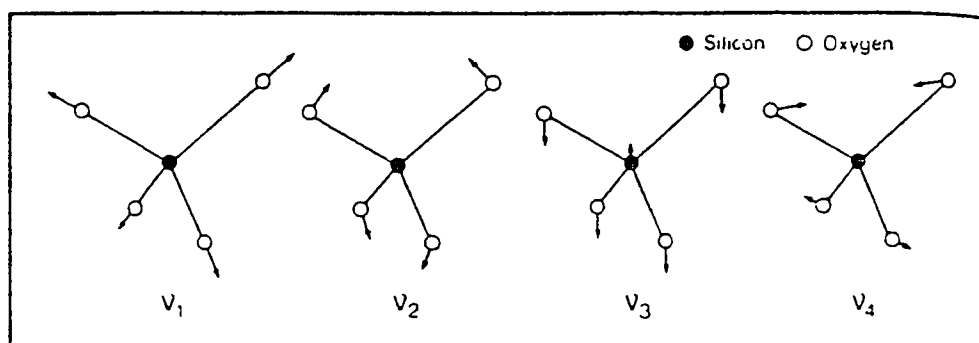
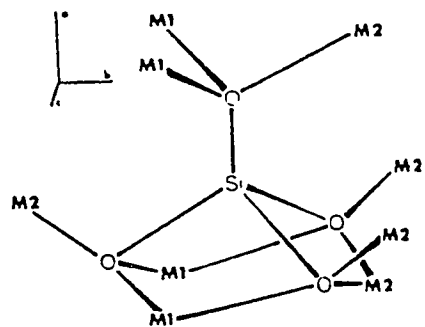


Figure 21: a) Schematic diagram showing the position of silicon with respect to the various oxygen and the cations in the M1 and M2 octahedral coordinations. b) Above diagram illustrates the symmetric and anti-symmetric stretching silicon and oxygen atoms in an isolated SiO_4 tetrahedral unit (after Price et al., 1976).

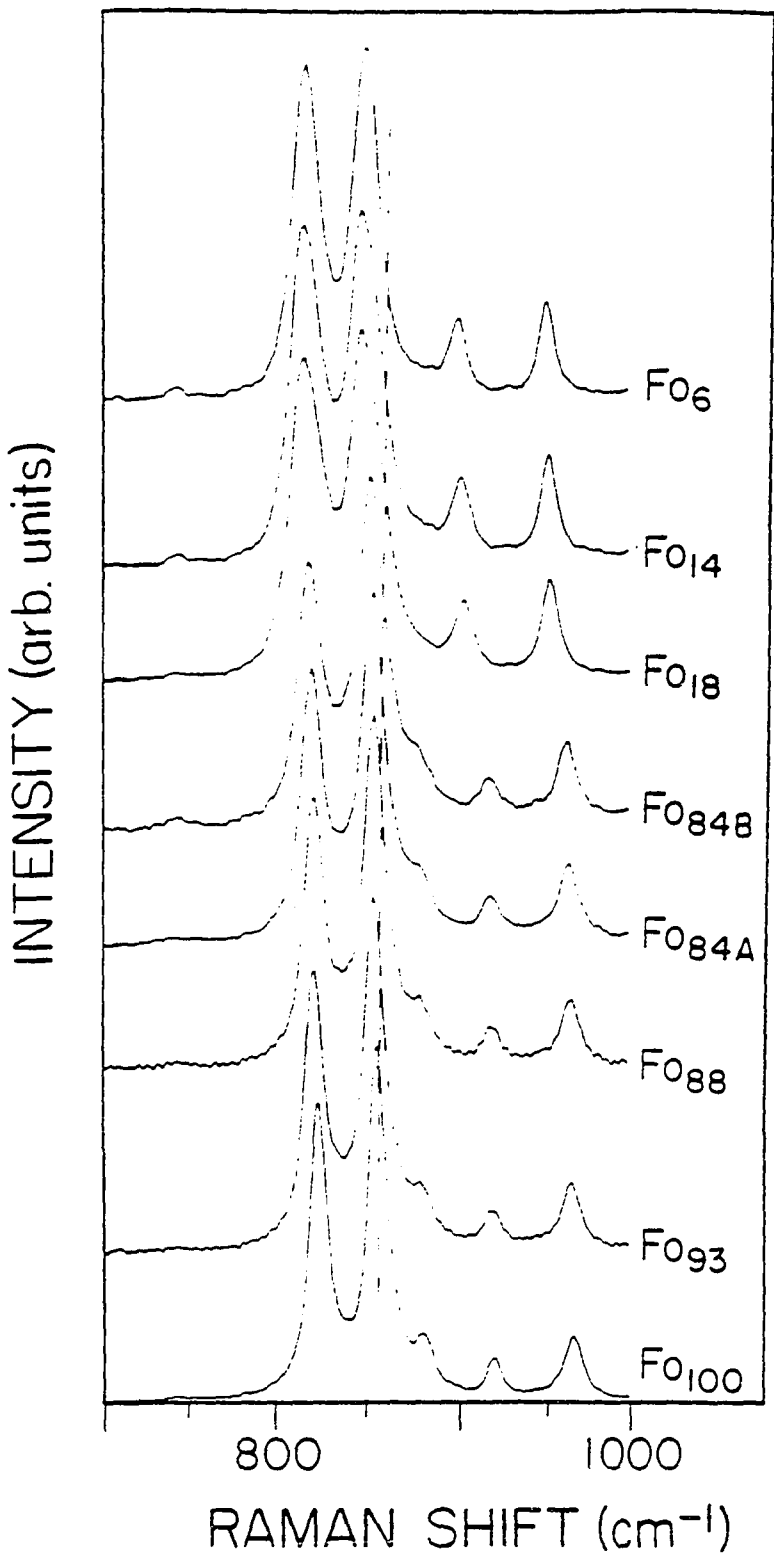


Figure 22: Details of the Raman spectra of Fo-Mo solid solution series in the high frequency region (700-1000 cm⁻¹)

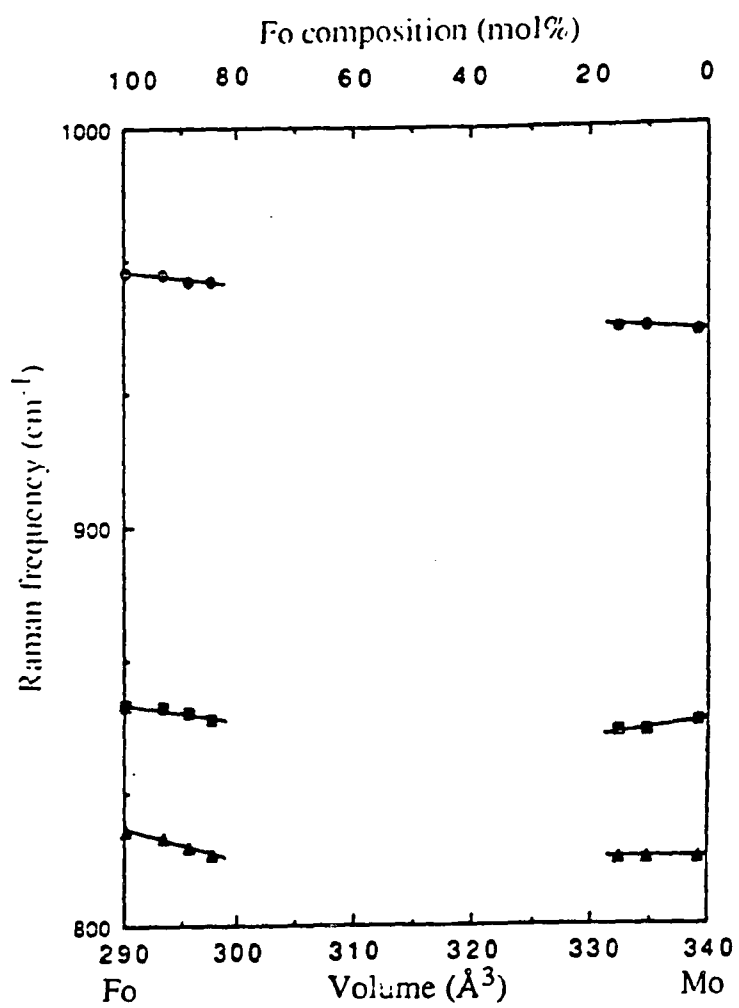


Figure 23: Plot of the high frequency vs unit cell volume. Sample composition is given at the top of abscissa. (Legends: $\ominus = 964 \text{ cm}^{-1}$; $\blacksquare = 855 \text{ cm}^{-1}$; and $\blacktriangle = 824 \text{ cm}^{-1}$.

The coefficients of a linear fit to our data are given below. For convenience, the equations are normalized to their respective end-member volume.

forsterite-rich composition

$$\nu_1 = 963.99 - 0.343V \quad R = 0.963$$

$$\nu_2 = 855.34 - 0.432V \quad R = 0.954$$

$$\nu_3 = 824.17 - 0.822V \quad R = 0.995$$

monticellite-rich composition

$$\nu_1 = 948.50 + 0.205V \quad R = 0.939$$

$$\nu_3 = 850.29 + 0.426V \quad R = 0.939$$

$$\nu_2 = 816.80 \quad \text{constant wrt volume}$$

where V is the unit cell volume in the range 290-340 Å³. The non-linear behavior of the high-frequency bands are due to the complex nature of vibrations of the SiO₄ tetrahedra that exist in the family of olivines (Piriou and McMillan, 1983). The linear correlation coefficients (R) for Mo are not very high, indicating that frequency variation of coupled ν₁-ν₃ modes with volume are not linear.

Let us consider the behavior, and characteristics of the high-frequency bands in the Fo-Mo solid solution series. The bands of interest of Fo in this study are the two intense A_g modes at 855 cm⁻¹ and 824 cm⁻¹ and the medium band at 964 cm⁻¹, originating from the stretching modes of SiO₄ tetrahedra. The lattice dynamics of Fo have attracted the attention of a number of workers (e.g; Price and Parker 1984, Price et al., 1987., Rao et al., 1987, Lam et al., 1990). It is proposed that the band at 964 cm⁻¹ contains large contributions from Si-O(1) bond stretch (Lam et al., 1990). The stretching bands at 855 cm⁻¹ and 824 cm⁻¹ originate largely from Si-O(3) and Si-O(2) bonds, respectively. Their frequencies and halfwidths vary systematically with the cation content.

In general, the observed frequency of a bond-stretching vibration mode is inversely proportional to the corresponding bond length. In solids, however, such a

simple relationship may not be strictly valid because of near-neighbor interactions and crystal field effects. Table 10 lists the Si-O bond lengths, the ratio of average inter O-O distances to the Si-O bond distances, and the observed Raman frequencies in forsterite, monticellite and Ca-olivine. It is evident that within each of these minerals, a given vibrational band varies strongly as a function of corresponding inverse bond length. For example, in forsterite, this dependence is clear: for bond lengths Si-O(1) (1.620 Å), Si-O(3) (1.636 Å), and Si-O(2) (1.656 Å), the corresponding frequencies are 964, 855 and 824 cm⁻¹, respectively. But among other olivine crystal structures, a simple consideration the Si-O bond lengths alone does not explain the observed frequencies (Fig. 24). For the present sample compositions, an extrapolation of the frequency between the end members gave a parabolic fit (Fig. 25) with a minimum frequency value of 846.5 cm⁻¹. This is far from a linear approximation if we consider corresponding bond length alone. To resolve this dilemma, Piriou and McMillan (1983) investigated the high-frequency vibrational spectra of several orthosilicates. They studied the vibrational coupling of the ν_1 and ν_3 modes by considering simple harmonic oscillators. Their simple theoretical model showed that the high-frequency vibrational modes vary with some physical parameter 'X'. They found that the strong band A_g at 856 cm⁻¹ in forsterite has more ν_1 character, whereas in the monticellite spectrum the band at 814 cm⁻¹ has more ν_1 character. In the class of orthosilicates, the monticellite lies next to the crossover between ν_1 and ν_3 modes (Fig. 26). So it has been suggested that in monticellite the mixing characteristics of ν_1 and ν_3 modes are more or less equal and forsterite and Ca-olivine are at the extreme ends (Piriou and McMillan, 1983).

The simple theoretical model of Piriou and McMillan (1983) explained the behavior of the ν_1 and ν_3 modes of olivines, but the relationship of the physical parameter 'X' to the crystal structure was not clear. Lam et al. (1990) theoretically simulated the forsterite structure using a pair-potential model by taking into account

Table 10: Table containing observed Raman frequencies,
bond length, and bond ratio

BOND	Fo			Mo			Ca		
	Bond Length (Å)	$\frac{\langle O-O \rangle}{Si-O}$	Frequency (cm ⁻¹)	Bond Length (Å)	$\frac{\langle O-O \rangle}{Si-O}$	Frequency (cm ⁻¹)	Bond Length (Å)	$\frac{\langle O-O \rangle}{Si-O}$	Frequency ^a (cm ⁻¹)
Si-O ₁	1.620	1.840	964.0	1.615	1.957	949.0	1.637	2.0504	925.0
Si-O ₃	1.636	1.822	856.0	1.640	1.927	851.0	1.642	2.0442	839.4
Si-O ₂	1.656	1.800	824.0	1.656	1.908	817.0	1.665	2.0159	813.6

62

^aData from Piriou and McMillan (1983).

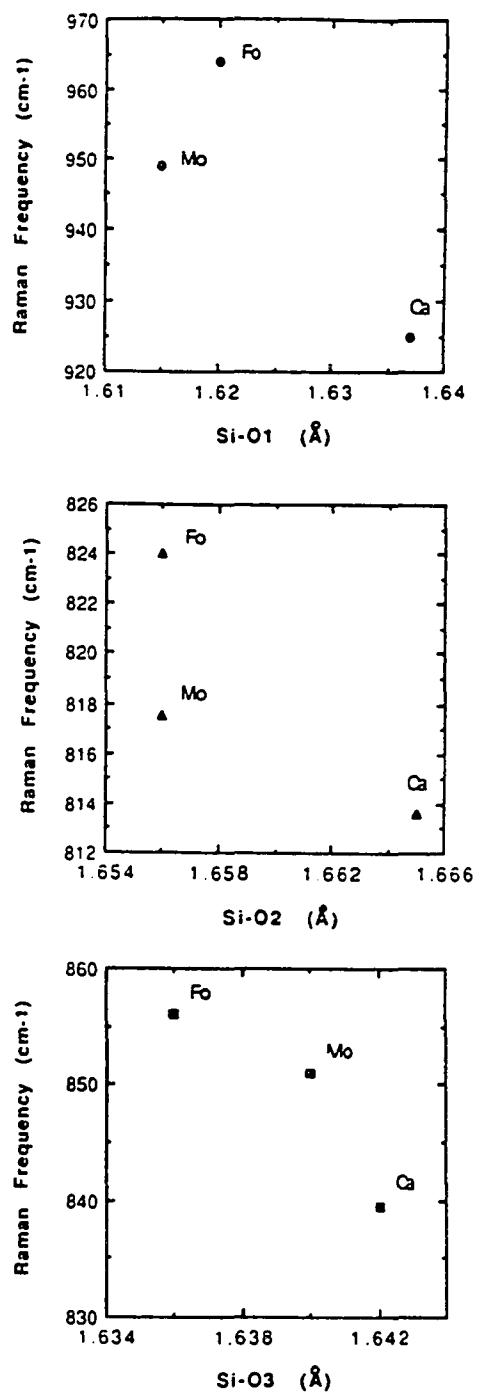


Figure 24: Plot of the three major Raman modes of three olivines with respect to the corresponding to the Si-O bond length.

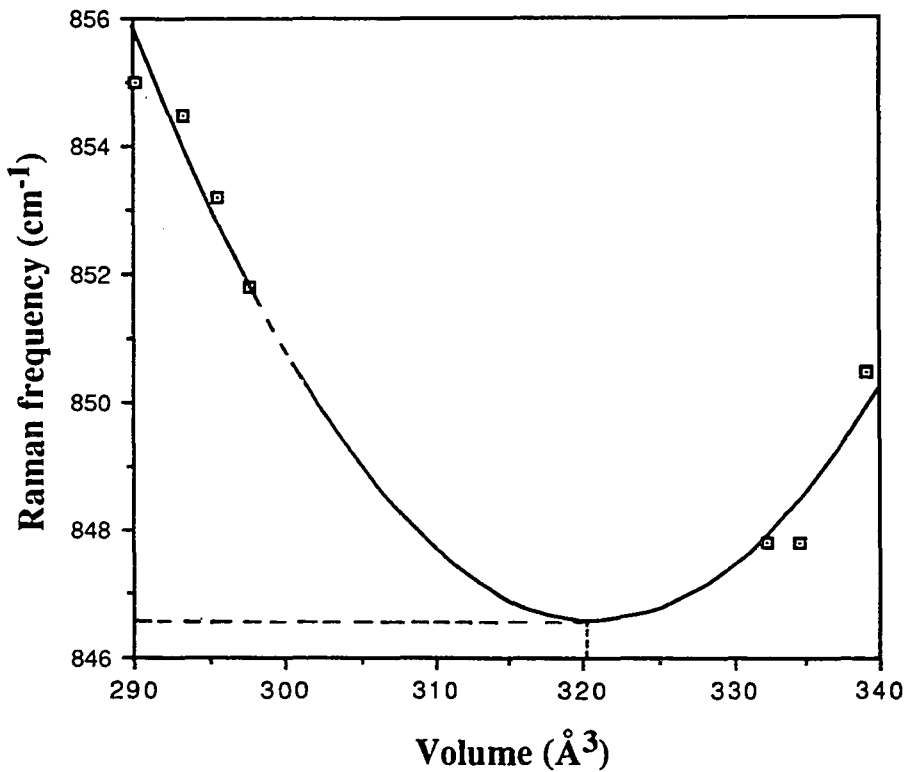


Figure 25: The 855 cm^{-1} Fo100% band is fitted to a parabolic curve showing the possible frequency-volume behavior between the miscibility gap

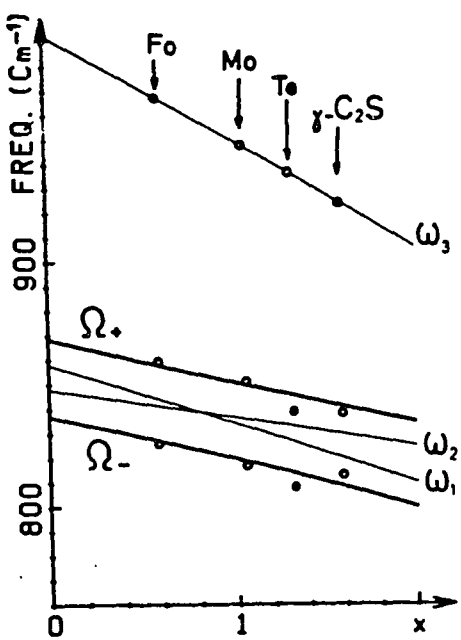


Figure 26: Coupling behavior of high-frequency modes (A_g and B_{1g} modes) in olivine crystals. For details of the mode behavior see the text (after McMillian , 1983).

the ionic and covalent interactions, as well as the core-core repulsion forces. Their model shows that the high frequency ν_1 and ν_3 modes in olivine are not only affected by the variations of the Si-O bond but also by the variation of inter-tetrahedral O-O interactions. Lam et al., (1990) showed that the inter-tetrahedral O-O distance varies by 10% with the substitution of larger cations. They proposed that the intensity of ν_1 and ν_3 mixing is attributed to the net effect of the inter-tetrahedral $\langle O-O \rangle$ force constant and the Si-O force constant. They calculated the ratios of inter- $\langle O-O \rangle$ to $\langle Si-O \rangle$ distances for forsterite, monticellite and Ca-olivine and tabulated them along with the Si-O bond lengths and their corresponding frequencies (see Table 10). It is noted that for a given composition, both across and down the table, the lower the value of this ratio the higher the Raman frequency. When a larger cation is substituted into the forsterite structure, Si-O bond length increases and the relative degree of covalency of the bond decreases. Moreover, the intra- and inter- $\langle O-O \rangle$ distances increase. A plot of the Raman frequencies 964, 855 and 824 cm^{-1} of Fo and corresponding band frequencies of Mo and Ca-olivine versus the sum of the corresponding Si-O bond length to the Si-O(1) bond length and the ratio of inter- $\langle O-O \rangle$ to $\langle Si-O_n \rangle$, (where $n=1,2,3$) distances in the respective mineral shows a good linear trend with forsterite having the highest value of these modes and Ca-olivine having the lowest (Fig. 27). The present Raman data on Fo-Mo solid solutions are, therefore, are in agreement with predictions of Lam et al. (1990).

3.3.2 Low-frequency Raman spectra

Raman spectra of the Fo-Mo series in the low-frequency region, 100-700 cm^{-1} (Fig. 28) show band broadening, systematic decrease in frequency, and merging of adjacent bands. Frequencies of these bands shift toward lower wave numbers as the composition of the solid solution varies across the Fo-Mo join. The bands are fairly sharp in the Mo-rich samples but broad in the Fo-rich samples.

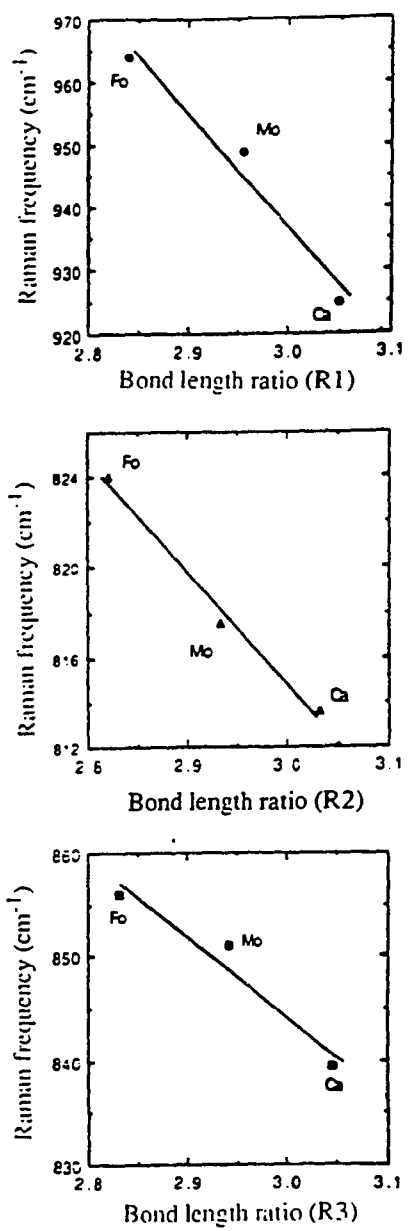


Figure 27: The dependence of high frequency bands in olivines on the sum of the ratio of Si-O bond lengths to the Si-O(1) bond length and the ratio of inter-tetrahedral to the Si-O bond lengths. Bond length ratio: $R1 = (\text{Si-O}(1))/(\text{Si-O}(1)) + <\text{O-O}>/(\text{Si-O}(1))$; $R2 = (\text{Si-O}(2))/(\text{Si-O}(1)) + <\text{O-O}>/(\text{Si-O}(2))$; and $R3 = (\text{Si-O}(3))/(\text{Si-O}(1)) + <\text{O-O}>/(\text{Si-O}(3))$.

In vibrational spectroscopy, the half width of a band is used to study positional disorder in crystal structures. Two strong bands at 434 cm^{-1} and 545 cm^{-1} are assigned respectively as a B_{1g} mode and an A_g type modes (see table 8) originating from ν_4 vibrations. We have selected these bands, because these are relatively strong in intensities and have flat baseline for half width calculations. Even though the band at 434 cm^{-1} could be a combination of $B_{1g}+B_{2g}+B_{3g}$ modes, in the spectra of polycrystalline samples the intensities of B_{2g} and B_{3g} modes are usually much weaker than that of B_{1g} mode and, therefore, the selection of the 434 cm^{-1} band for half width calculation is justifiable. On addition of calcium these bands shows broadening in the Fo-rich samples and narrowing in the Mo-rich samples. For example, at the forsterite end the 434 cm^{-1} band has a half width of 11.5 cm^{-1} and it increases by seven wave numbers with the addition of 16 mol% calcium (Fig. 28). On the other hand, in the Mo-rich end, its half width decreases by one wave number with the addition of 8 mol% calcium. The same behavior is observed with the 545 cm^{-1} band. This unusual behavior can be explained on the basis of order-disorder phenomena in the crystal. Positional disorder in binary olivine is caused by the occupancy of larger cations, such as calcium (ionic radii 1.0 \AA), in the smaller M1 site. In forsterite, the two structural sites M1 and M2 are of the same size. In monticellite the M2 site is larger than the M1 site. By preference, the larger cation (calcium) fills the M2 site and the smaller cation (magnesium) the M1 site. For this reason monticellite is a highly ordered mineral. The addition of calcium into the forsterite affects its crystal structure in two ways: the occupancy of either sites by calcium distorts the crystal structure and hence affects the SiO_4 tetrahedra; secondly, the presence of calcium in both M1 and M2 sites introduces positional disorder into the crystal structure. On the other hand, in the monticellite the M2 site is already big enough to accommodate the magnesium ion without affecting the crystal structure, but it does introduce disorder. For these reasons, the addition of

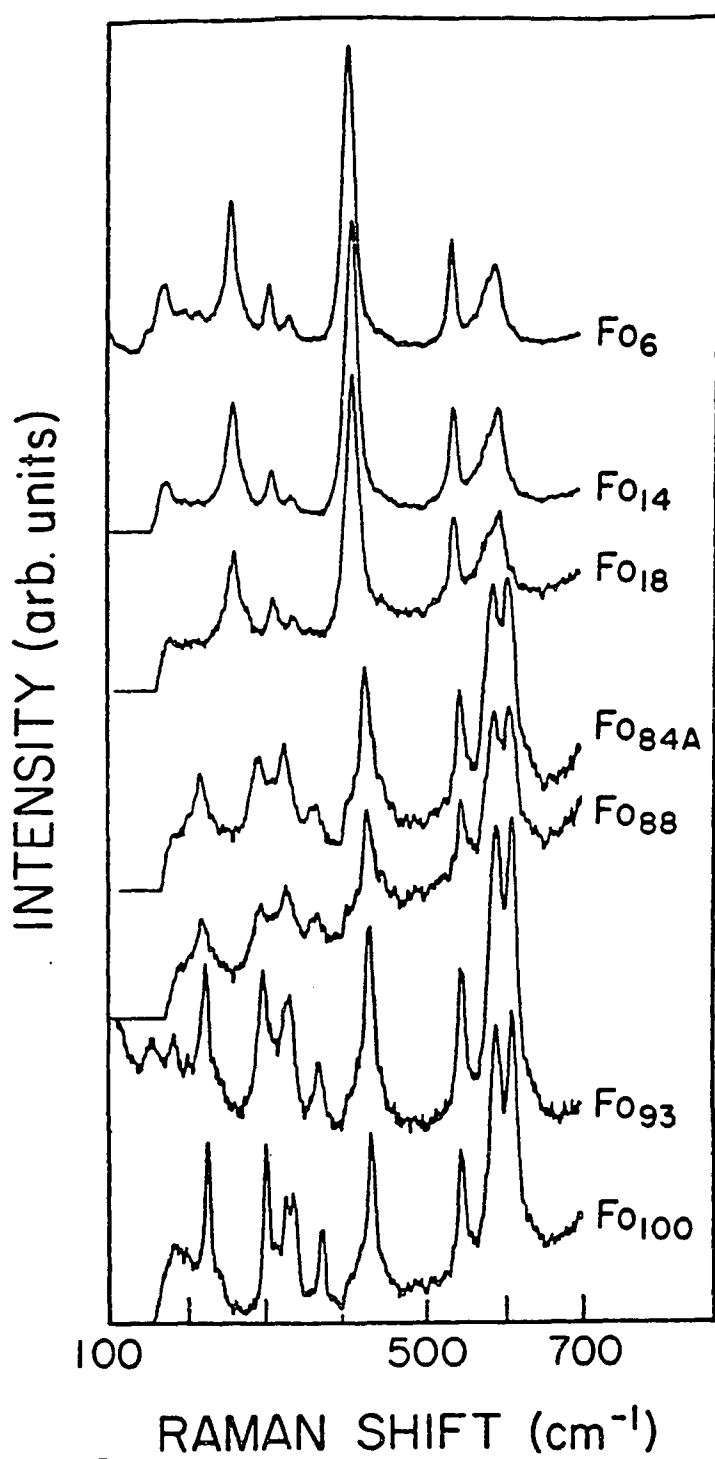


Figure 28: Raman spectra of forsterite-monticellite SS series in the low frequency region ($100\text{-}700 \text{ cm}^{-1}$)

calcium into the forsterite-rich composition causes considerable increase in the halfwidth of the Raman bands, whereas in the monticellite end, addition of magnesium causes only a slight increase in the halfwidth. Adams and Bishop (1985) calculated the presence of a maximum of 11% calcium in M1 site in the Fo-rich samples and 2% calcium in the Mo-rich samples. A comparison of the observed change (Fig. 29) in the slope of the bands of SiO_4 near the Fo-end to those of minerals near the Mo-end further indicates that Fo-rich olivines exhibit higher (Ca,Mg) disorder. Disorder in general tends to decrease the frequencies of the Raman bands.

In silicate solid solutions, one expects to observe a negative excess-volume effect (Newton and Wood, 1980). An example of such effect is shown in Fig. 30. The data from Adams and Bishop (1985), however, show a nearly linear relationship between the unit cell volume and composition across the given end-members. The absence of such excess-volume effects in these samples implies lack of positional disorder. The substitution of the larger calcium cation at the M1 site in the Fo-end causes the volume to increase linearly. However, it is, however, evident from Fig. 23 that the frequencies of the high-frequency bands of SiO_4 are not linearly dependent on unit cell volume along the Fo-Mo join.

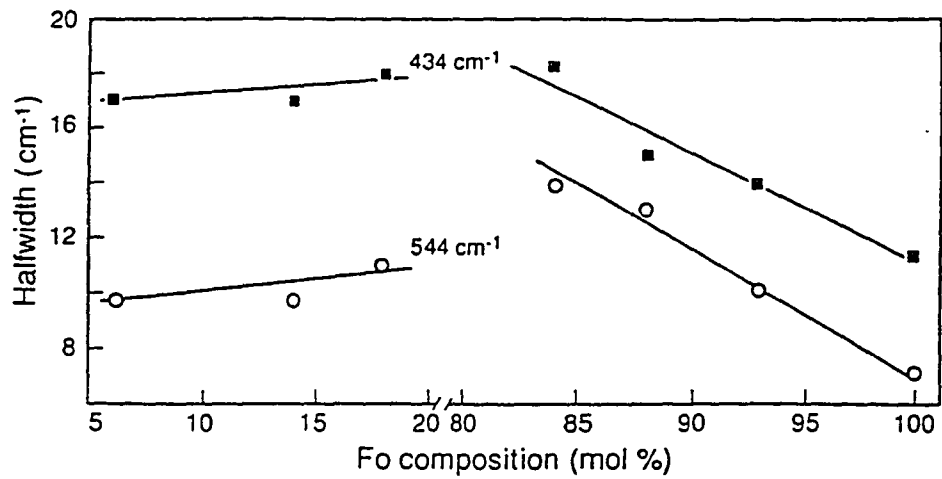


Figure 29: Behavior of halfwidth of two low frequency Raman bands
434 cm⁻¹ and 544 cm⁻¹ band.

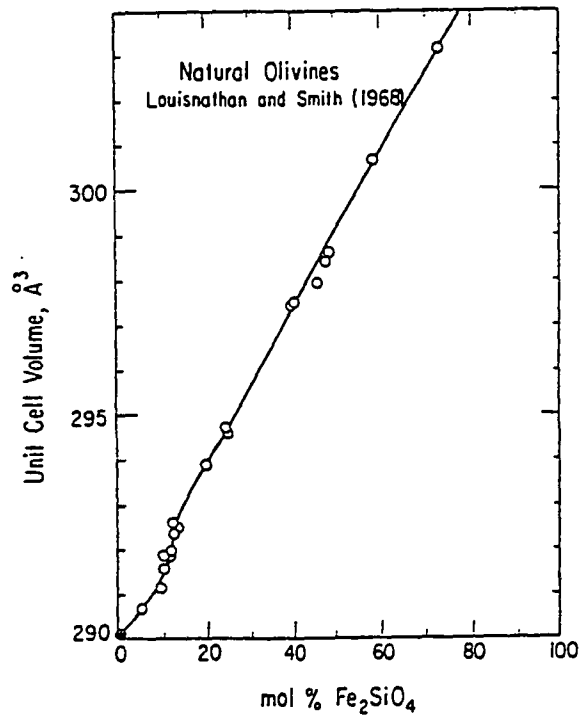


Figure 30: Unit cell volume of natural olivine in the Mg₂SiO₄-Fe₂SiO₄ joint (after Newton and Wood, 1980). In the present samples (Ca, Mg)SiO₄ this behavior is not observed.

3.4 High pressure studies of Fo-Mo series using Raman and infrared spectroscopy.

Olivines are a major constituent of the upper mantle. It is very well accepted that under high temperature and pressure olivine transform to spinel. Olivine has relatively an open crystal structure, orthorhobic, while spinel is compact and has an isometric crystal structure. The 400 km discontinuity in the Earth's mantle is believed to be the result of this transition (Green, 1984). Deep mantle melting and petrological setting of various mineral including olivine has been discussed by several authors (Hemley and Kubicki, 1990; Anderson, 1989). Therefore, it is important that we should study the properties of olivines under high pressures.

High-pressure experiments on forsterite has been done by several authors (Besson, et al., 1982; Kudoh and Takeuchi, 1985; Hofmeister, et al., 1989; Chopelas, 1990; Kubicki, et al., 1992; Wang, et al., 1992). Earlier experiments on forsterite crystals up to 65 kbars (Besson, et al., 1982) showed that the pressure induced changes in the high-frequency vibrational bands (except one band) originating from the stretching of SiO_4 tetrahedra are linear and the authors considered the properties of SiO_4 tetrahedra independent of their immediate environment. However, recent high-pressure experiments up to 240 kbars in diamond anvil cell reveal that the pressure induced systematic variation of some of the high-frequency as well as low-frequency vibrational bands are not always linear, but shows break in their linear slope with varying pressure, indicating some sort of changes in the crystal structure. Chopelas (1990) and Wang, et al., (1992) observed a break in the pressure derivatives (slope) for several vibrational modes in the forsterite crystal. Wang, et. al 1990) suggested

that this behavior is due to the change in the compressional mechanism in the crystal not a phase transition.

High-pressure data on forsterite, fayalite, tephrite, and Nickel olivine are available in the literature (Sharma, et al., 1992). However, high-pressure studies on calcium containing olivine has not been measured. One of the reason for the lack of study on this sample is that the calcium containing olivine is a high-pressure phase and it is a rare mineral in nature (see Fig. 19). Therefore, it is often necessary to synthesize calcium-rich olivines (Monticellite, CaMgSiO_4 or Larnite, Ca_2SiO_4) if one is interested in the study of its structural properties. Adams and Bishop (1985) have synthesized several composition of this high-pressure mineral and studied the structural properties with X-ray diffraction techniques. In the present study, one sample which is close to monticellite composition (Fo6%) is selected for high-pressure vibrational spectroscopy.

3.5 Experimental details

High-pressure Raman spectra were collected with a micro-Raman spectrometer. The sample was excited with a laser line 457.9 nm and the laser power at the sample was 20 mW. For good signal to noise ratio the spectra were collected with an exposure time of 1 minute, and 45 such scans were added. Detailed information on the high-pressure experimental setup is given in section 14 of chapter 2.

3.6 Sample description

Fo6% (CaMgSiO_4 , Mo 94%) sample in the solid solution series was used to do the high-pressure experiments. Sample was polycrystalline and in fine powder form. A very small amount of sample is loaded into the diamond anvil cell using tip of a pin. A small piece of ruby chip was also placed inside the cell. Small amount of pressure

transmitting medium, methanol-ethanol-water (16:3:1), was also added before the DAC was closed. One part of water was added to the methanol-ethanol mixture for methanol from solidifying at about 125 kbar.

3.7 Results and discussion

3.7.1 Raman spectra

Several Raman spectra of the Fo6% sample were measured in the pressure range from 1 bar to 167 kbar in a Diamond Anvil Cell. Raman spectra of FO6% in the low-frequency ($100\text{-}700\text{ cm}^{-1}$) and high-frequency range ($700\text{-}1100\text{ cm}^{-1}$) are plotted separately for detailed analysis (Figs. 31 and 32). In the high frequency region there are four distinct bands at 824 , 857 , 904 , and 957 cm^{-1} , (Fig. 31). The origin of these bands are discussed in detail in section 3.5. Two strong A_g bands at 824 and 857 cm^{-1} are assigned to the stretching of Si-O₂ and Si-O₃ bonds, respectively. The medium band (A_g mode) at 957 cm^{-1} originates from Si-O₁ bond. The weak band at 904 cm^{-1} is a B_{3g} mode.

The systematic frequency increase of these bands indicate the compressibility of the SiO₄ tetrahedra (Fig. 33). Previous experimental work (Hazen, 1976; Hazen and Finger, 1980, Besson, et al., 1982) up to 50 kbar showed no significant change in the Si-O bond lengths. Spectroscopic studies of the metasilicate glasses indicates that silicon tetrahedra is preserved to very high-pressure above 35 GPa, (Hemley and Kubicki, 1991). In the Fo6% sample Raman bands appear at 824 cm^{-1} and 857 cm^{-1} at 1 bar, show differential frequency shift with increasing pressure (Table 11). The band at 857 cm^{-1} has a slope of $0.398\text{ cm}^{-1}/\text{kbar}$ compared to $0.304\text{ cm}^{-1}/\text{kbar}$ for the 824 cm^{-1} band. All the Raman bands, except 824 cm^{-1} , of Fo6% composition has higher values of slope than corresponding bands of forsterite crystal. This implies that higher deformation of the unit cell under pressure for the Ca-containing olivines. All Raman

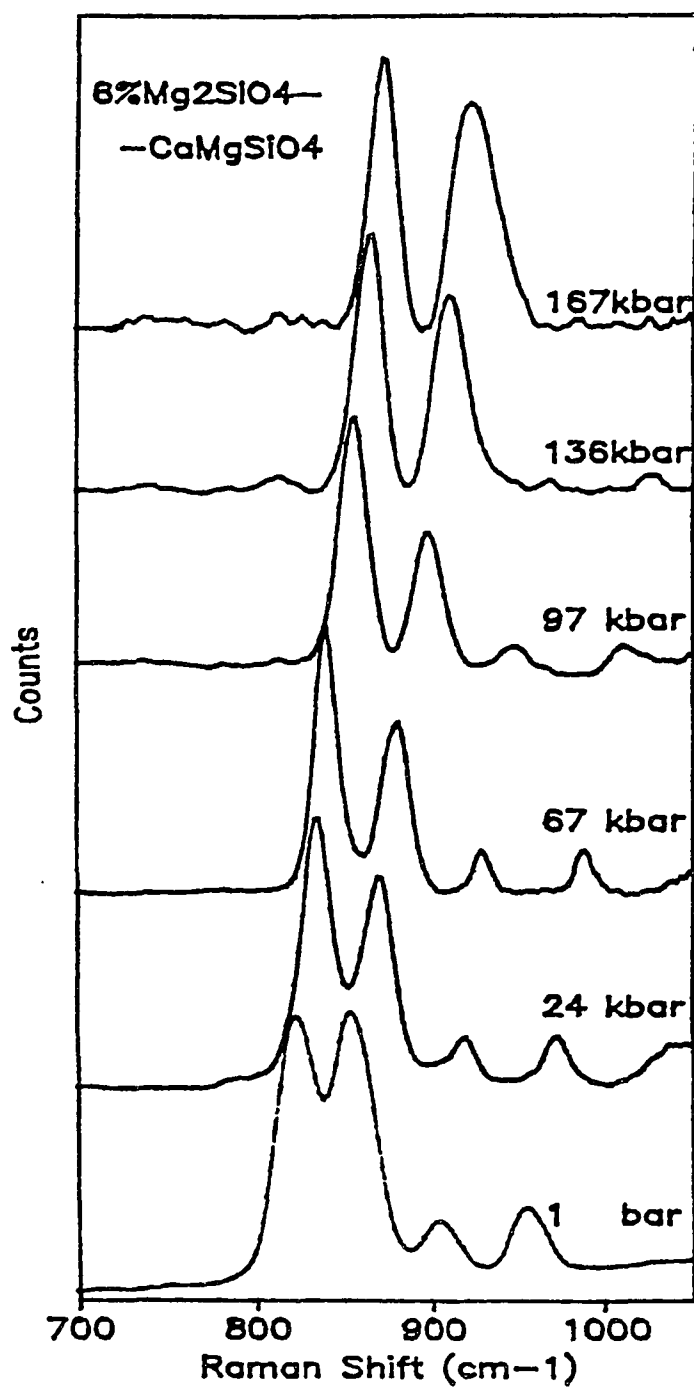


Figure 31: High-pressure Raman spectra of Fo6% in the high frequency region (700-1100 cm⁻¹) between 1 bar and 167 kbar.

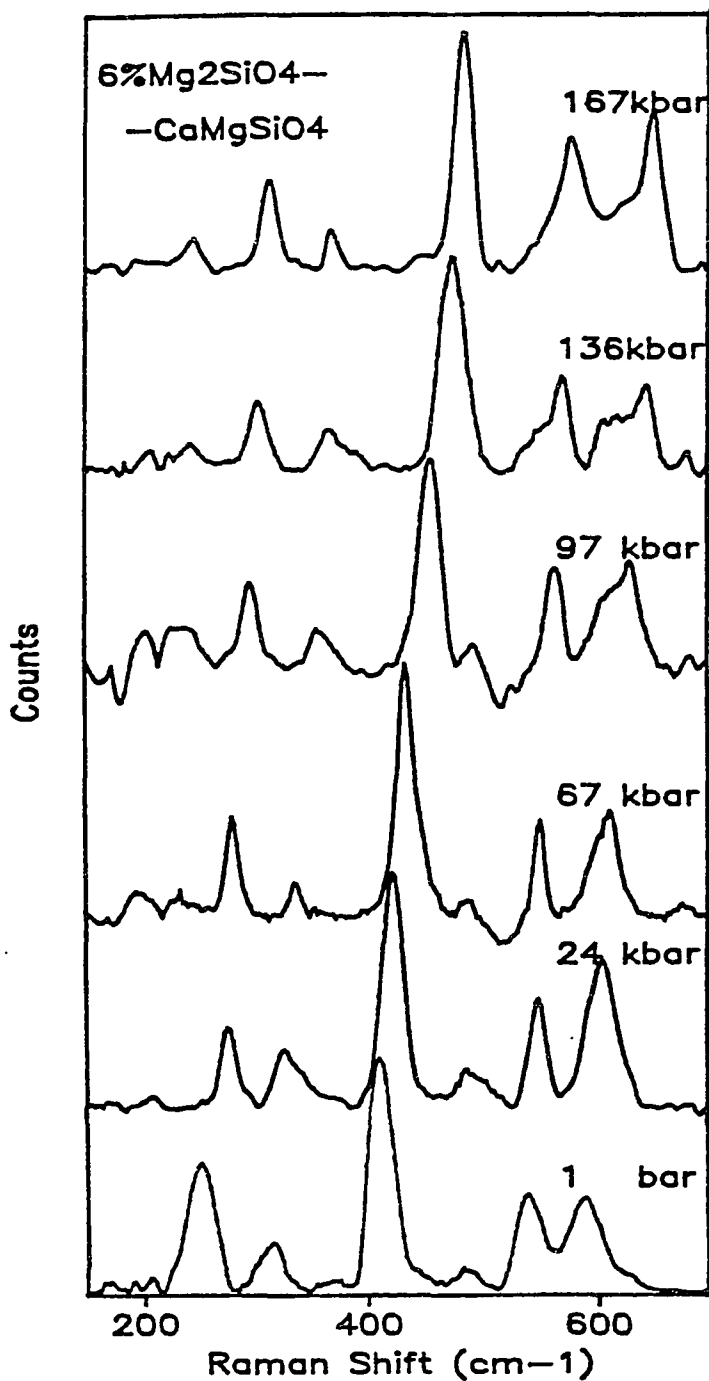


Figure 32: High-pressure Raman bands of Fo6% in the low-frequency region (100-700 cm⁻¹).

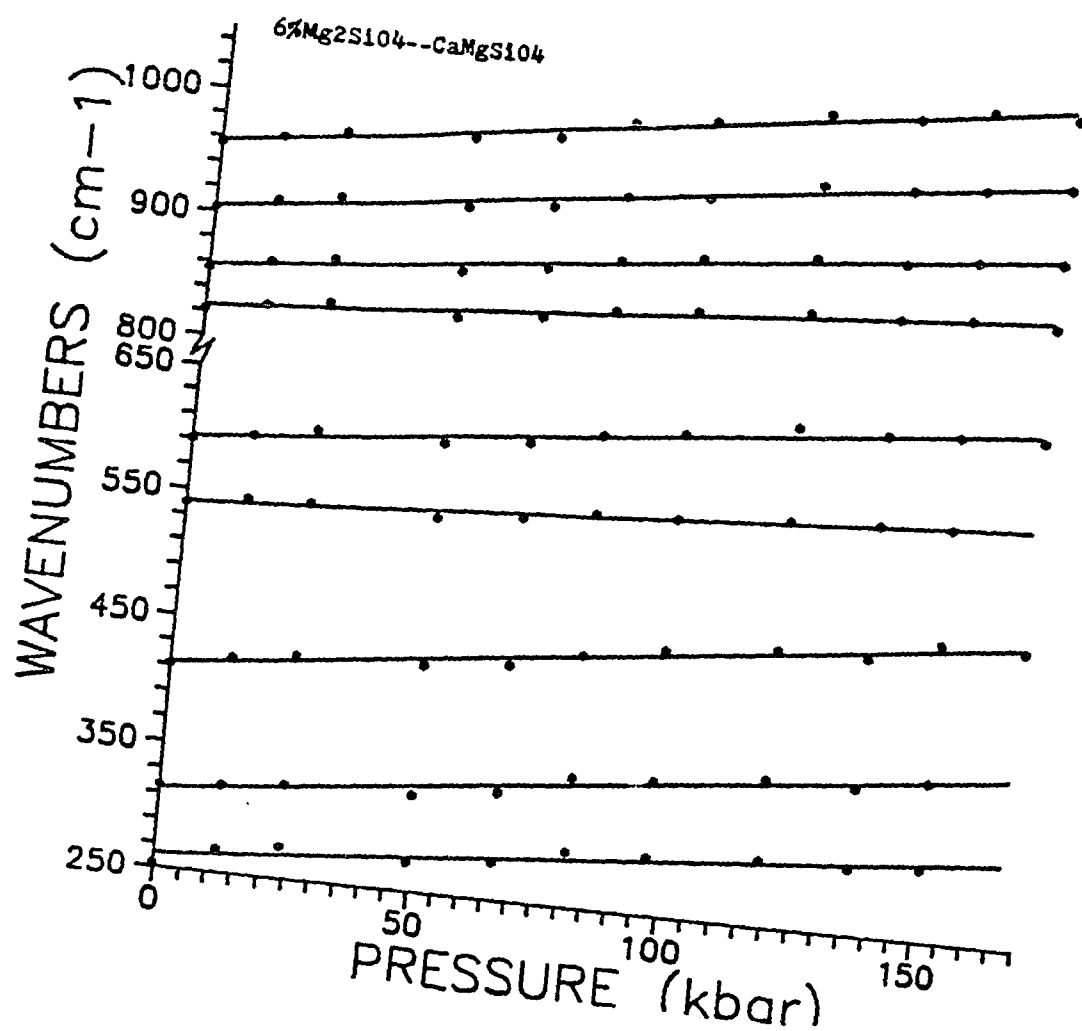


Figure 33: Plot of the variation of Raman frequency with pressure.

Table 11. Equation resulted from the least square fit to the nine observed Raman (A) and six IR (B) bands (cm^{-1}) in Fo6% (CaMgSiO_4) with pressure (kbar).

78

$$\begin{aligned}v_1 &= 956.8 + 0.521 \times P \\v_2 &= 904.0 + 0.472 \times P \\v_3 &= 857.3 + 0.398 \times P \\v_4 &= 824.4 + 0.304 \times P \\v_5 &= 591.8 + 0.392 \times P \\v_6 &= 539.8 + 0.246 \times P \\v_7 &= 412.1 + 0.452 \times P \\v_8 &= 313.9 + 0.414 \times P \\v_9 &= 261.5 + 0.336 \times P\end{aligned}\quad (\text{A})$$

$$\begin{aligned}v_1 &= 1005.0 + 0.204 \times P \\v_2 &= 897.5 + 0.274 \times P \\v_3 &= 830.2 + 0.270 \times P \\v_4 &= 590.1 + 0.312 \times P \\v_5 &= 554.1 + 0.200 \times P \\v_6 &= 533.0 + 0.163 \times P\end{aligned}\quad (\text{B})$$

bands show decrease in intensities and with increasing pressure. This is attributed to the distortion of the SiO_4 tetrahedra with pressure (Kubicki, et al., 1992). Also, it could be because of the thinning of the sample in the DAC (Hofmeister, et al., 1989). Finally, after each pressure increment the DAC has to be aligned with the laser beam for maximum signal. In some cases DAC is completely removed from the stage for measuring the ruby fluorescence using another spectrometer. This procedure makes it very difficult for one to comparatively study the intensity of the vibrational band.

The band width analysis of the three high-frequency bands, 824, 857, and 904 cm^{-1} , and one low-frequency band, 412 cm^{-1} , have been carried out. These calculations show non-linear behavior of band widths with pressure. This could be because of several reasons. Decrease in the band width is an indication of reduced disorder in the crystal structure. Band width of a vibrational band is a function of positional disorder (White, 1972). At high pressure the positional disorder in the crystal structure decreases. With DAC, it is very difficult to obtain Raman spectra with good signal to noise ratio. In the attempt to obtain a good Raman signal minor adjustments on the slit width of the spectrometer or on other optical alignments on the DAC has to be made, which in turn affect the intensity and band width calculations.

In the low-frequency region, 100-700 cm^{-1} , six distinctive bands are observable. General observation of these bands show systematic frequency increase of the bands toward high wave numbers, decrease in band intensity, increase in band width, and band merging with increasing pressure. For example, the strongest band 412 cm^{-1} , at ambient conditions, show systematic frequency shift towards high-frequency with increasing pressure. This band has a maximum shift of 74 cm^{-1} , and a slope of 0.452 $\text{cm}^{-1}/\text{kbar}$. Table 10a lists the equation containing the coefficients of the linear fit for all the major bands. There are no break in the slope between pressure 67 kbar and 97 kbar as seen in earlier experiments in forsterite composition (Wang, et al., 1992).

The full width at half maxima of the low-frequency band shows non-linear trend in its behavior and is attributed to experimental discrepancies. Also, when analyzing the high pressure spectra, curve fitting in the low frequency region becomes quite a difficult task because of the weak intensity of bands in the region and as well as the background that results from the scattering of light from the diamond anvil cell.

3.7.2. Infrared spectra

Mid-infrared spectra of the Fo6% sample in the pressure range 1 bar to 194.1 kbar, are given in Fig. 34. A linear fit relating six IR frequency with pressure are given in Fig. 35. Mid-IR frequencies in olivine originate from the stretching of Si-O-Si bonds. Clearly, all bands show increase in frequency with pressure. Pressure derivatives of these bands are given in Table 12. IR bands have lower pressure derivatives than that of Raman bands. The lower values of the pressure derivatives suggest the resistance to compression of the SiO_4 tetrahedra. Wang, et al., (1992) have calculated the Gruneisen parameter for the forsterite using both Raman and IR vibrational data. They suggested that all the modes with low Gruneisen values (<0.9) are associated with the internal modes and those above 0.9 are of lattice modes resulting from the cation interactions. For the calculations of Gruneisen parameters of the Fo6% sample, the bulk modules, K, were not able to find in the literature. Therefore, the K (Bulk modules) value corresponding to monticellite (CaMgSiO_4) composition is used to calculate approximately the Grunesien parameter for Fo6% (Kuskov and Galimzyanov, 1984). Grunesien parameter γ_i can be calculated using the following formula:

$$\gamma_i = (K_{T0}/\nu_{i0}) * (\partial \nu_i / \partial P)_{T0}.$$

Table 12 lists the observed modes and their assignments, pressure derivatives, and the Gruenesien parameters. As mentioned earlier, the Gruenesien parameters for the IR modes are lower than the Raman modes.

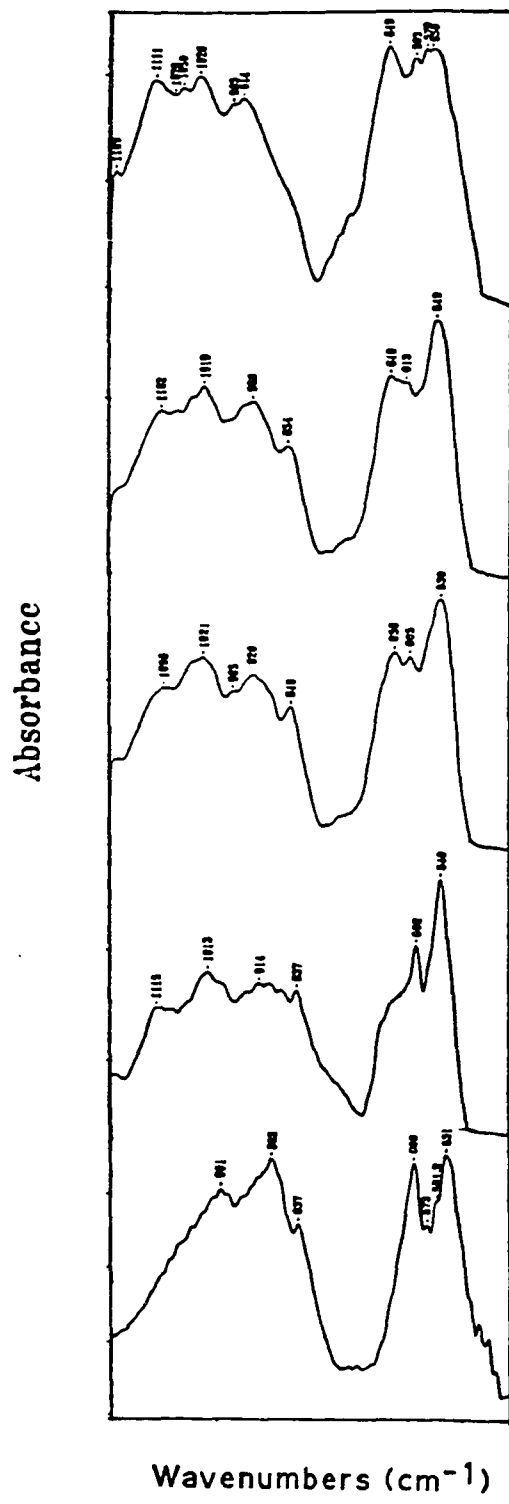


Figure 34: Five IR spectra of Fo6%, between pressure 1 bar and 197 kbar, in the 450-1200 cm^{-1} region.

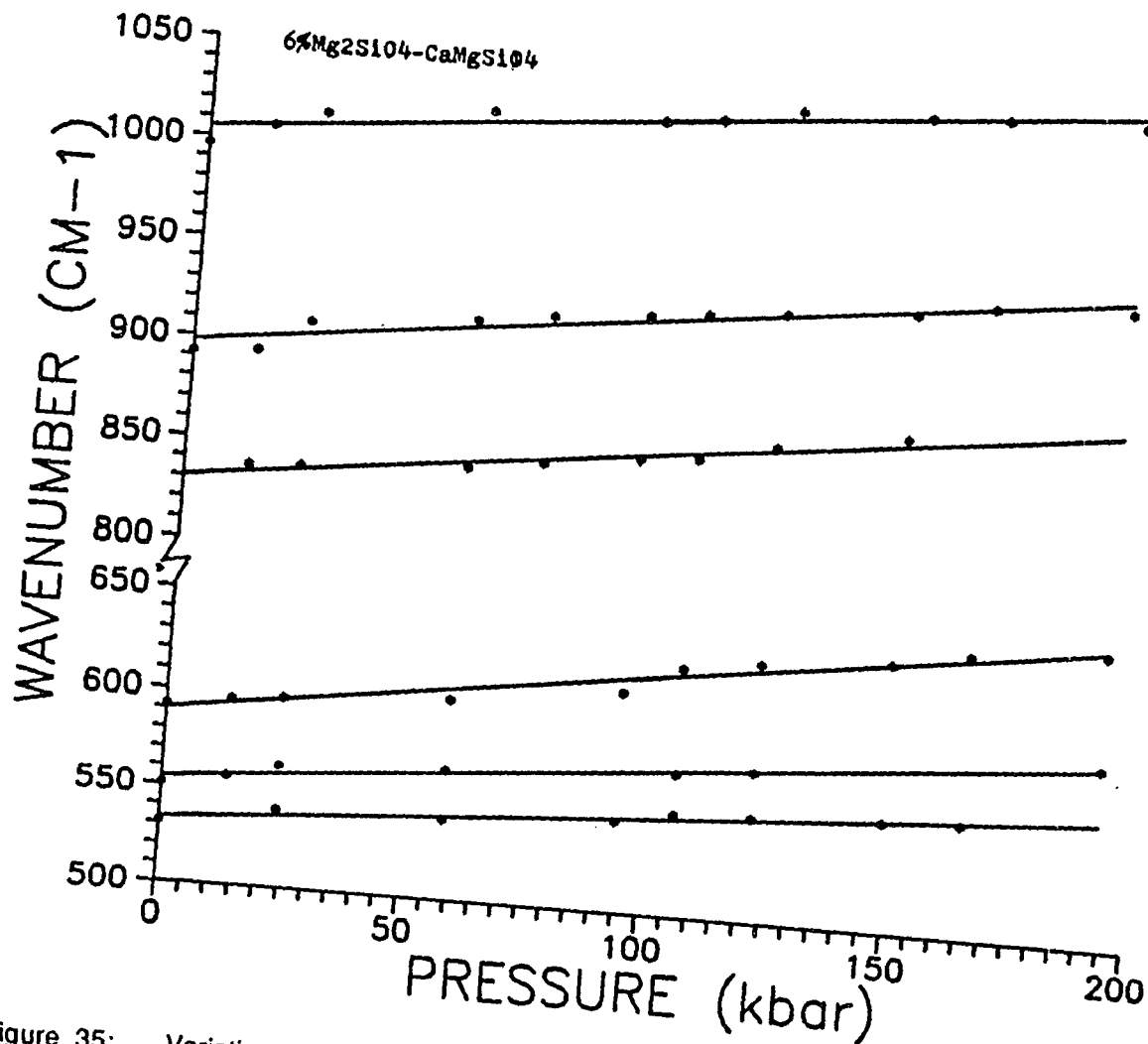


Figure 35: Variation of IR frequency with pressure. Like Raman bands, IR frequency varies linearly.

Table 12: Pressure derivatives and mode assignments for the Raman vibrational modes of forsterite, fayalite, and Fo6% forsterite.

Fayalite			Forsterite			Monticellite		
ν_{i0}	$d\nu_i/dp$	mode	ν_{i0}	$d\nu_i/dp$		mode	ν_{i0}	$d\nu_i/dp$
183	.301	T(SiO ₄)	241	.280	ve	261	.336	
227	.116	T(SiO ₄)						
224	.235	R(SiO ₄)						
306	.389	T(Mg ₂ O ₆)						
331	.295	T(Mg ₂ O ₆)						
341	.498	R(SiO ₄)						
376	.369	R(SiO ₄)						
411	.312	R(SiO ₄)+v2						
424	.480	R(SiO ₄)+v2						
434	.458	R(SiO ₄)+v2						
441	.545	R(SiO ₄)+v2						
454	.194	v4				n4	540	.452
585	.289	v4				v4	592	.246
609	.324	v4						
826	.307	v3				v1	824	.304
856	.324	v1				v3	857	.398
884	.303	v3				v3	904	.472
922	.283	v3						
966	.501	v3				v3	957	.521

IR bands show increase in the band width with increasing pressure. Unlike Raman, IR bands are very weak and they overlap with the nearby bands. This makes curve fitting calculation very difficult. However, the effect of broadening with pressure is very significant and attributed to the deformation of the SiO_4 tetrahedra at high pressure.

3.8

Low-temperature Raman spectral studies.

Thermal oscillation of an atom resulting in anharmonic vibration, causes the mean position to be displaced, and leads to thermal expansion. The anharmonicity decreases with temperature and at very low temperatures, in some crystals ~50 K, it nearly vanishes. It also affect the thermodynamic properties of a mineral such as thermal conductivity and Gruneisen parameter (Anderson, 1989). Study of crystal structure at very low-temperature therefore, allows one to detect the anharmonicity present in various vibrational modes. Several authors have discussed the theoretical aspects as well as experimental results of anharmonic behavior on various crystal structures (Pathak, 1965; Opie, 1968; Lowndes, 1971; and Sharma, 1992).

From the forsterite-monticellite solid solution series, Fo6% sample has been chosen for the low temperature work, since it is close to 100% monticellite (CaMgSiO_4) composition. Anharmonicity of forsterite along with other olivines has been studied by Sharma, et al., 1992.

3.9 Experimental setup

Micro-Raman set up is utilized to conduct low-temperature experiments and is described in detail in chapter 2. From a Spectra Physics Laser Model #2020, 488 nm laser line has been used as the excitation source. Approximately 12 mw power is used at the sample ensuring there is no local laser heating of the sample. After every temperature increment or decrement, approximately 20 to 30 minutes is allowed for equilibrium conditions. Temperature controller operate it best below 150 K and above this temperature it shows fluctuation as much as +/-10 K.

3.10 Results and discussion

Raman spectra of Fo6% sample has been obtained between temperatures 290 K and 32 K in the frequency range 120-720 cm⁻¹ and are shown in Figs. 36 and 37. As one expects, Raman frequency increases with decreasing temperature. Strong bands at 241 cm⁻¹, and 293 K, are assigned to the B_{2g} mode and move up to 262 cm⁻¹ with decreasing temperature (35 K). The most intense band ~390 cm⁻¹, at room temperature, is assigned to the B_{3g} mode (Choples, 1990). This band shifts to higher frequency by approximately 20 wave numbers. A plot of the Raman frequency with temperature reveals that the frequency drops sharply from room temperature to 175 K, and then levels off around 125 K (Fig. 38). This indicates that the modes are becoming harmonic below 125 K. The present result agrees with Sharma, et al., (1991) suggestion that forsterite, Nickel olivine and tephrite become harmonic below 175 K. They found that iron containing olivine, fayalite, becomes harmonic only below 50 K.

Band width of an observed band in a vibrational spectrum is an indicator of disorder in the crystal structure of minerals (Farmer, 1974). In turn, disorder is a function of composition, pressure, and temperature. Study of band width with composition in the Fo-Mo solid solution series at room temperature reveals that there is only a small amount of positional disorder in the Ca-rich end of the solid solution series. This is indicated by the fact that in the Fo-end of the Fo-Mo solid solution series band width verses composition plot shows steep slope, while at the Mo-end, slope is very gentle. This clearly indicates that Mg and Ca are ordered in the M1 and M2 sites (see section 3.3b) in the Mo-end. Further evidence of this result can be derived from the low-temperature experiments on Fo6%. For example, the band at 390 cm⁻¹ of Fo6% show decrease of band width with temperature. Its band width decreases from 38.27 cm⁻¹ to 15 cm⁻¹ between 293 K and 35 K (Fig. 39). However, the major change in the band width occurs between 293 K and 175 K. Below 175 K, the band width change is

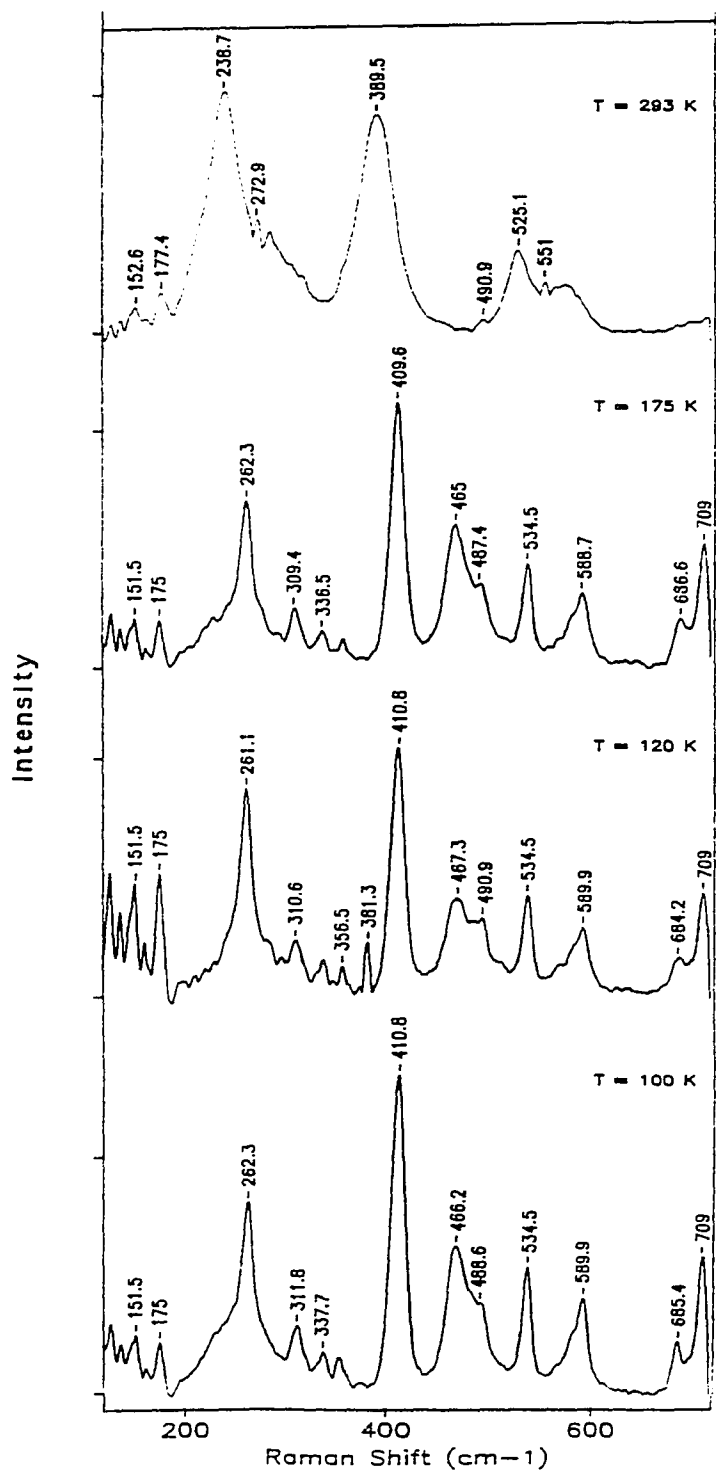


Figure 36: Low-temperature (293-100 K) Raman spectra of Fo6% in the 100-700 cm^{-1} region.

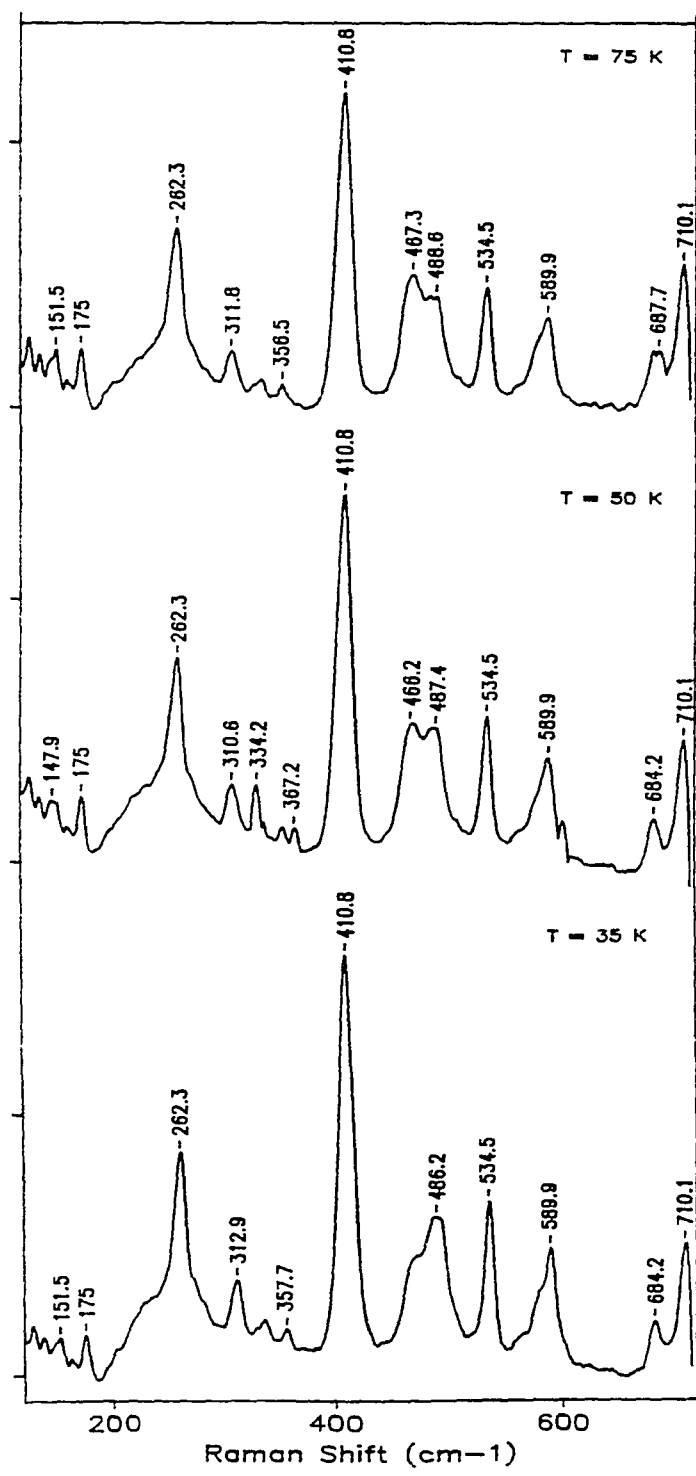


Figure 37: Low-temperature (75-35 K) Raman spectra of Fo6% in the $100\text{-}700 \text{ cm}^{-1}$ region.

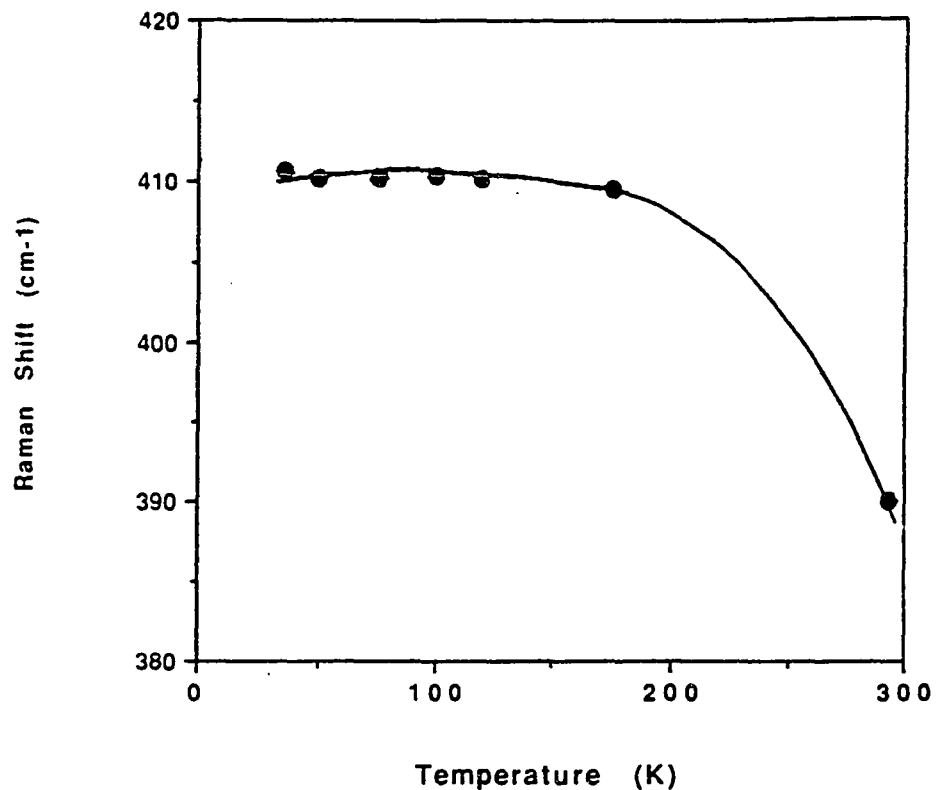


Figure 38: Variation of Raman frequency with temperature. Raman band around 390 cm^{-1} decreases the frequency sharply the temperature up to 175 K then levels off up to 35 K.

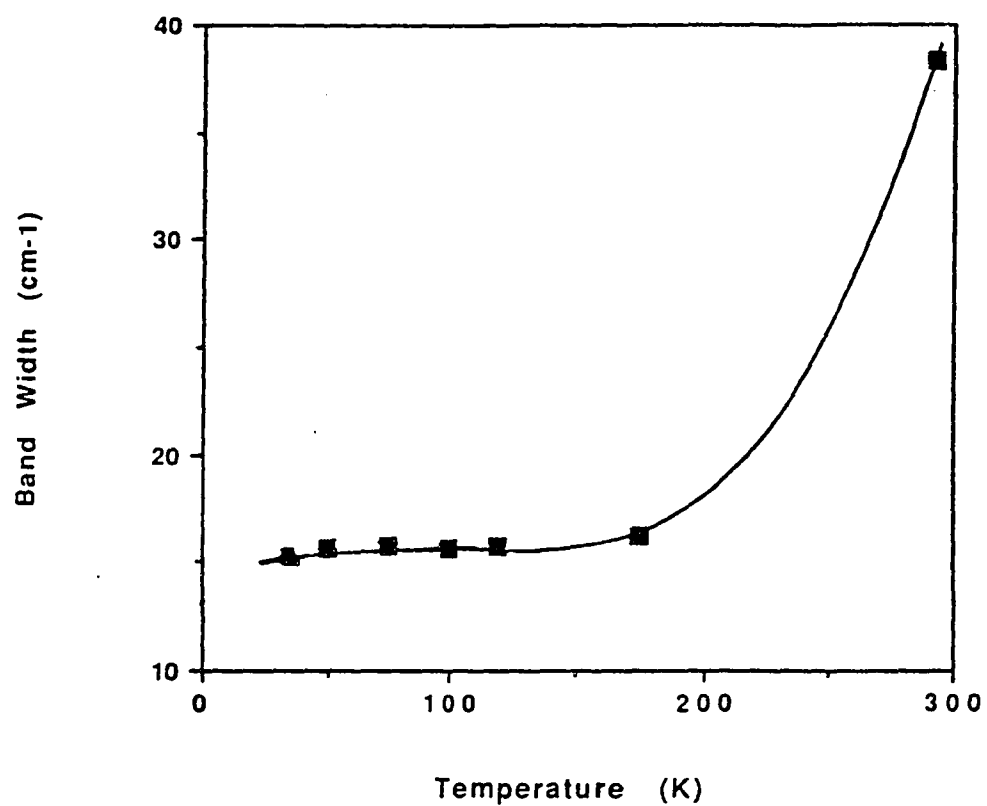


Figure 39: Variation of Band width of the 390 cm^{-1} peak. The band width at room temperature is much higher than at low temperature indicating the order in the crystal structure.

only less than 2 wave numbers. If there are positional disorder below 175 K frequency and the band width should change. Therefore, the absence of change of band width indicates very small amount of disorder. Thus, Raman spectroscopy of minerals at low-temperature gives information on the anharmonicity and disorder in minerals.

CHAPTER 4

RAMAN STUDIES OF PYROXENES

To earth scientists, knowledge of the structure of minerals at high temperature is very important. Study of minerals at elevated temperatures leads to better understanding of the physical phenomena such as crystallization, solid solutions, and inter growth in crystals. Pyroxenes play a major role in the dynamics of the lower and upper mantle. It is predicted that pyroxenes and garnets are the main constituents of the shallow mantle. On the basis of seismic data it has been suggested that perovskite is a major phase in the lower mantle. Experimental studies have shown that $MgSiO_3$ transforms into perovskite in the lower mantle under high pressures. Also, pyroxenes are an important mineral group found in meteorites and on the lunar surface (Anderson, 1989). Therefore, the study of pyroxenes is very important for the study of the earth as well as for other planets.

Pyroxenes belong to the inosilicate group in which the SiO_4 tetrahedra link to form an infinite chain by sharing oxygens (Fig. 40). Therefore, two of the four oxygens in each SiO_4 tetrahedron are shared and as a result the ratio of silicon to oxygen becomes $(Si:O) = 1:3$. The mean Si-O (=T-O) bond length ranges from 1.618 Å to 1.644 Å. In pyroxene crystal structure, the shortest of among the four Si-O bond distances the shortest is usually Si-O₂ and the longest is Si-O₃ (bridging oxygen) except for calcium tschermaks (CATS). Cameron and Papike (1981) found that the mean Si-O bond length increases slightly with increasing radius of the cation. Most pyroxenes belong to the monoclinic form, but, the orthorhombic form also exists. Each unit cell of a single chain has a length of approximately 5.2 Å. Pyroxenes crystallize at very high temperatures, but if water is present in the melt, pyroxenes may react with water to form amphibole (Klein and Hurlbut, 1977).

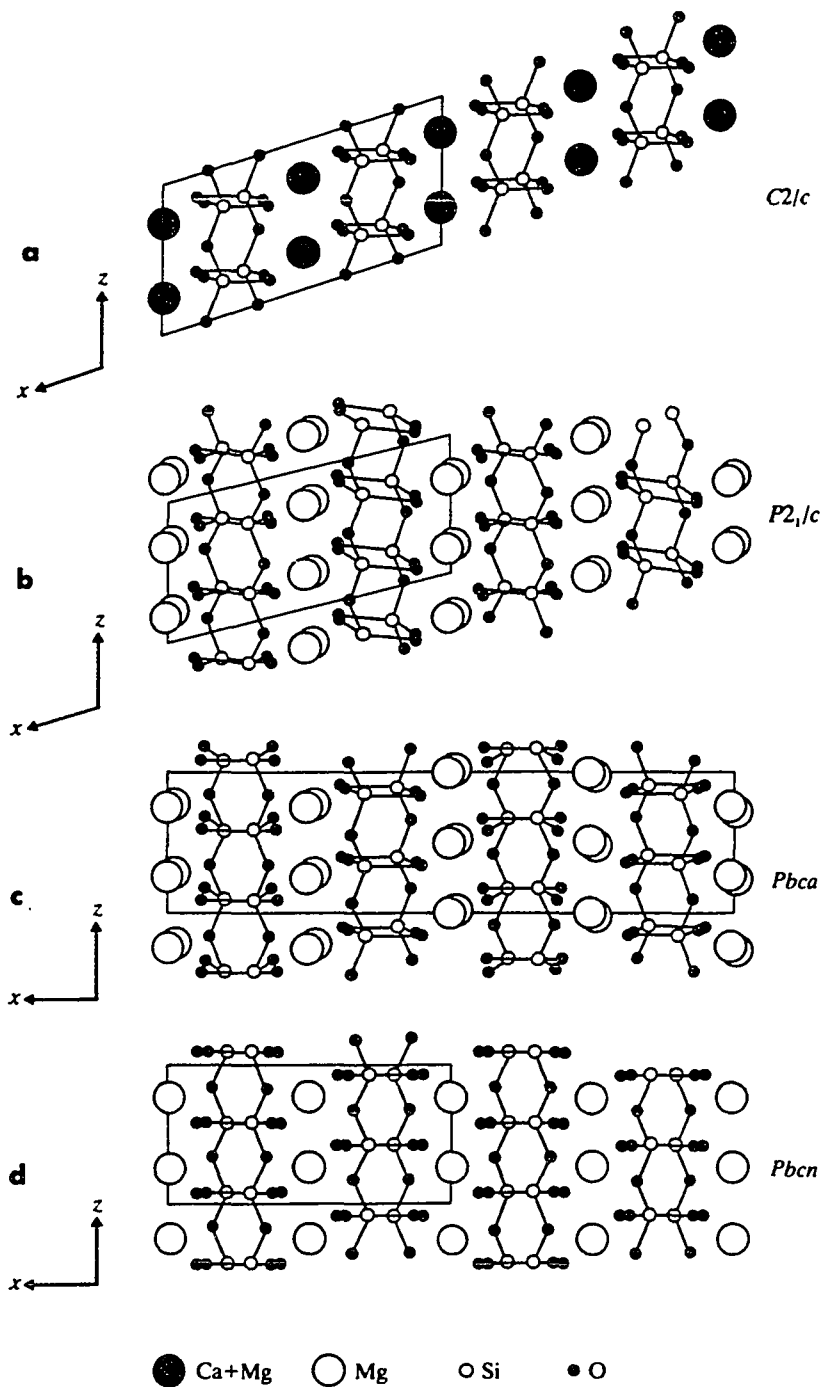


Figure 40: Schematic diagram of four pyroxene crystal structures belonging to four different space groups (after Deer, et al., 1978).

The chemical composition of pyroxenes can be written as XYZ_2O_6 . Here X = Na^+ , Ca^{2+} , Mn^{2+} , Fe^{2+} , Mg^{2+} and Li^+ in the M2 crystallographic site, Y = Mn^{2+} , Fe^{2+} , Mg^{2+} , Fe^{3+} , Al^{3+} , Cr^{3+} and Ti^{4+} in the M1 crystallographic site, and Z = Si^{4+} or Al^{3+} in the tetrahedral chain. The M1 cation is coordinated by four O1 and two O2 anions that have fairly regular octahedral configuration (Fig. 41). The coordination of M2 varies from six to eight depending on the cation size (Prewitt, 1980) and the crystal structure becomes more irregular.

The crystal structure of pyroxenes was first determined using X-ray diffraction by Warren and Bragg in 1928. Since, then several authors have refined the pyroxene structure (Brown, 1972; Smyth and Burnharu, 1972; Smyth, 1971; Appleman and Papke, 1969; Christensen and Hazell, 1967; and Cameron, et al., 1973). Refined and more detailed knowledge of crystal structure has been always useful for more accurate studies of phase transitions, exsolutions, and solid solutions. Knowledge of the structural properties of these minerals at high-pressure and temperatures is very valuable to earth scientists, but experimental data on this subject is very rare. However, Smyth (1973) has determined the structure of ferro-hypersthene up to 8500 C. Cameron, et al., (1973) have investigated high-temperature properties of six pyroxenes using the X-ray diffraction method and tabulated the structural parameters. They suggested that, compared to the mean M-O distances, the Si-O bond lengths do not vary much and there is differential expansion with increasing temperature between Si-O and M-O bonds. The differential expansion affects the silicate chain structure and the structural transformation of minerals.

Vibrational spectroscopy has not been used extensively in the study of structural properties of pyroxenes as is the case with orthosilicates. However, infrared spectra of pyroxenes have been reported by several authors (Lazarev, 1972., Ruatstein and White, 1971, and Kieffer, 1979), thereby establishing a data set across different

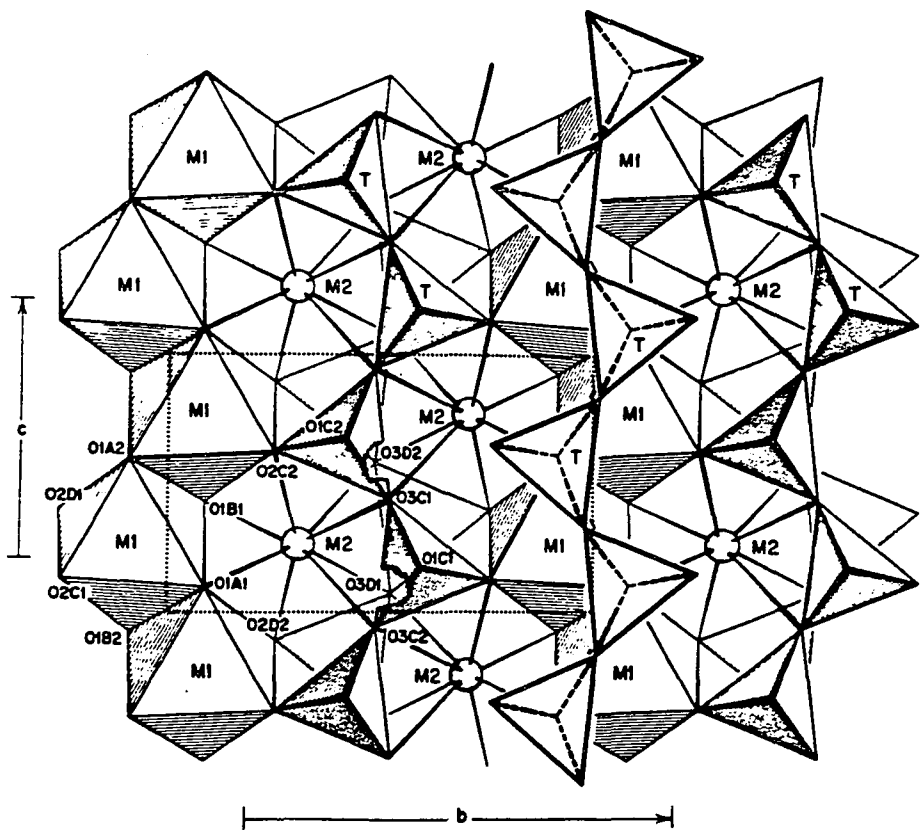


Figure 41: Crystal structure of C₂/c pyroxene projected on to the (110) plane (after Cameron and Papike, 1981).

compositional ranges. This data set was mainly used for mineral phase identification. IR spectroscopy is a good tool for identifying mineral components of different phases. Raman spectra of pyroxenes were first reported by White (1975). Kieffer (1979) has used this data along with the infrared vibrational data to obtain thermodynamic parameters such as heat capacity and entropy. Etchepare (1972) used Raman spectroscopy to study the structure of crystalline and glassy diopside. Tomisaka and Ishi (1980) have discussed the lattice dynamic properties of diopside in detail. Sharma and Simons (1981) have investigated different polymorphs of crystalline spodumene.

In the present work, the author first investigates the Raman spectra of six pyroxenes at room temperature. Their vibrational band assignments, variation in the band intensity with cation substitution, and their implications on the bond characteristics are discussed. Then, the high temperature properties of diopside and α -spodumene up to 700° C are also presented. Finally, the Raman spectra of ortho-, proto, and clino-enstatite have been measured and an attempt is made to interpret the high temperature vibrational data by deconvoluting the complex bands into various components.

4.1 Experimental setup

The Raman spectra of the six pyroxene samples were measured using a micro-Raman setup and Spex double monochromator conventional Raman setup. A diode array detector cooled at -30° C was used to collect the Raman signal in conjunction with the micro-Raman setup. For the double monochromator, a thermo-electrically cooled photomultiplier tube was used. Approximately 20 mW laser power was used at the sample. All the pyroxene samples were small single crystals, and none of the samples were subjected to polarized orientated single crystal studies because of their small sizes.

High temperature data was collected using the high temperature furnace as shown in chapter 2.

4.2 Theoretical calculations

All of the pyroxenes used for the analysis belong to the monoclinic space group C2/c with Z=4. There are two formula units per unit cell. For example, diopside is a common monoclinic mineral, and has 20 atoms in the unit cell and belongs to C2/c space group. Tomisaka and Iishi (1980) have theoretically calculated the number of vibrational modes present in the diopside crystal and compared that with the experimentally observed bands. Theoretically 57 (3N-3) optic modes were expected, and the distribution of these modes among different symmetry species is given below.

$$\Gamma_{\text{total}} = 14 A_g(R) + 16 B_g(R) + 13 A_u(IR) + 14 B_u(IR).$$

where R and IR represents Raman and infrared modes, respectively. Experimentally, 50 vibrational modes have been observed .

4.3 Results and discussion

Raman spectra of six pyroxene crystals, acmite ($\text{NaFe}^{3+}\text{Si}_2\text{O}_6$), diopside ($\text{CaMgSi}_2\text{O}_6$), hedenbergite ($\text{CaFe}^{2+}\text{Si}_2\text{O}_6$), calcium tschermaks ($\text{CaAl(Al)}\text{SiO}_6$), jadeite ($\text{NaAlSi}_2\text{O}_6$), and α -spodumene ($\text{LiAlSi}_2\text{O}_6$) were measured at room temperature and are shown in Figs. 42 and 43. General observation of these spectra reveal that the main features of all the spectra are somewhat similar. The spectral region between $100\text{-}1100 \text{ cm}^{-1}$ can be divided into two parts: 1) the low-frequency region ranging from $100\text{-}500 \text{ cm}^{-1}$. 2) the high-frequency region ranging $500\text{-}1100 \text{ cm}^{-1}$. The low-frequency vibrations are the deformation and bending modes, and

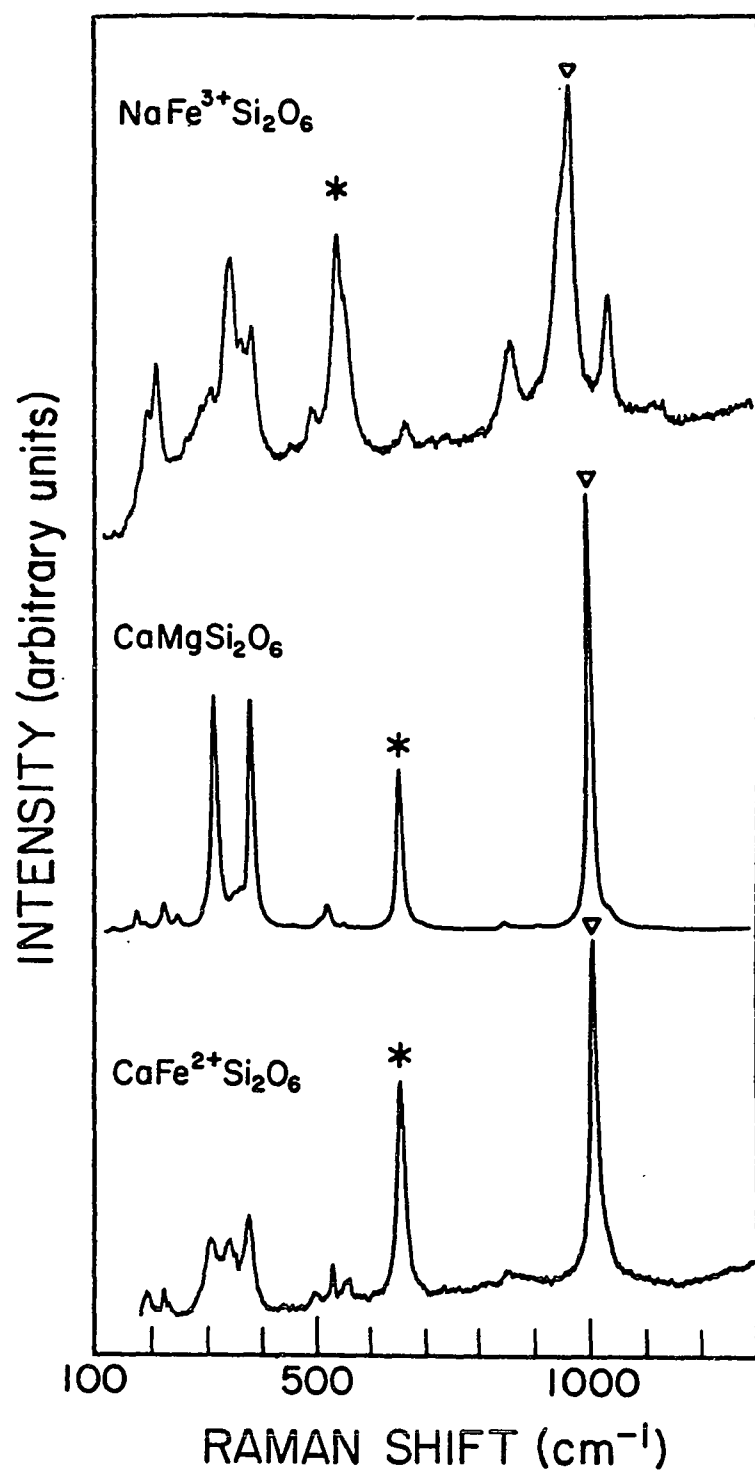


Figure 42: Raman spectra of acmite, diopside, and hedenbergite at ambient conditions.

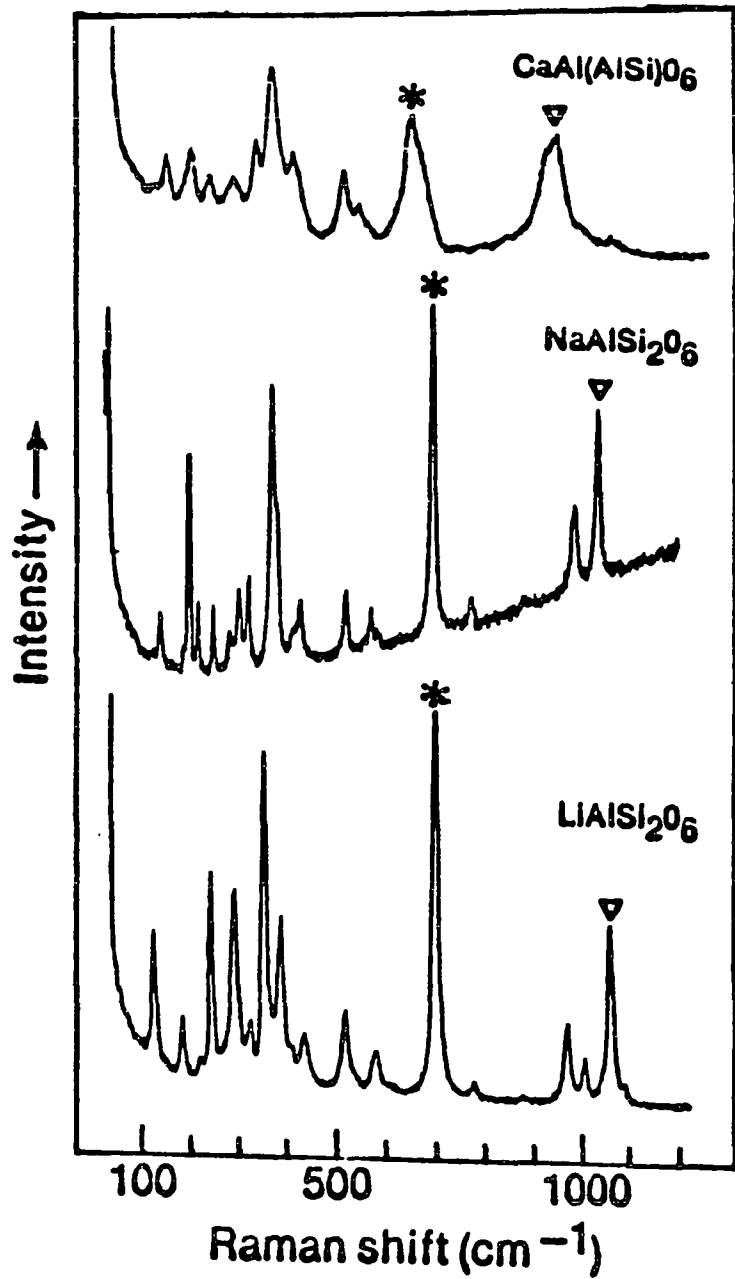


Figure 43: Raman spectra of CaTs, Jadeite, and spodumene crystal at ambient conditions.

the high-frequency vibrations are attributed to various stretching movements of the Si-O bonds. For example, the strong band around 700 cm^{-1} is the characteristic feature of the pyroxene chains. White (1974) has assigned this band to the symmetric stretching of bridging oxygen, $\nu_s(\text{T-O-T})$, vibrations of T-O-T bonds in the chain. In diopside this band appears as a strong and narrow band at around $\sim 662\text{ cm}^{-1}$. In α -sodumene, jadeite, and calcium teshmaks, however, the corresponding $\nu_s(\text{T-O-T})$ band appears at 707, 699 and 651 cm^{-1} respectively. Variation in the frequency is attributed to the substitution of different cations in the octahedral sites. For example, between α -spodumene and jadeite, the Raman frequency of α -spodumene is higher than in jedite. In α -spodumene the Li^+ cation that goes into the M2 crystallographic site is much smaller in size than that of Na^+ in jadeite. Now, the coulomb interactions between the cation in the M2 crystallographic site and the non-bridging oxygen in the tetrahedra is a function of the cation size. A plot of M1-O (\AA) verses cation radius in the M1 crystallographic site shows a linear relation between cation radius and M1-O bond length. Smaller cations will have a lesser attraction on oxygens, and therefore, weaker pull on the oxygen atom. This in turn makes the Si-O bond length shorter. Vibrational frequency depends strongly on the bond length of the vibrating atoms. Clark et al., (1969) has suggested that in C2/c pyroxenes the Si-O(br) bond lengths is a function of M2-O bonds.

The high-frequency band $\sim 1009\text{ cm}^{-1}$ in diopside is assigned to the stretching of (non-bridging oxygen) Si-O⁻ bonds. Compared to diopside and jadeite, acamite has more than one single strong peak in the high-frequency region. Jadeite, compared to diopside, acamite, and hedenbergite, has weak spectral features especially in the low-frequency region. In the spectrum of diopside the low-frequency bands are very clear and distinctive. These aspects of the spectral features are not as distinctive as in iron containing samples. This is because the absorption of the infalling radiation and

fluorescence due to the impurities present in the samples reduces or masks the Raman signals.

Figure 44 shows the ratio of Raman intensities of the symmetric stretch of the non-bridging oxygen band to the symmetric stretch of the bridging oxygen band versus the average bond length of the $\langle M-O \rangle$. In this plot, minerals containing aluminum - spodumene, jadeite, and CATs- have lower intensity ratios. They are plotted in the bottom part of the graph. The mineral containing magnesium, diopside ($CaMgSi_2O_6$), has higher intensity ratios and is thus plotted on the top right. Finally, the iron-containing samples are plotted in the middle and to the right of the graph. This behavior of the spectra can be explained in terms of the nature of the bonds. It has been shown that an ionic bond gives a stronger Raman signal than a covalent bond. Therefore, the aluminum-containing samples plotted on the bottom of the page have higher covalent character than the magnesium- or iron- containing samples. Thus, it is possible to use Raman spectroscopy to qualitatively determine the bond characteristics.

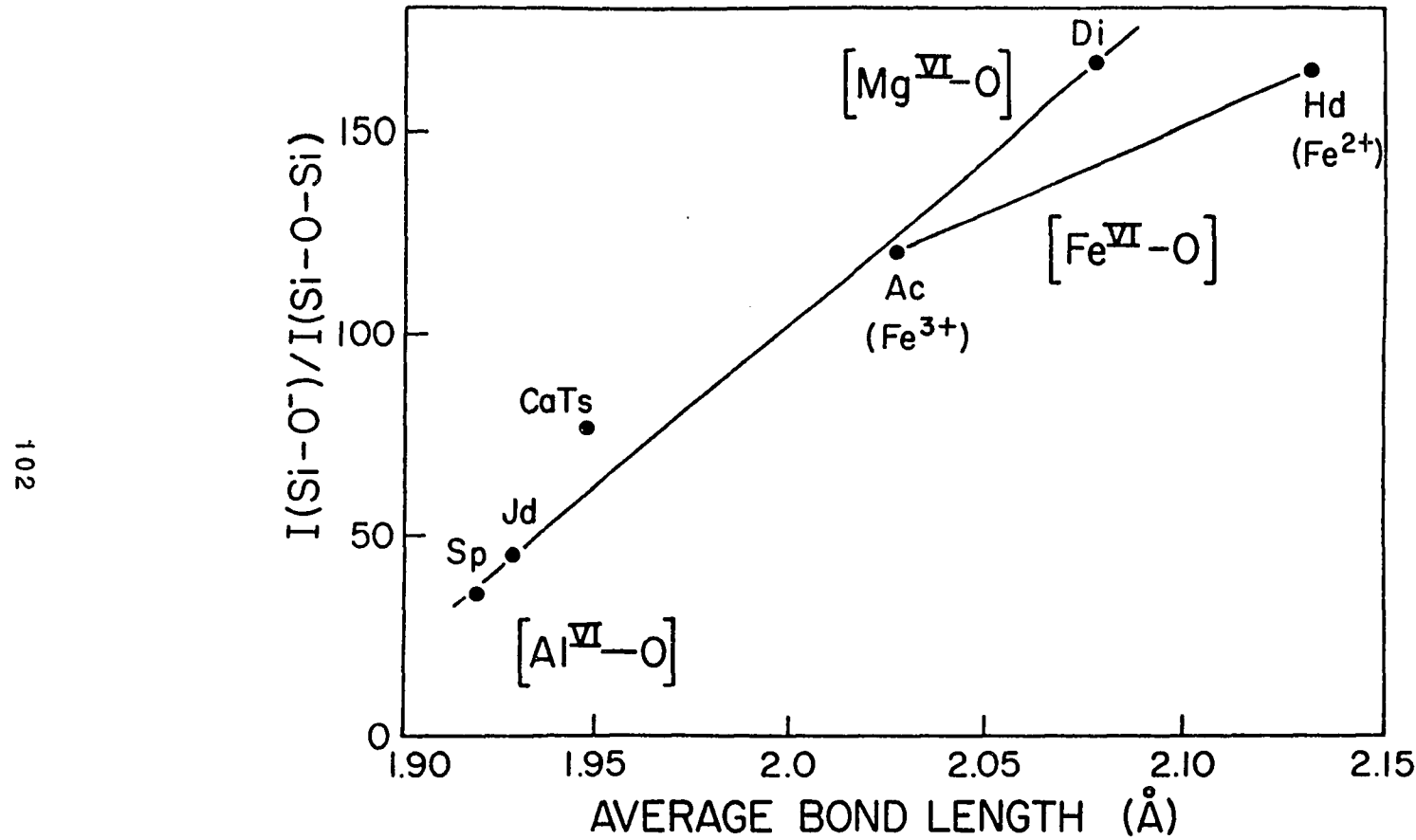


Figure 44. Plot of the ratio of symmetric (Si-O-) to symmetric (Si-O-Si) stretch vs Si-O bond length indicating the nature of the bond.

4.4

High temperature Raman spectra of diopside and α -spodumene.

In this section the author discusses the Raman spectra of diopside and α -spodumene at high temperature. As mentioned earlier, high temperature X-ray diffraction studies of these samples have been conducted by Cameron, et al., (1985). They found that the variation of silicon oxygen (Si-O) bond lengths are very small compared to the cation oxygen (M-O) bond lengths. The present study is targeted to verify these finding in pyroxene crystals as well as to investigate the properties of Raman spectra at high temperatures.

4.5 Results and discussion

The high-temperature Raman spectra of diopside between temperatures 298 K and 773 K are illustrated in Fig. 45. General characteristics of the spectra at various temperatures reveal a frequency shift toward lower wave numbers, an increase in band widths, and a decrease in relative intensity of the bands with increasing temperature. The decrease in intensity of the high-frequency bands with increasing temperature is attributed to the distortion of the silicate chain. Also, the intensity of the Raman bands has to be corrected before comparative study of the intensities, and this has not been taken into consideration in the present study. The increase in the width of these bands is caused by the increased anharmonicity in the crystal structure. A plot of the observed Raman frequency vs temperature is shown in Fig. 46. The high-frequency band at 1042 cm^{-1} shows the highest frequency decrease and therefore has the steepest slope. All other Raman bands show a similar trend in slope with the exception of a band at 663 cm^{-1} , which shows a much smaller change in the frequency at high temperatures. Etchepare (1972) has assigned a band close to 663 cm^{-1} to the deformation and chain

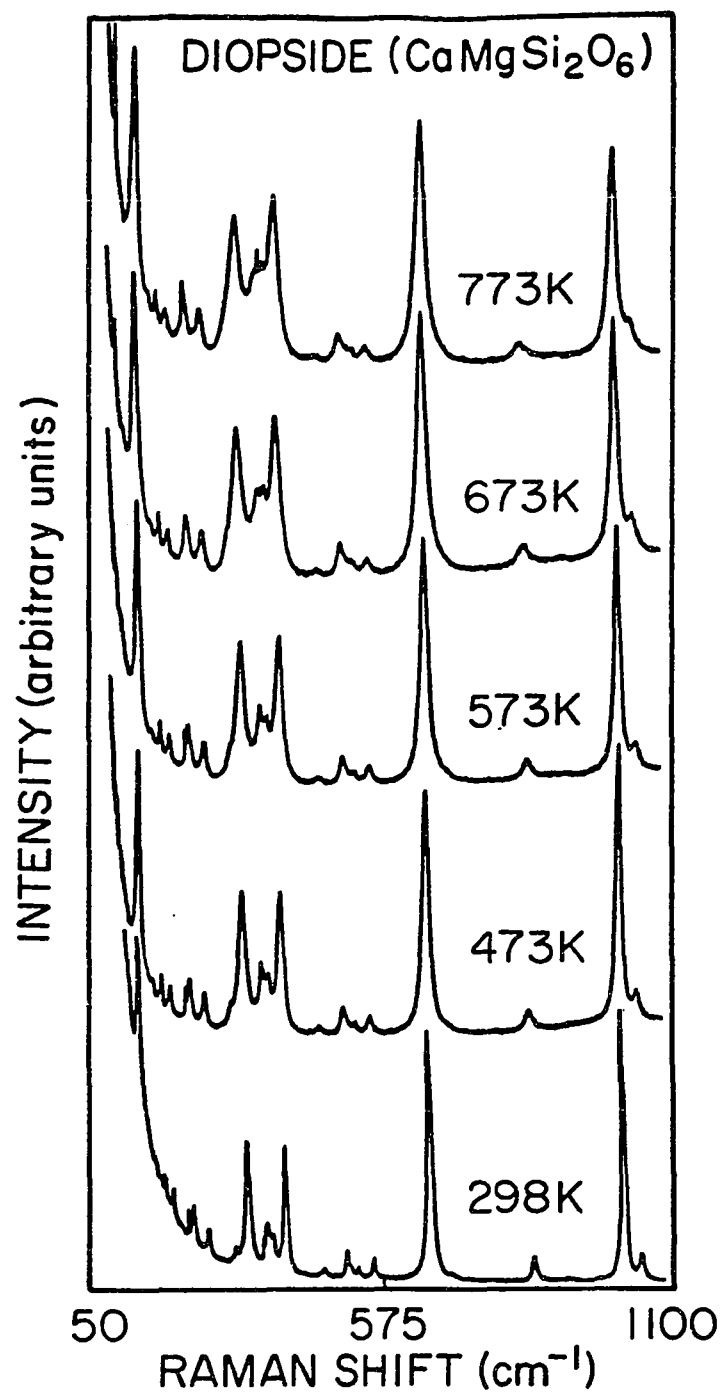


Figure 45: Raman spectra of diopside between 298 K and 773 K.

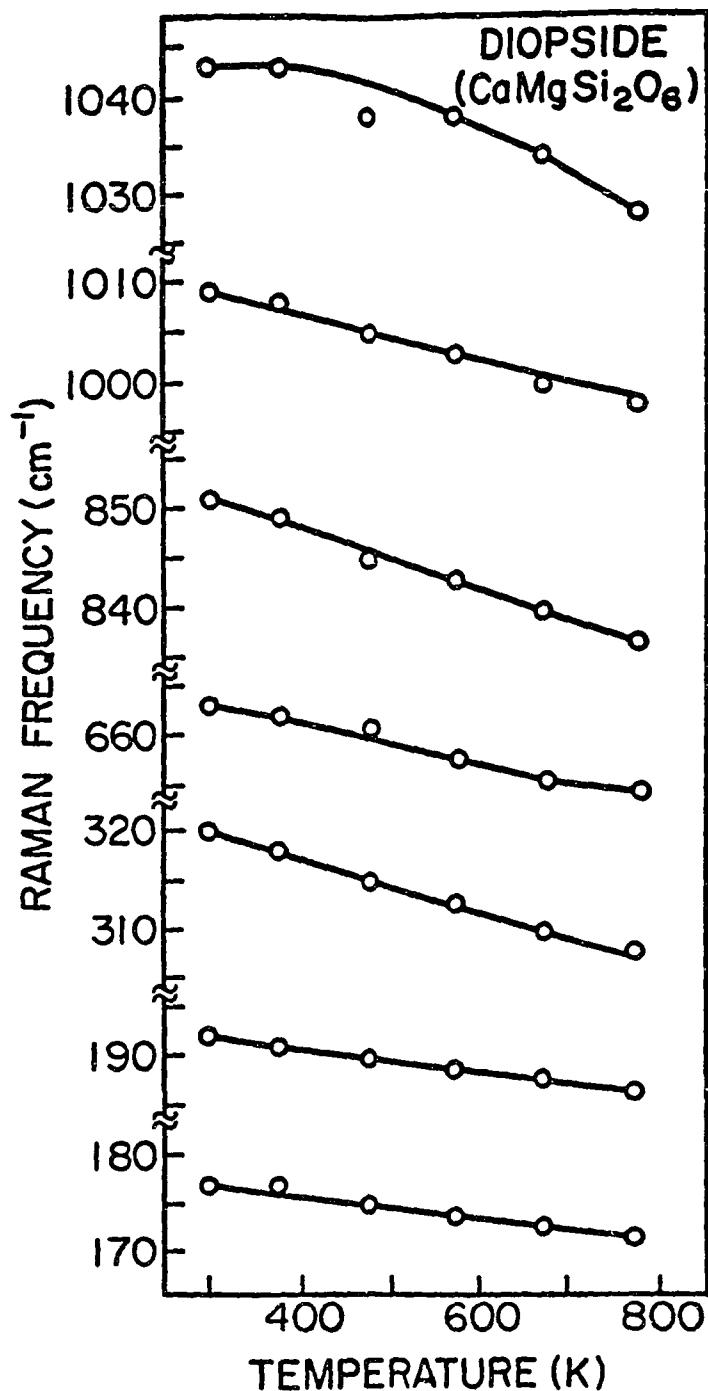


Figure 46: Variation of Raman frequency vs temperature. Most of the bands shows linear decrease in frequency with increase in temperature.

movements. The author, however, has not observed this in the present study which may be due to a combination of the change in the Si-O bond angles and Si-O-Si bond lengths.

Temperature vs observed Raman frequency of spodumene is shown in Fig. 47. Sharma and Simons (1981) have measured three polymorphs of crystalline and glassy spodumenes. High-frequency bands due to the stretching vibrations of Si-O-Si show a decrease in frequency with an increase in temperature. Since vibrational frequency of a band is inversely proportional to the bond length of the vibrating bond, one should except a decrease in Raman frequency with increasing temperature. However, Raman bands at 389 cm^{-1} , 182 cm^{-1} , and 123 cm^{-1} show an increase in the frequency above 500 K. Sharma and Simons (1981) have argued that the drastic changes in the Raman spectra of spodumene polymorphs are due to the presence of Al^{3+} ions both in the octahedral and tetrahedral sites. Three out of ten Raman bands of α -spodumene plotted against temperature show an increase in Raman frequency above 700 K. The X-ray diffraction studies of α -spodumene up to 760°C indicate that all of its structural parameters, such as Si-O bond, M1-O bond, and M2-O bond, show linear a increase with increasing temperature. This implies that Raman frequency should decrease with temperature. However, the observed Raman frequencies show a slight increase in frequency. It should be noted that the Raman frequency is extremely sensitive to the bond length. Any small changes in the bond length can be detected by monitoring the changes in the Raman frequency corresponding to that bond, which may not be sensitive when using X-ray diffraction techniques. For example, Adams and Sharma (1978) have studied the high pressure properties of sodium and potassium cyanide. Their results, which contradicted to the previously well established neutron and IR data, showed that there is an increase in the frequency of $\nu(\text{CN})$ due to a decrease in the $d(\text{C-N})$ bond length. Due to the limited resolution of the experimental techniques neither X-ray, nor neutron diffraction was able to detect the minute changes in the crystal structure. But, Raman spectroscopy

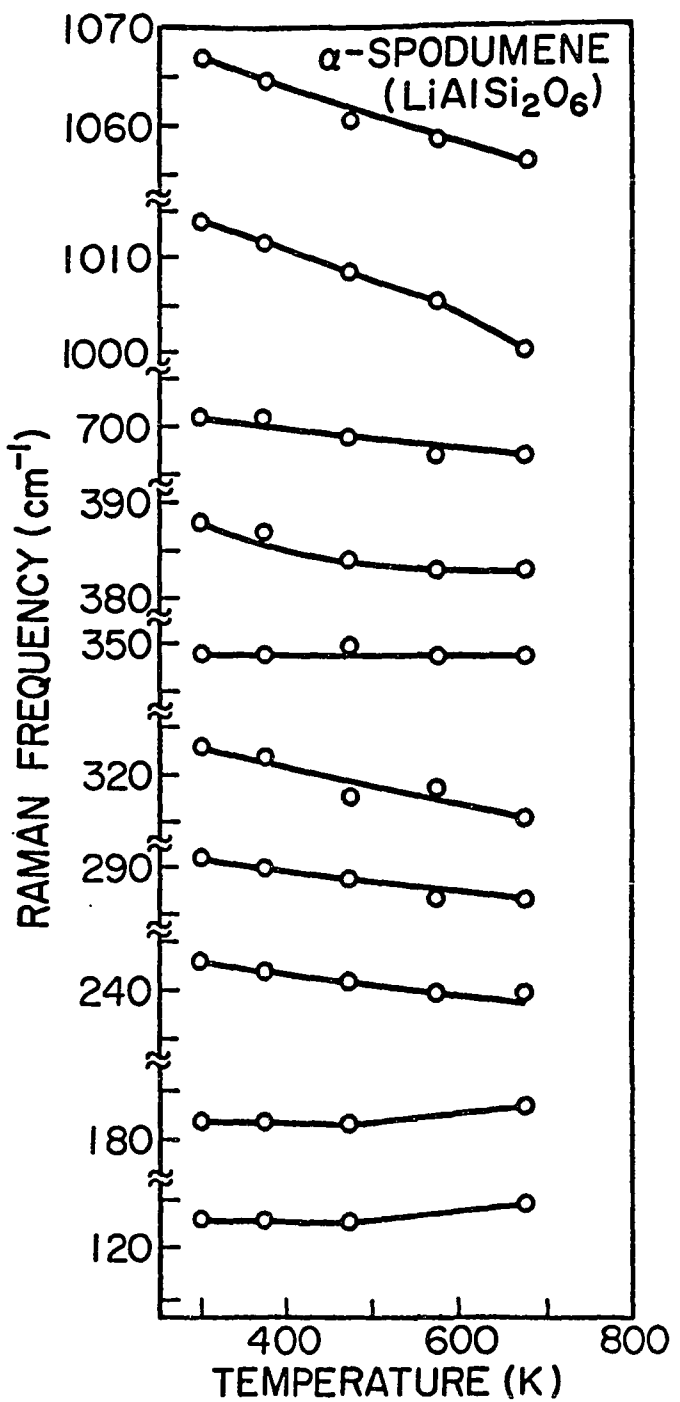


Figure 47: Variation of Raman frequency with temperature in α -spodumene.

were able to detect this small change. In α -spodumene, the increase in Raman frequency above 500 K is due to the small changes in crystal structure caused by the instability. It is known that at high temperatures above 500 K, α -spodumene becomes metastable, and therefore one should expect changes in the structural parameters. Thus, vibrational spectroscopy can be used to demonstrate and detect the instabilities in crystal structures.

4.6

High-temperature studies of enstatite.

The terminology enstatite represents a wide class of minerals which fall into different crystallographic groups (Smith, 1969., Prewitt, 1980). The most naturally occurring enstatite is the magnesium-iron-containing enstatite ($Mg_2Si_2O_6$ - $Fe_2Si_2O_6$). It is an orthorhombic mineral and belongs to the $Pcba$ space group. The pure form of $Fe_2Si_2O_6$ is a very rare mineral, because in most geological settings with equivalent pressure and temperature fayalite (Fe_2SiO_4) is the most favored mineral.

There are three principal polymorphs for the $MgSiO_3$: ortho-, clino-, and proto-enstatite. Ortho-enstatite is a stable phase below $1000^0 C$ and proto-enstatite is stable at high temperatures. Clino-enstatite is an intermediate monoclinic mineral that exists between ortho- and proto-enstatite and is a metastable phase at all temperatures. Proto-enstatite transforms into clino-enstatite upon quenching. Proto-enstatite crystals can, however, be formed in the presence of Li impurity (Cameron, et. al., 1973).

4.7 Results and discussion

The crystal structure of natural pyroxenes fall into two classes: orthorhombic and monoclinic. In Fig. 40 these two classes are illustrated. Diopside is monoclinic and is shown in Fig. 40a. In Fig. 40b, c, d crystal structures of three polymers of enstatite, low-clino, ortho- and proto-enstatite, are shown. Room temperature Raman spectra of ortho-enstatite, clino-enstatite, and proto-enstatite are given in Fig. 48. Even though the proto-enstatite spectra is noisy compared to ortho- and clino-enstatite, the basic spectral features of these pyroxenes in the high-frequency region remain the same. As

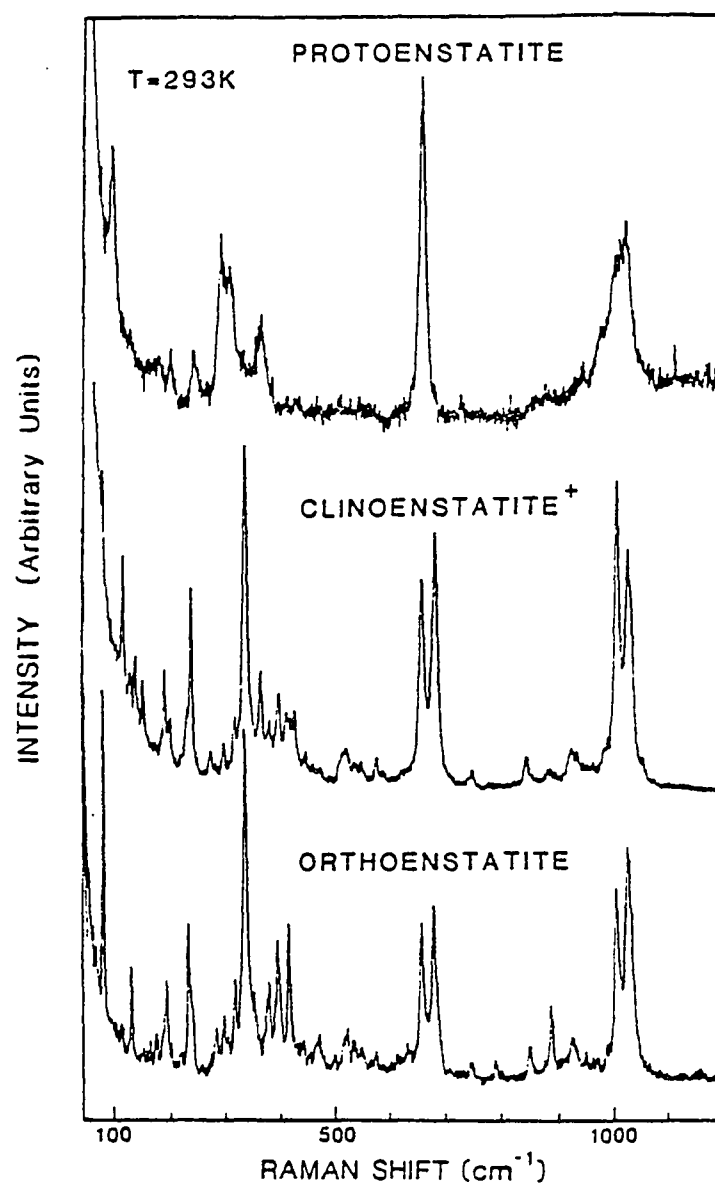


Figure 48: Raman spectra of proto-enstatite, clino-enstatite, and ortho-enstatite at 293 K.

while in proto-enstatite it appears as one single strong band. The intensities of individual bands depend on the orientations of the crystal. In the high-frequency region, $\sim 1000 \text{ cm}^{-1}$, two peaks appear in ortho-, and clino-enstatite, while the proto-enstatite gives only one single broad band. Upon heating, the proto enstatite transforms into proto-enstatite. The ortho-toproto enstatite transition take place at 1320 K. No Raman active soft modes (see Chapter 2) are observed at high temperatures in orthoenstatite. However, a new and strong band, 98 cm^{-1} , emerges at the ortho-toproto enstatite transition temperature (Fig. 49). Also, at the transition temperature several Raman modes show non-linear frequency variation indicating the structural transformation. The internal modes originating from the SiO_3 chain do not show much difference in their Raman spectra at high temperatures (Fig. 50). The major changes in the Raman spectra occur in the low-frequency region, where the vibrational modes are affected by the octahedral sites. Fig. 51 shows the variation of the Raman frequency with temperature. Smyth (1971) has suggested that the ortho-toproto enstatite transitions are triggered by the breaking of magnesium-oxygen bonds rather than silicon-oxygen bonds. Smyth's model is very much in agreement with presently observed Raman vibrational data.

The high temperature spectra of ortho-enstatite are shown in Fig. 52 and Fig. 53. The two high frequency bands at 1014 cm^{-1} and 1034 cm^{-1} originate from the non-bridging $\text{Si}-\text{O}^-$ symmetric stretch. However, as the temperature increases, these two bands shift at different rates and finally merge with each other. By resolving the bands into two it could be possible to understand more about the behavior of the SiO_3 chain. Therefore, curve-fitting of these bands was carried out using the Spectra Calc program. The bands were considered approximately 80-90% Lorentian and 20-10% Gaussian form. However, the shape of the band changes with temperature. Curve fitted results of the high-frequency bands are shown in Figs. 54 and Fig. 55. The Raman frequencies of

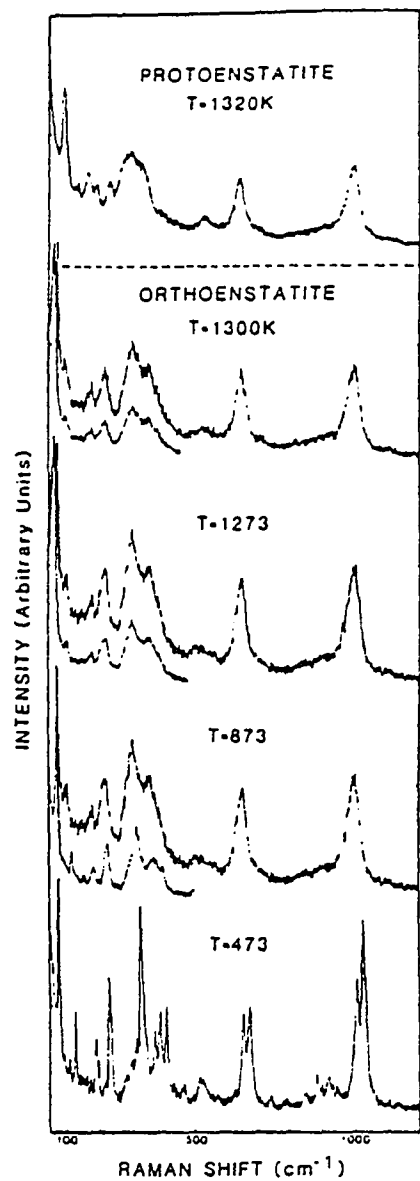


Figure 49: High-temperature Raman spectra of ortho-enstatite at high-temperature. The ortho-to-proto transition occurs at 1320 K marked by the appearance of a peak at 98 cm^{-1} .

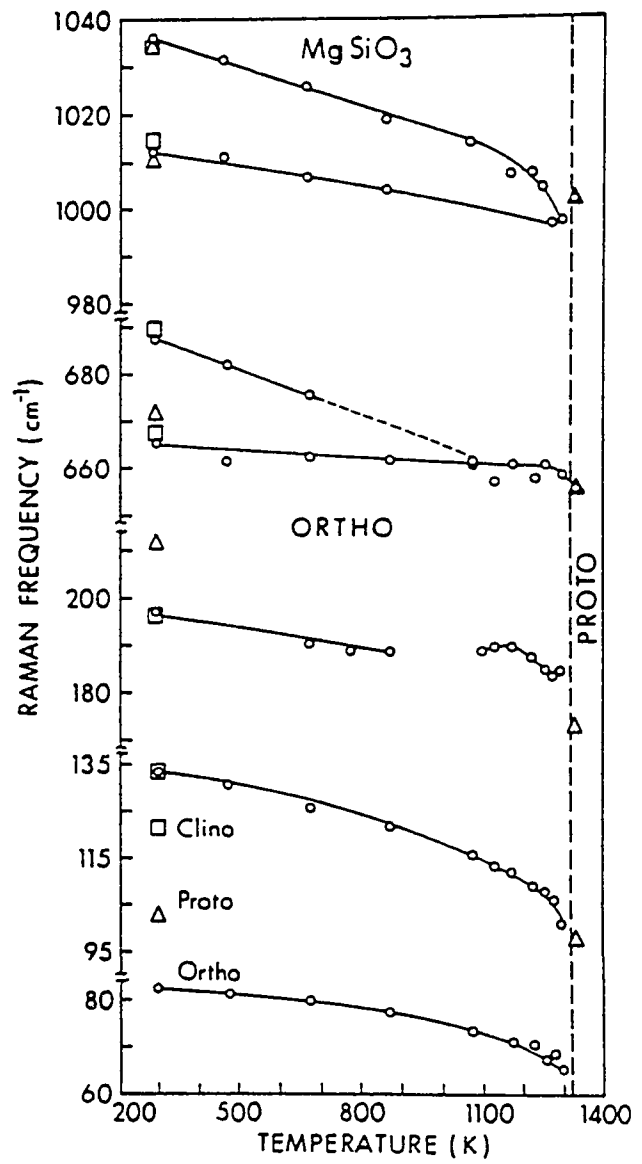


Figure 50: Plot of the variation of Raman frequency in ortho-enstatite with temperature.

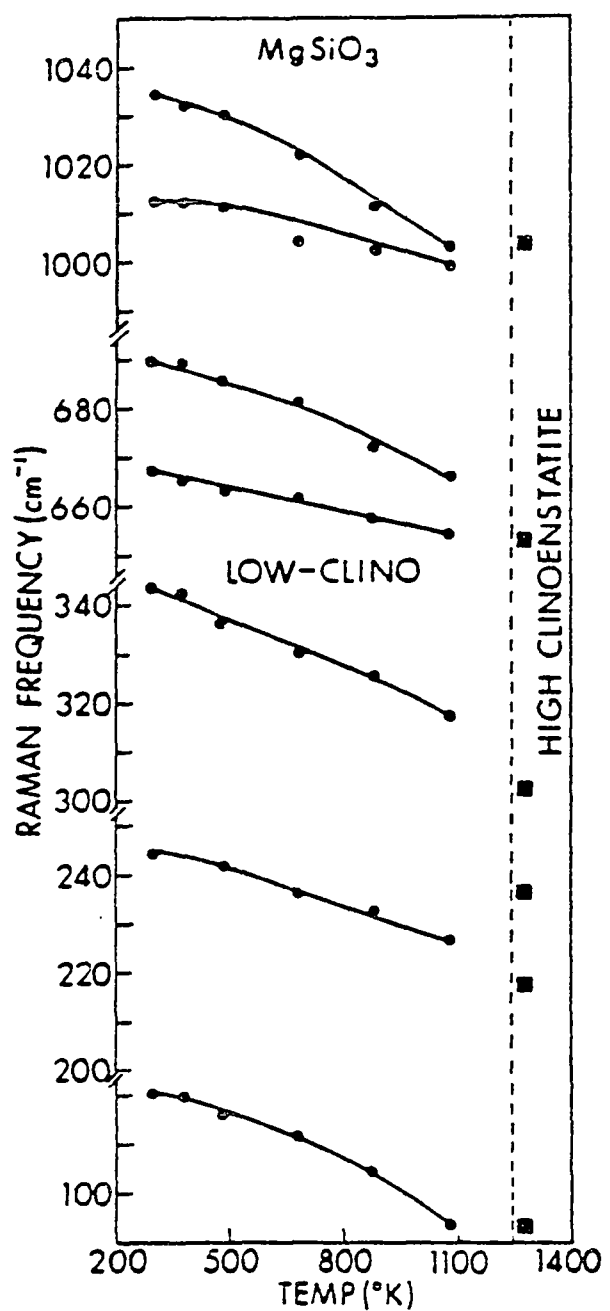


Figure 51: This plot indicates the transition of MgSiO_3 from the low-clino-enstatite to high-clino-enstatite.

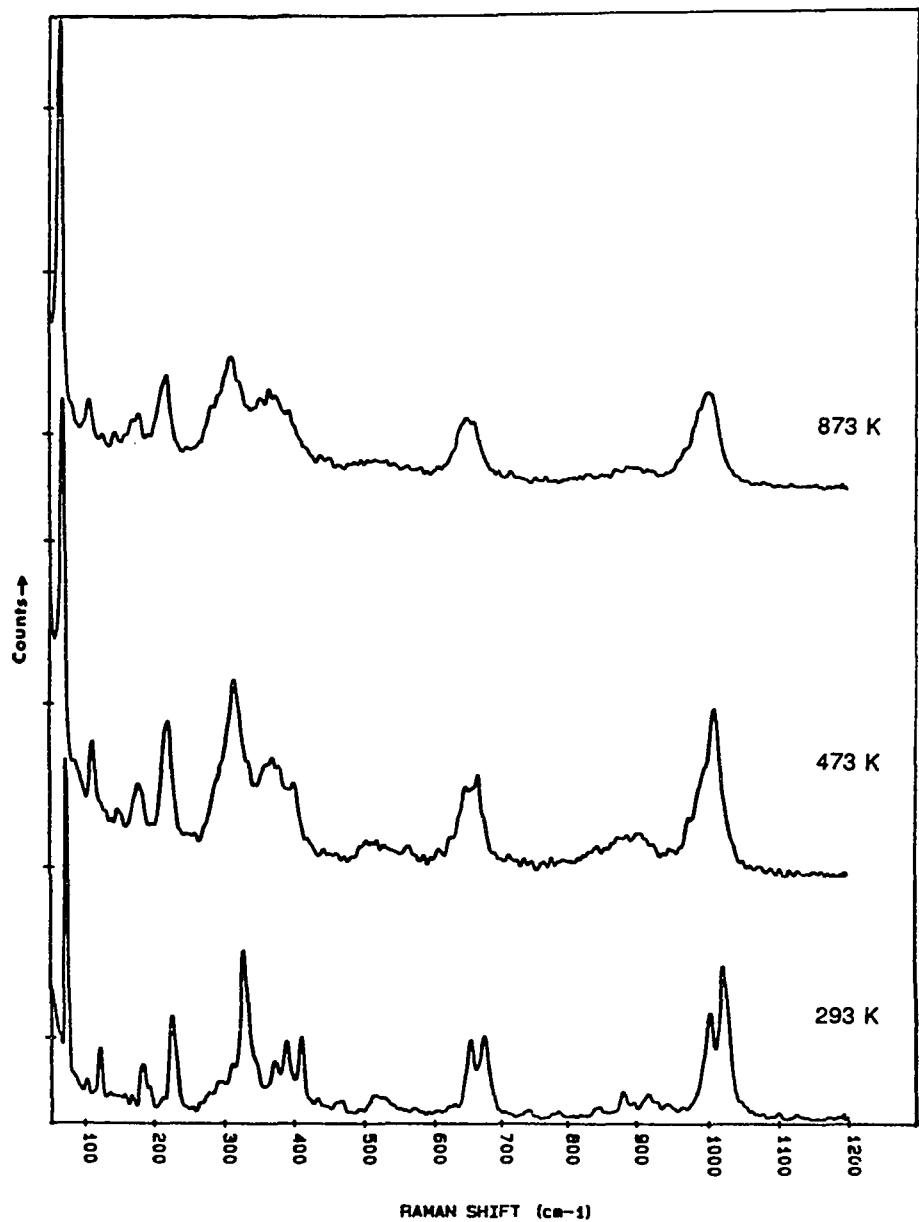


Figure 52. Raman spectra of ortho-enstatite between 293 K and 1273 K. Frequency shifts and band merging are observed in the 500-1100 cm^{-1} region.

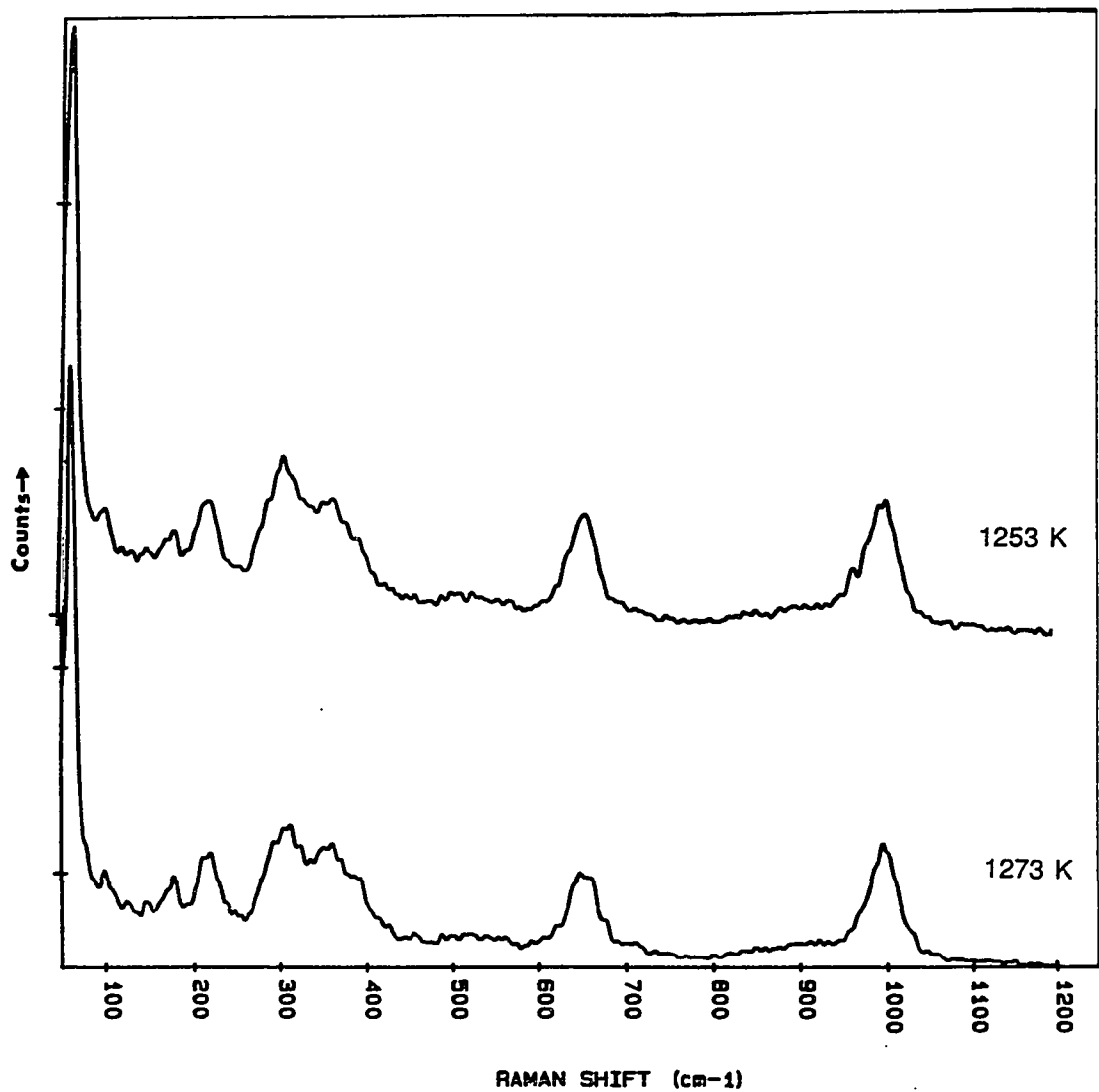


Figure 53. Raman spectra of ortho-enstatite between 293 K and 1273 K.

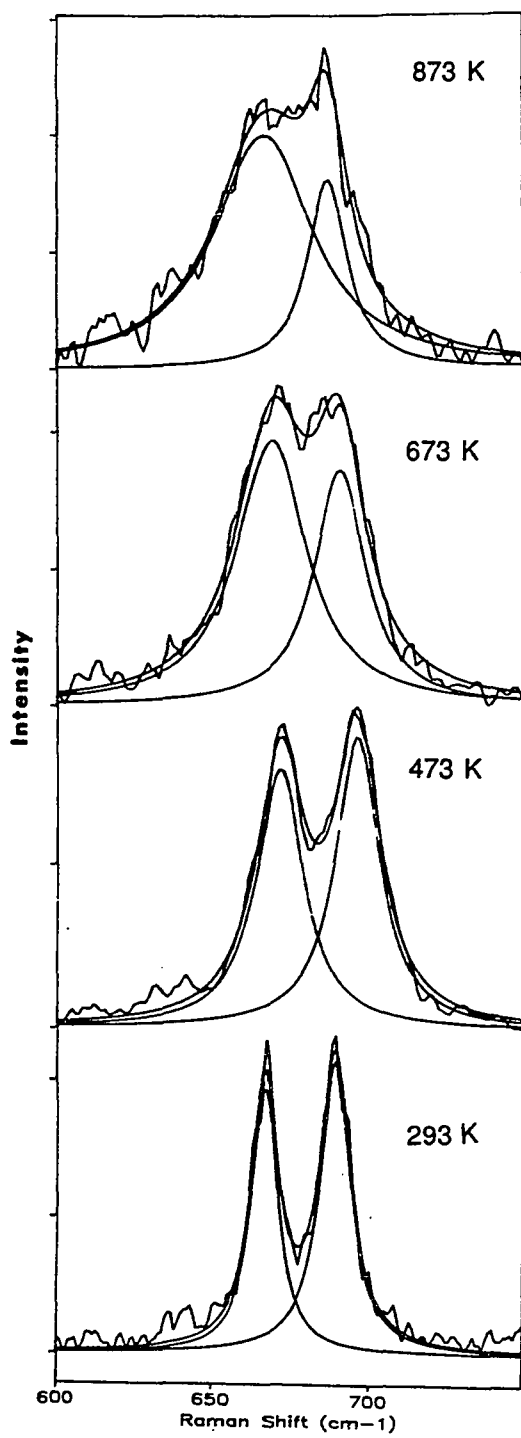


Figure 54. Curve fitted spectra of enstatite at various temperatures in the 600-750 cm⁻¹ region.

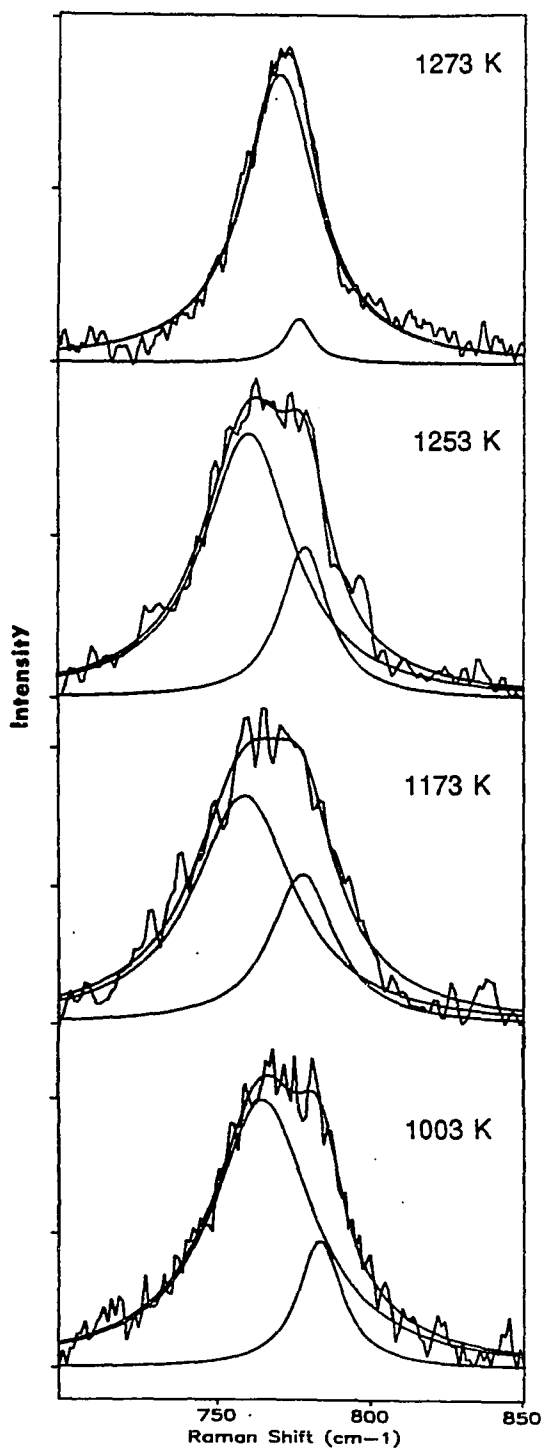


Figure 55. Curve fitted spectra of enstatite at various temperatures in the 600-750 cm⁻¹ region.

the individual peaks from the curve fitted results are plotted against temperature in Fig 56 and corresponding band width are in Fig. 57. Both peaks show a linear decrease in frequency with temperature. However, the peak at 1034 cm^{-1} has a higher slope than 1014 cm^{-1} . This implies differential variation in the bond length for the bridging and non-bridging oxygen. The variation of the Raman bands in the 660 cm^{-1} region is shown in Fig. 58. These bands originate from the symmetric stretch of the Si-O-Si bond. It is noted that the Raman frequency of these bands, 668 cm^{-1} and 666 cm^{-1} , decrease rapidly above 9500 C . Their band width, unlike the high-frequency bands, does not obey a linear relationship with temperature (Fig. 59). In Fig. 60 and Fig. 61 the frequency and band width for the band at 85 cm^{-1} vs temperature is plotted. It shows that at the transition temperature ($>1200\text{ K}$), the Raman frequency drops rapidly. The band width of the band increases rapidly at the transition temperature. High-temperature structural studies of orthopyroxene up to 8500 C (Smyth, 1973) suggest a differential expansion rate for T-O and M-O bonds, which causes the kinked chain to straighten out. It is also, found that the bond length of $(\text{Si}-\text{O}_b)$ decreases much faster than the $(\text{Si}-\text{O}_{nb})$ bond. This is clearly seen in the Raman spectra at high temperatures. Differential expansion of the (M-O) bond is the primary reason for the straightening of the silicate chain and the main cause of the effect of temperature effect on the crystal structure.

Clino-enstatite has two polymorphs: low- and high-clinoenstatites. The temperature dependence of Raman spectra between 293 K and 1293 K of low-clino enstatite are shown in Figs 62 and 63. A few deconvoluted bands in the high-frequency region are shown in Fig. 64 and 65. Also, the results are tabulated in Table 14. The clino-enstatite undergoes low-to-high phase transition at 1273 K . At the transition temperature, Raman bands show non-linear frequency variation. Transition is also marked by the appearance of two new bands, one at 131 cm^{-1} and another at 155 cm^{-1} . At high-temperature ($>1000\text{ K}$), peak at 1014 cm^{-1} falls at a much faster rate than

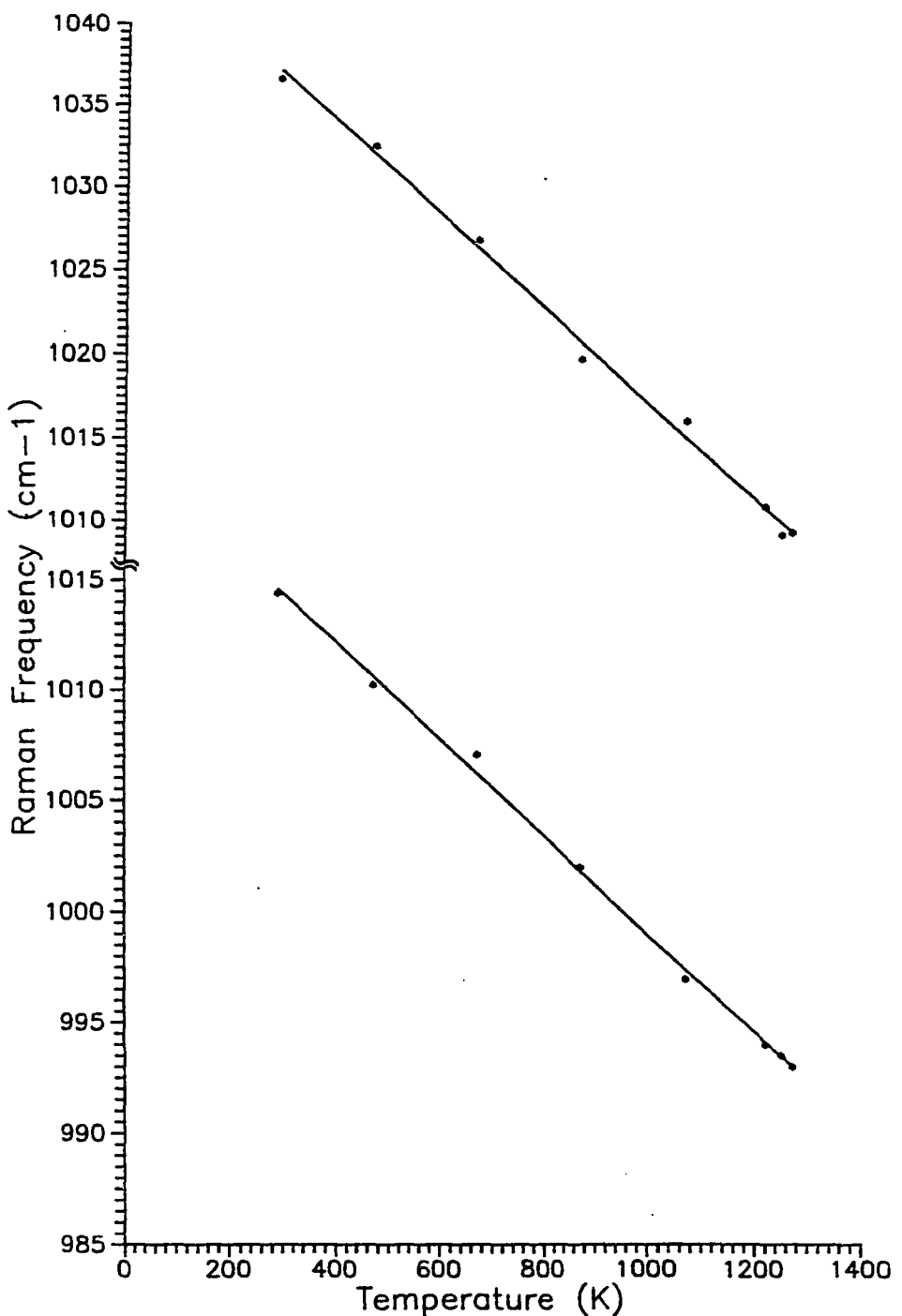


Figure 56. Stretching frequencies due to the Si-O- shows linear variation in the Raman frequency with temperature.

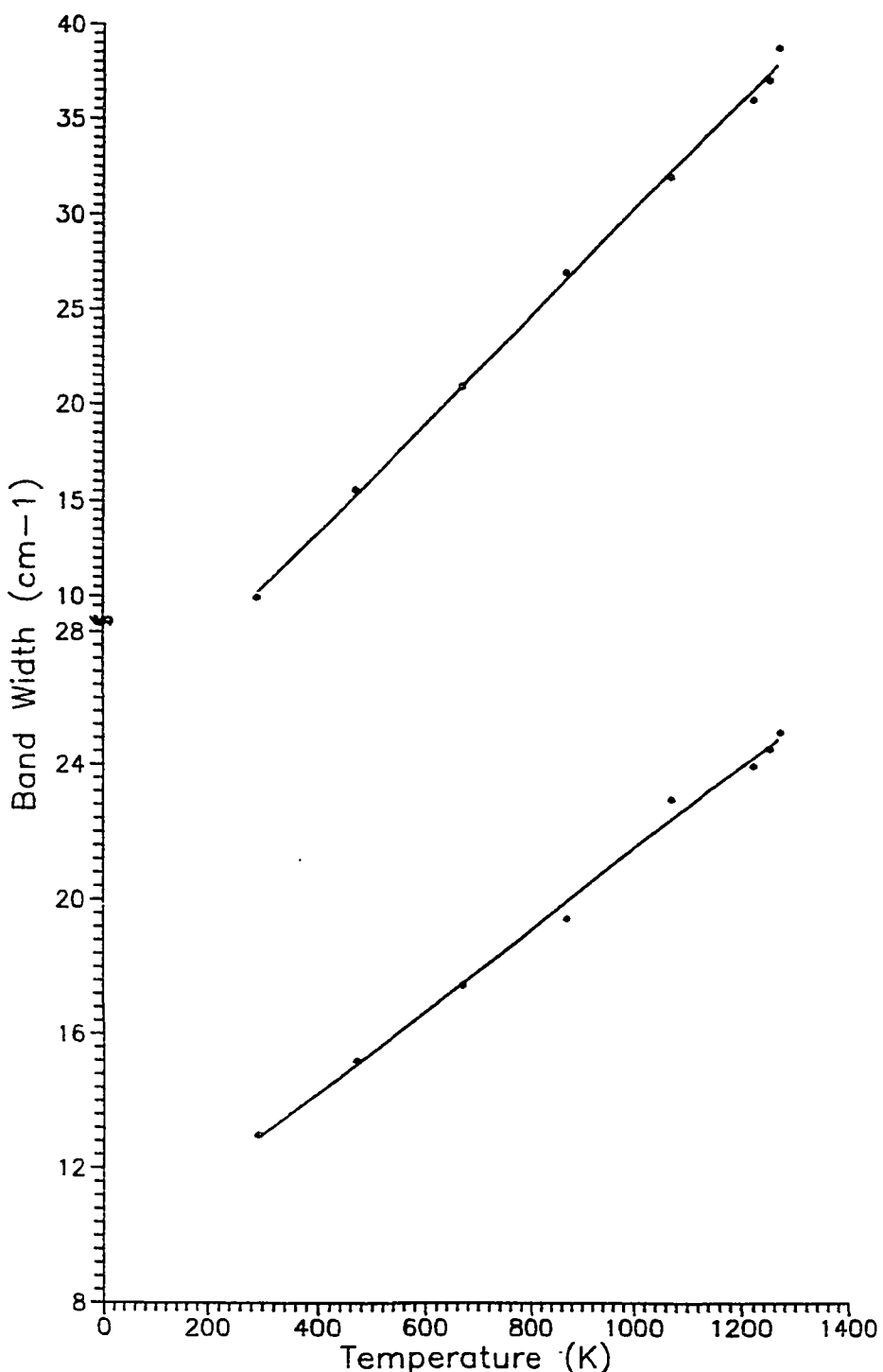


Figure 57. The band width of the stretching bands also show linear trend in its changes with temperature.

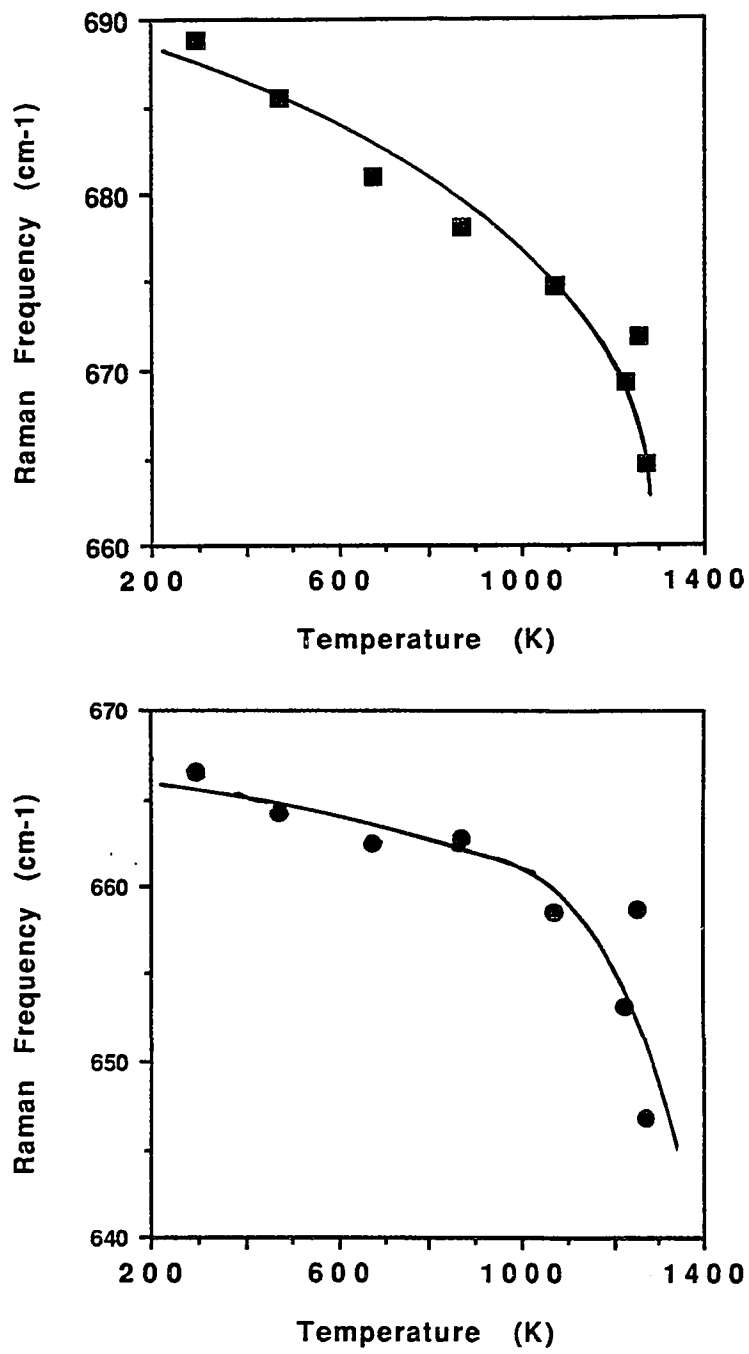


Figure 58. A plot of the behavior of the 666.5 cm^{-1} and 688.9 cm^{-1} bands with temperature.

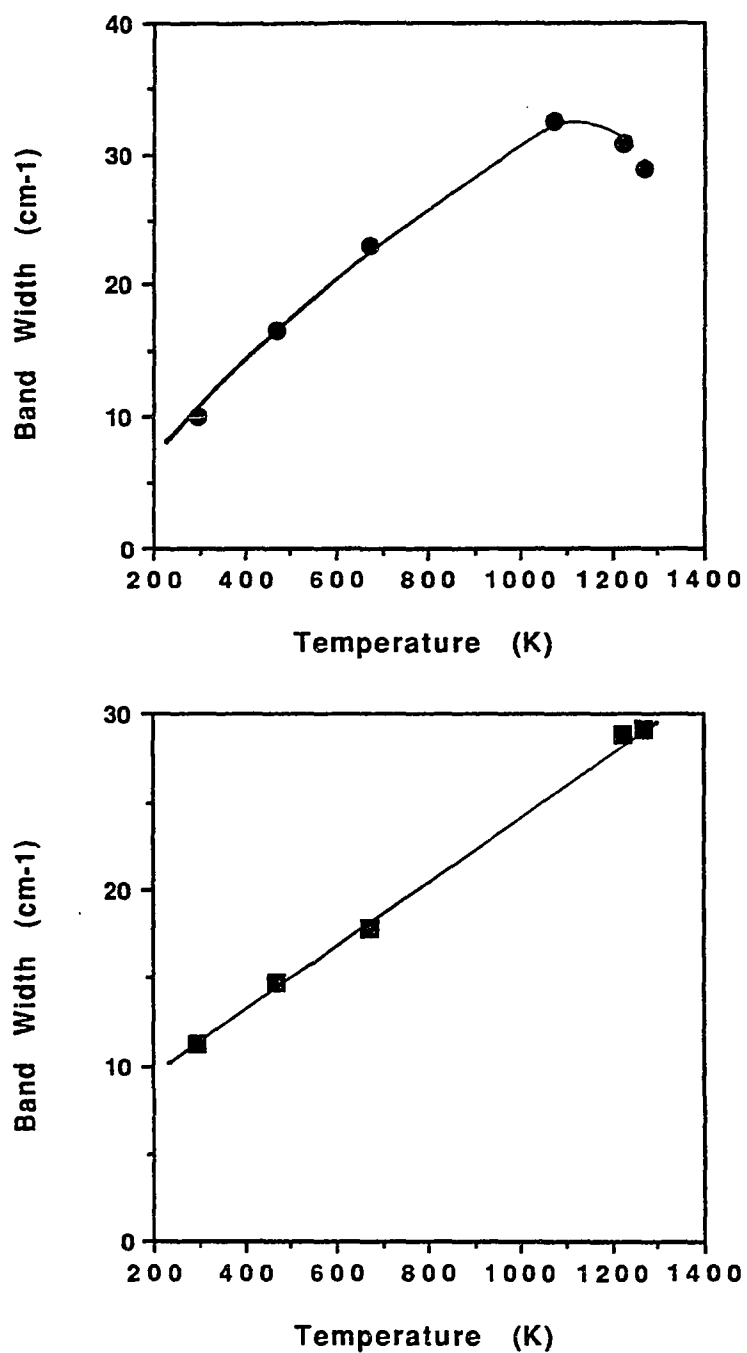


Figure 59. Variation of band width of the symmetric stretching bands.

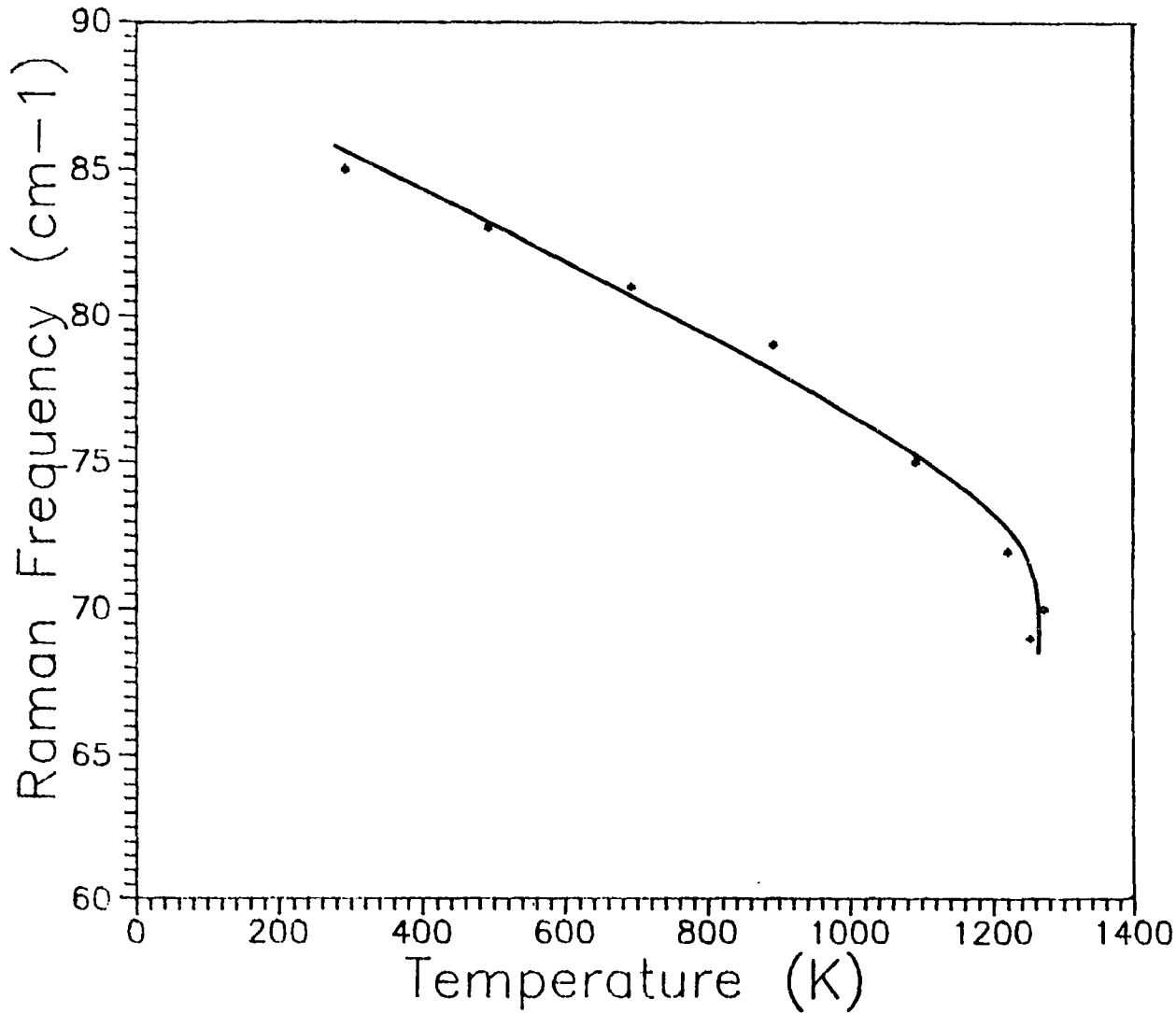


Figure 60. The transition from ortho-to-clino enstatite is marked by the sudden changes in the Raman frequency. Band at 85 cm^{-1} shows sudden decrease in frequency around 1200K.

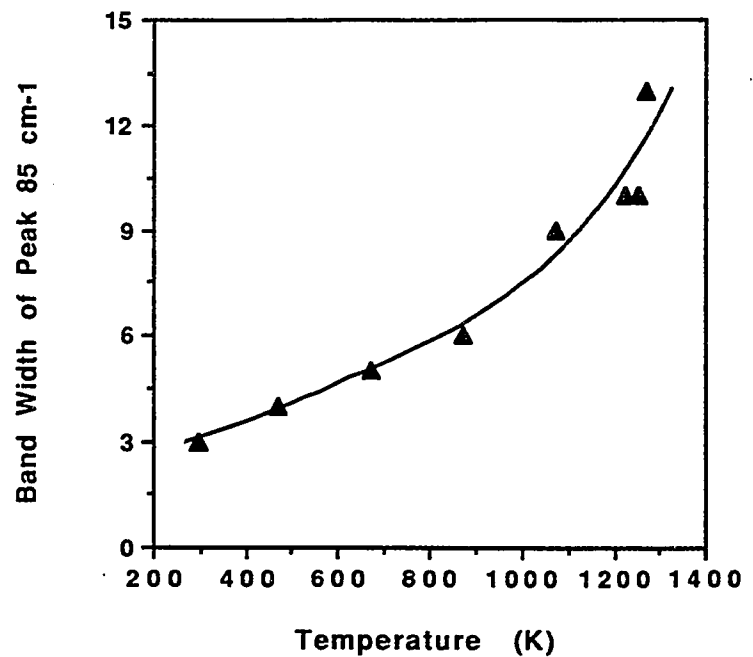


Figure 61. Band width of peak 85 cm^{-1} . It is fitted to a polynomial equation.

Table 13: Curve fitted results for enstatite and clino-enstatite Raman bands

temp(K)	ensfreq1	ensfreq2	ensbw1	ensbw2	bwens85
293.000	666.510	688.851	10.060	11.260	3.000
473.000	664.230	685.446	16.570	14.847	4.000
673.000	662.393	680.992	22.960	17.810	5.000
873.000	662.735	678.060		10.230	6.000
1073.000	658.582	674.752	32.465	13.990	9.000
1223.000	653.195	669.295	30.797	28.790	10.000
1253.000	658.757	671.840			10.000
1273.000	646.744	664.640	28.850	29.066	13.000

temp. (K)	censh.freq1	censhifreq2	censbw1	censbw2	censlfrq1	censlfreq2	bw1	bw2
293.000	10'5.200	1037.400	12.000	15.360	668.590	691.470	10.700	10.600
473.000	10'2.610	1034.630	16.040	15.630	665.750	688.220	17.880	16.750
873.000	1007.290	1027.260	20.640	18.280	663.010	683.570	20.660	17.790
1073.000	998.300	1015.960	24.990	19.200	657.590	674.470	25.830	19.660
373.000	1014.600	1036.500	11.410	15.680	668.330	690.720	13.130	12.960
1073.000	996.740	1014.210	24.990	24.738				
1273.000	968.430	1003.960	28.540	41.600	635.000	658.000	28.000	27.000

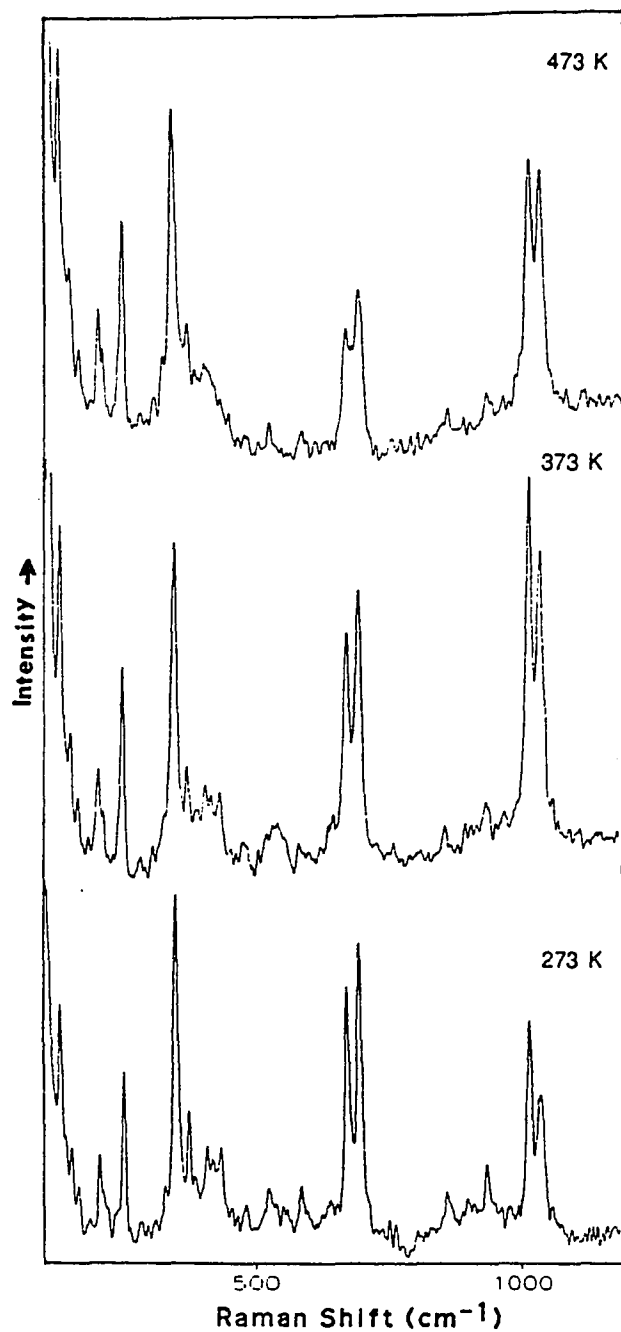


Figure 62. Raman spectra of clino-enstatite at high temperature.

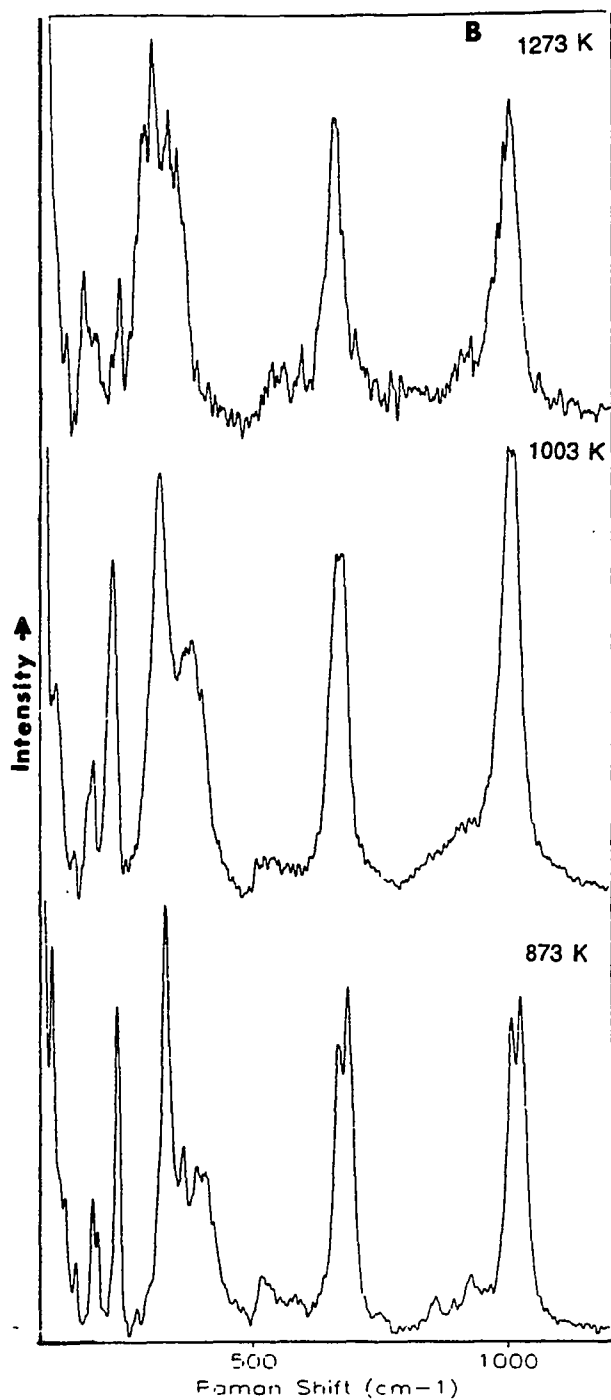


Figure 63. Raman spectra of clino-enstatite at high temperature. Sharp bands in the low frequency changes drastically with temperature.

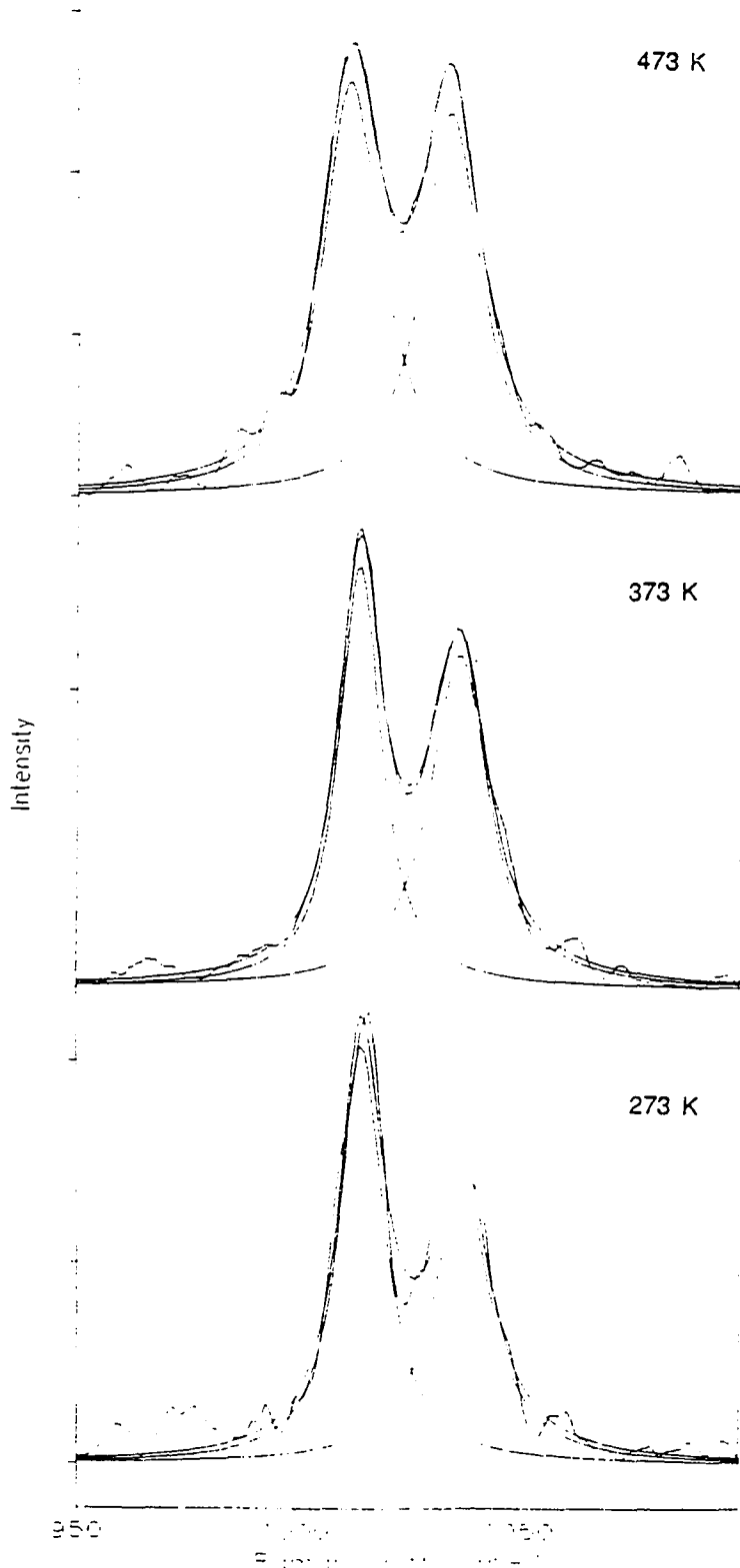


Figure 64. The Si-O⁻ stretching bands in the 950-1000 cm⁻¹ region is resolved with the help of a curve fitting program

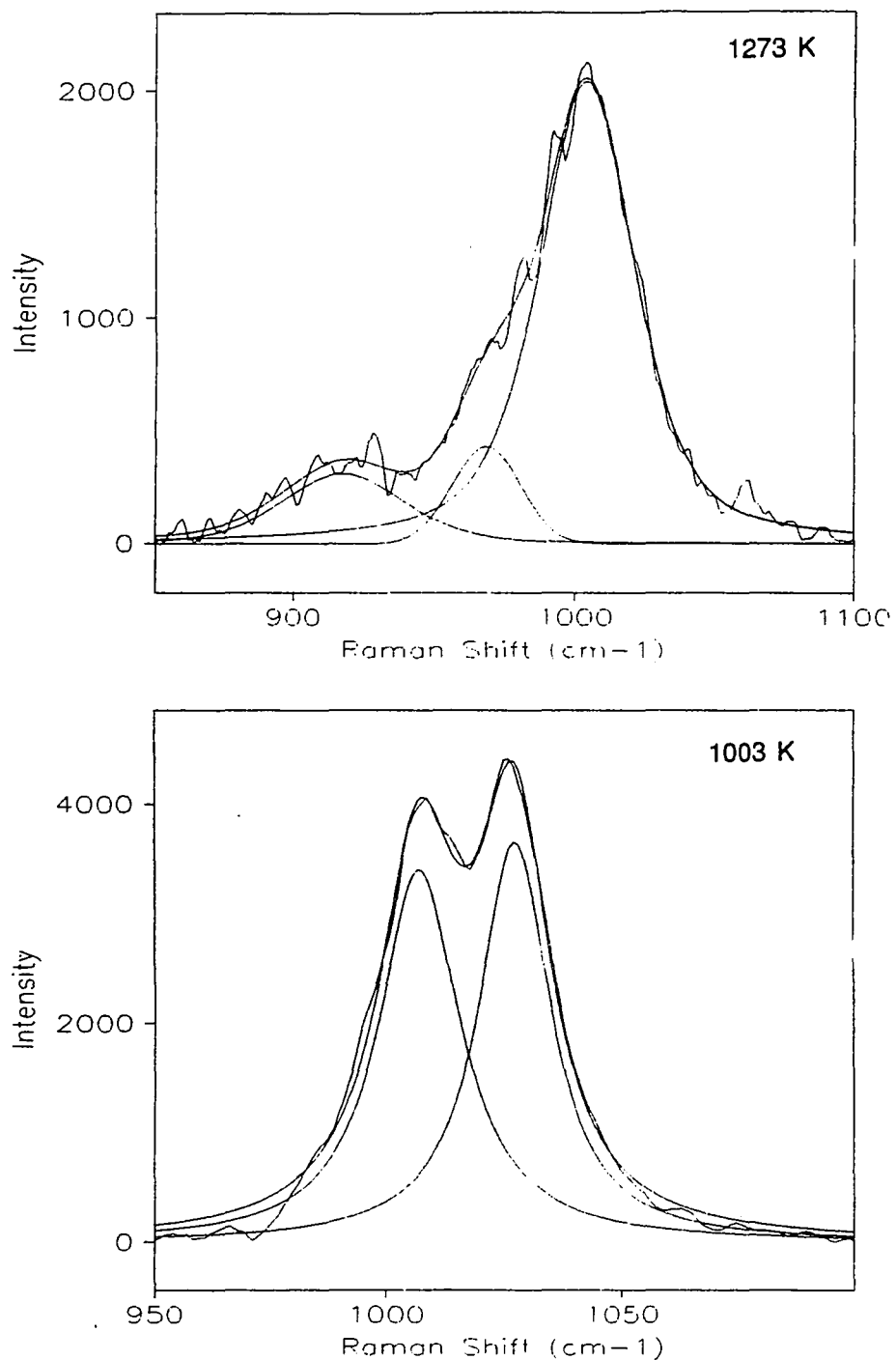


Figure 65. The Si-O⁻ stretching bands in the 950-1000 cm^{-1} region is resolved with the help of a curve fitting program.

1037 cm^{-1} band (Fig. 66). The band width of 1015 cm^{-1} shows almost a linear increase with temperature while the band at 1036.6 cm^{-1} represents a sharp increase in band width above 1050° C (Fig. 67). In the medium frequency region, 666.8 cm^{-1} band falls off faster than the 692 cm^{-1} band and their band with varies linearly with temperature (Fig. 68 and Fig.69).

4.8 Suggestion for future work

For a complete understanding of the crystal structure of pyroxenes more experiments have to be conducted. High pressure laser spectroscopic studies of pyroxenes have not been done. It is very important that we should have the high pressure vibrational data to calculate the thermodynamic parameters. As mentioned earlier (Chapter 2), high pressure spectroscopic technique is the only method available at present to determine the thermodynamic parameters and they are needed for the modeling of the earth interior.

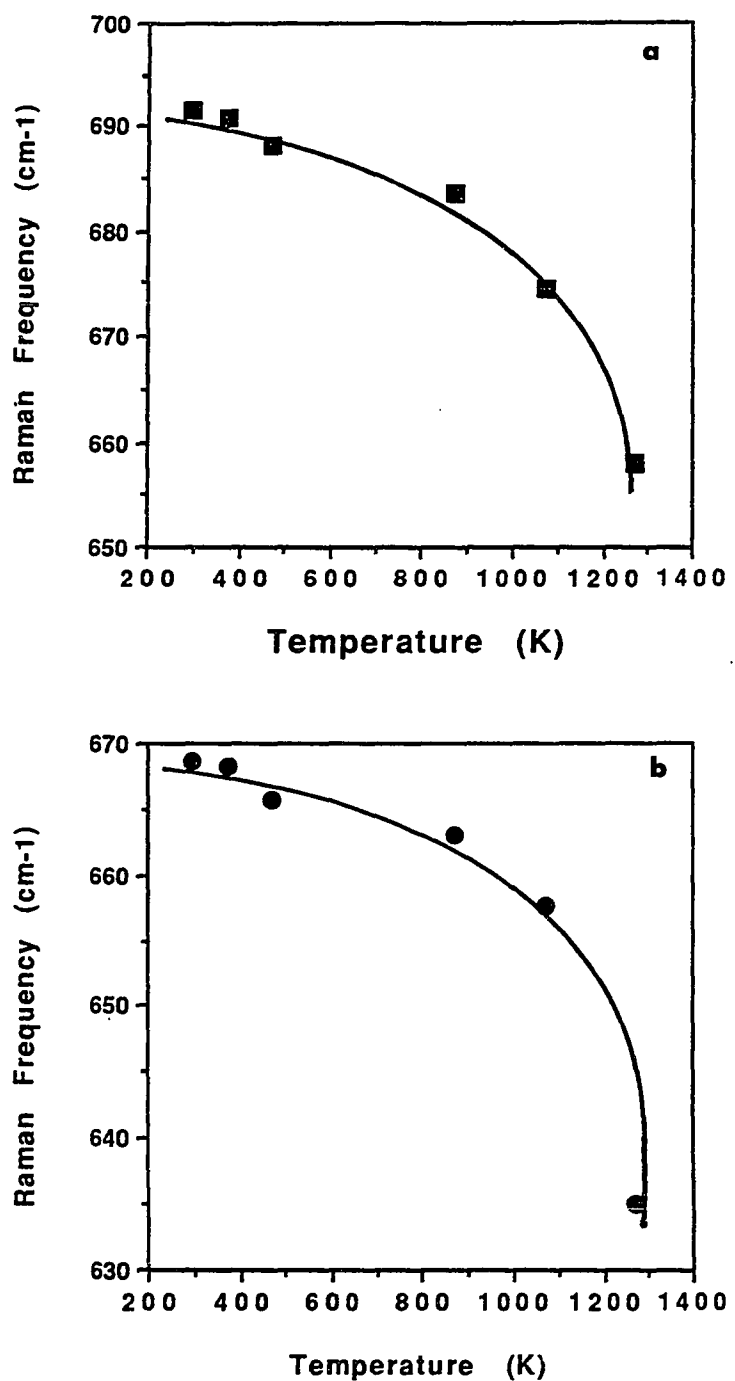


Figure 66. Variation of the Raman frequency of resolved peaks in the high frequency region. The band at 666 cm^{-1} shifts faster than the one at 690 cm^{-1} .

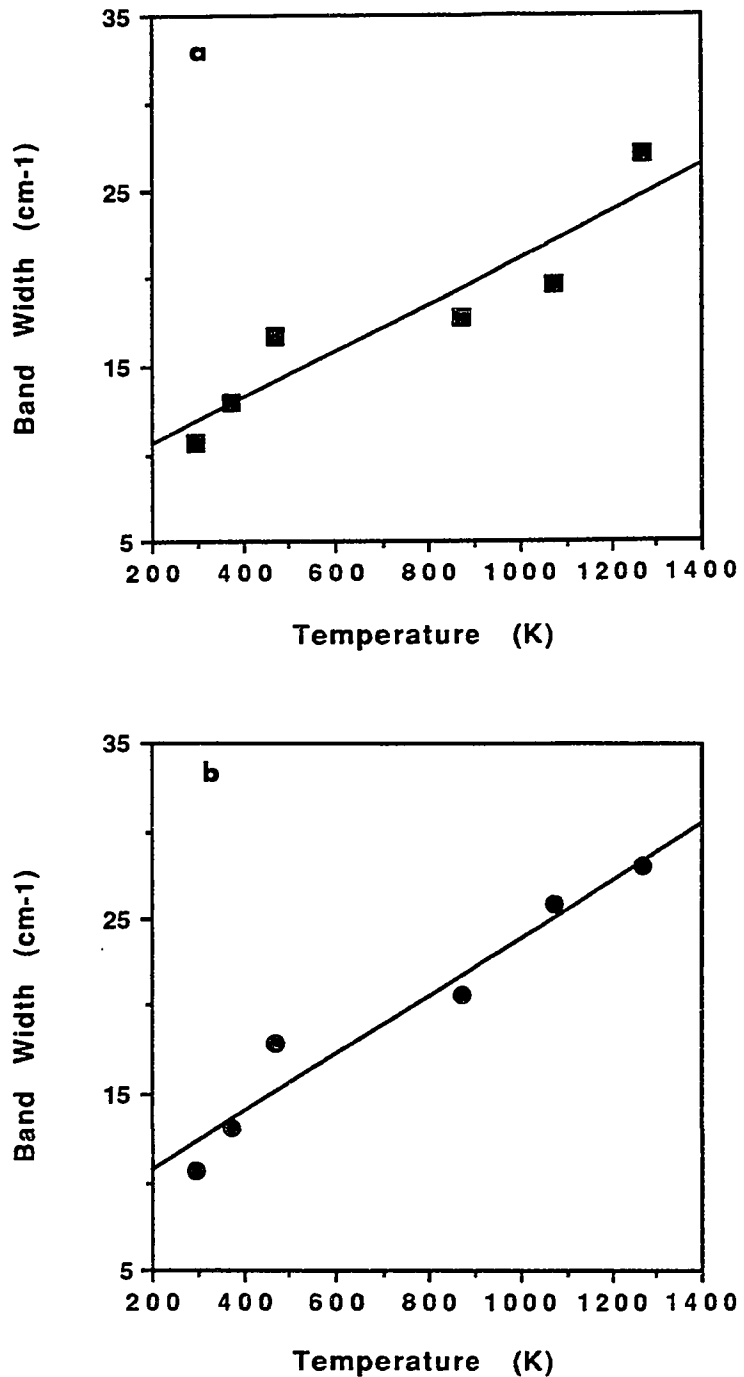


Figure 67. The band width of the high frequency bands show linear variation.

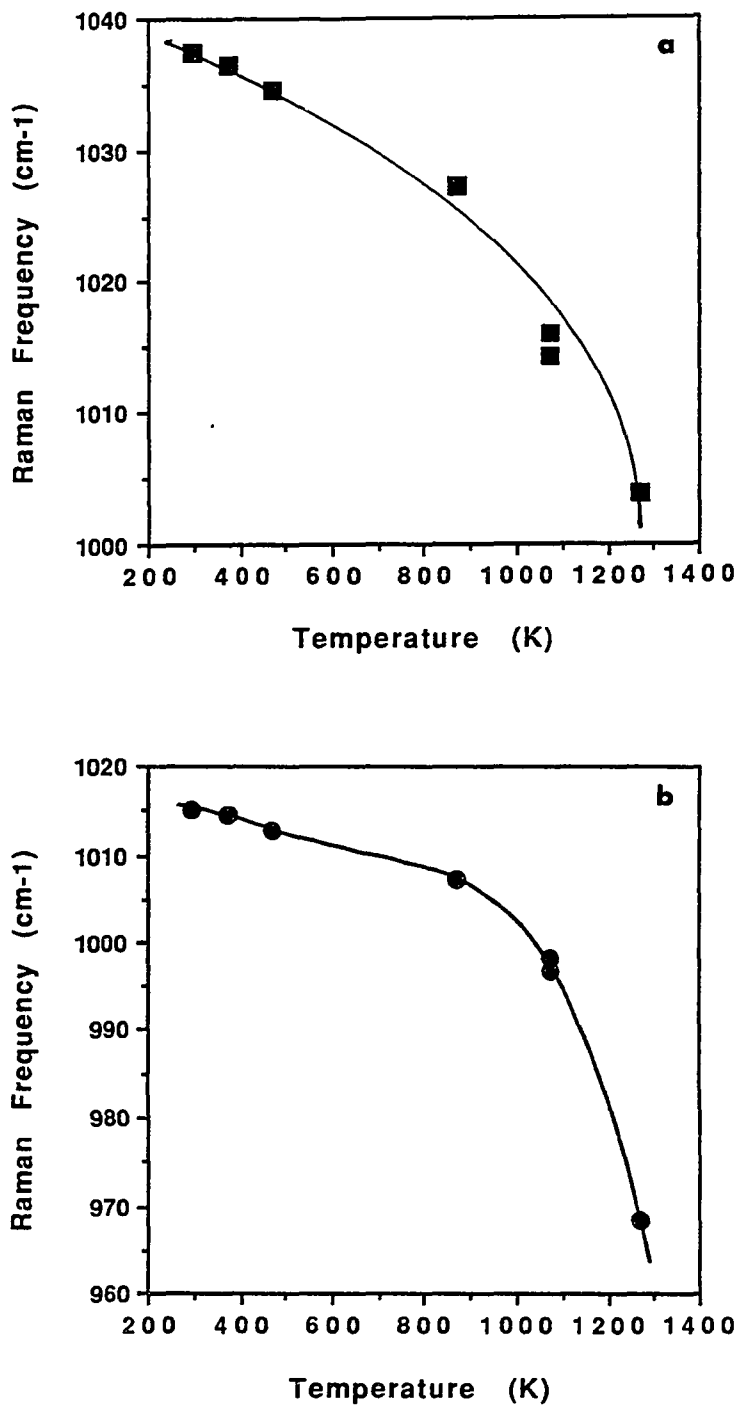


Figure 68. Variation of Si-O⁻ stretching frequencies with temperature.

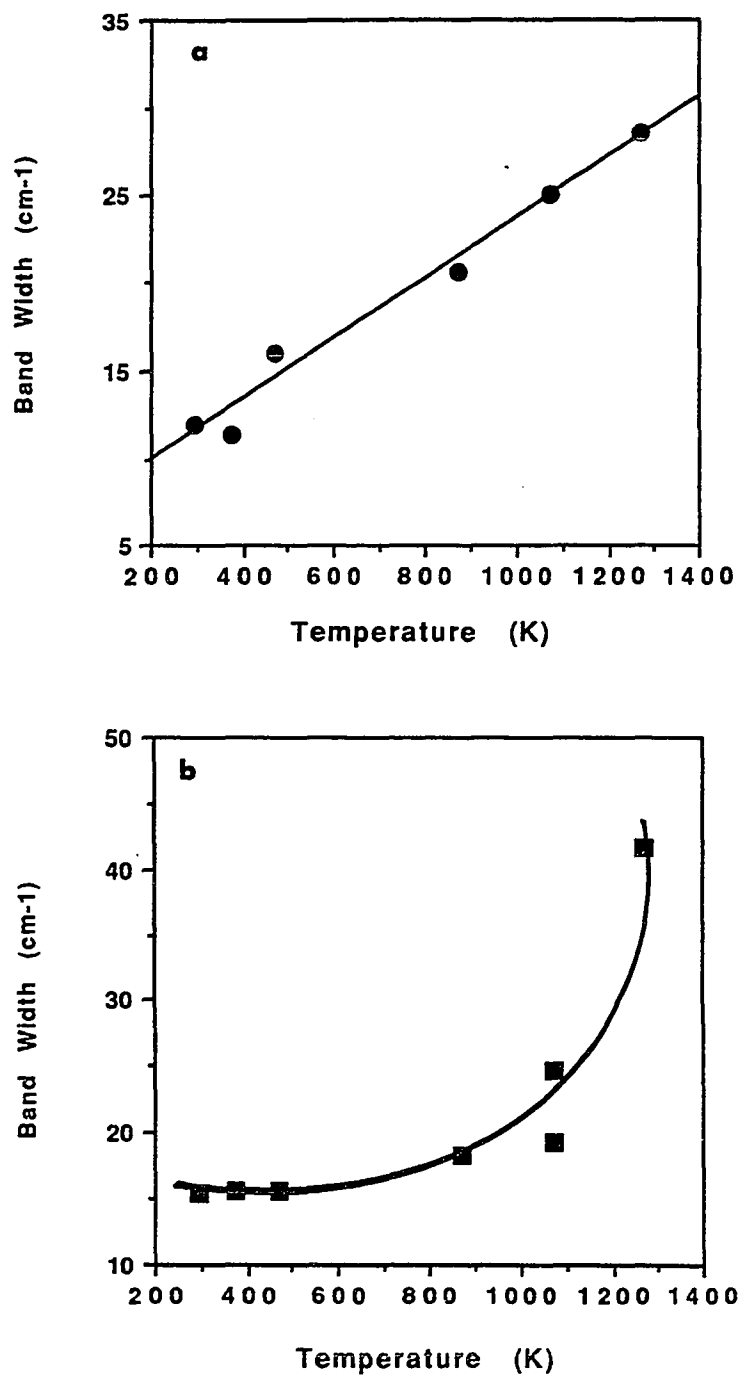


Figure 69. The band of the high-frequencies show that the 1015 cm⁻¹ peak shows a large increase in the band width than the 1037 cm⁻¹ peak.

CHAPTER 5

RAMAN AND IR SPECTROSCOPIC STUDIES OF AMPHIBOLE CRYSTALS

It is well known that volatile components play an important role in determining the chemical and physical properties of magmatic melts. The presence of water and other volatiles such as CO₂ and F₂, has a dramatic effect on the solidus and liquids curves (Hall, 1987), viscosities of silicate melts (Kushiro, et al., 1976), and the oxidation state of magmas (1978). It is, therefore, of interest to study the nature of hydroxyl ions and their interaction with cations in hydrous silicate minerals. Hydrous silicate minerals crystallize at very high pressures and temperatures deep inside the earth. Modern scientific advances have provided us new opportunities for examining hydrous minerals under high pressure in the laboratories. The applications of Diamond Anvil Cell (DAC) in earth science have been a stepping stone in past two decades. We are only beginning to understand the role of volatiles in the making of silicate rocks. This chapter describes a study that was undertaken to investigate the structural role of the hydroxyl ions in amphibole crystals at ambient as well as high pressures. A few measurements were also carried out at low temperatures to verify some of the earlier results (Wang, et. al., 1988) on the low temperature behavior of the hydroxyl bands in binary amphiboles.

Amphiboles belong to the most complex rock forming mineral group. They are also one of the important mineral groups in igneous and metamorphic rocks. These are hydrous minerals and the presence of hydroxyl ions was first recognized by Schaller in 1916 in termolite (Schaller, 1916). Amphiboles exhibit a wide range of chemical composition and have several cation sites in the crystal structure. The hydroxyl group lies on the O₃ sites (Hawthorne, 1982) which interact with the nearest cations in the M₁, M₃, and A sites. Along with OH⁻, amphiboles also contain fluorine (F⁻) and

chlorine (Cl^-). It was found recently that the O₃ site could also be occupied by O₂⁻ ions in oxy- and Ti⁺ bearing amphiboles (Matson, et al., 1985).

Vibrational spectroscopy has been used to obtain information on the vibrational modes and cation distribution in the crystal structure (Sterns, 1974; Hawthorne, 1982). For minerals containing iron, Mossbauer spectroscopy has been utilized to distinguish between Fe²⁺ and Fe³⁺ cations through quadrupole splitting (Hawthorne, 1982b). But, in amphiboles the Mossbauer technique is not very successful because the crystallographic sites M₁, M₂ and M₃ are indistinguishable. As mentioned earlier, the hydroxyl group in amphiboles lies on the O₃ site and it interacts with M₁ and M₃ sites. Monitoring the vibrational characteristic of the hydroxyl modes one could infer the nature bonding of the cation sites. Infrared studies of amphiboles have been done on several end members (Burns and Sterns, 1966, Farmer, 1974). For example, by recording ir spectra of the cummingtonite-granulite series, Burns and Sterns were able to demonstrate the effect of cation substitutions on the hydroxyl bands. They observed emerging new bands and a systematic shift in the hydroxyl bands in this series as a result of varying cation content.

Raman studies on amphiboles are rare. One of the reasons is the difficulty in obtaining good spectra. The first Raman spectrum of amphibole, actinolite, in the low frequency region was reported by White (Karr, 1975). However, the author did not report any work in the hydroxyl stretching region. While the present work was underway, Raman spectra of five end member amphiboles were presented by Wang et al., 1989). Also, Raman spectra of glaucophane (Gillet and Tequi, 1989) and termolite (Blaha and Rosasco, 1978) are now available in the literature. Recently, Ventura, et al., (1991) studied the effect of Ti substitution in synthetic richerite amphibole with Raman, IR, and X-ray diffraction techniques. The present work was undertaken to investigate the role of hydroxyl in some of the Ti-rich amphiboles that have been studied

with mass spectrometry and microprobe analysis (Matson, et al., 1985). Another goal of this study is the determination of the detection limit of the hydroxyl bands in amphiboles with multichannel micro-Raman spectrometry.

5.1 Experimental methods

Raman spectra of the amphiboles were collected with a micro-Raman multichannel spectrometer with 135° scattering geometry as described in chapter 2. The Raman spectra were collected in two different frequency regions: the low-frequency ($100\text{-}1200\text{ cm}^{-1}$) spectra corresponding to the vibrations of tetrahedral and octahedral units and the high-frequency spectra ($3000\text{-}4000\text{ cm}^{-1}$) corresponding to the OH-stretching vibrations. The laser excitation frequency used in the low-frequency region was 488 nm and in the high-frequency region it was 457.9 nm. Both laser excitations were from an Ar⁺ ion laser (Spectra Physics laser Model # 2020). In both cases, approximately 12 mw of laser power was used at the sample. The low-frequency and high-frequency regions were separately calibrated before the spectral measurements of the sample as described in chapter 2.

In amphiboles the hydroxyl stretching bands are very weak, so it was very difficult to obtain a Raman spectrum with a good signal-to-noise ratio. Fluorescence in these samples added an extra task to the problem. To reduce these problems, a clean and flat surface of the sample was selected for collecting the spectrum. With the help of a micro-meter stage, a fine spot was searched for low background and yet with a strong Raman signal. An exposure time of approximately 5 seconds was used for the initial search. Once such a spot was located, the Raman spectrum was accumulated for approximately an hour or until a spectrum with a good signal-to-noise ratio was obtained.

Infrared measurements were carried out with a Perkin-Elmer interferometric instrument (Model 1700). All the measurements were done in the transmission mode. The spectra were collected in the 5200-400 cm⁻¹ region and 300 scans were accumulated for a good signal-to-noise ratio. The resolution of the spectrum was 4 cm⁻¹. The resulting spectrum was then converted into absorbance mode before plotting and spectral analysis.

5.2 Description of the samples

Amphibole crystals were collected from several locations in the United States. A detailed sample description is given by Matson, (1984), Garcia, et al., (1980), Matson, et al., (1984). The mass spectrometric pyrograms of volatile release indicated that these samples contain 0.487 to 1.578 wt% of total H₂O from the structurally bound hydroxyl group. Small amounts of F⁻ and Cl⁻ were also released from these samples.

For the present study, good-quality samples were hand-picked from the same collection that was used for the mass spectrometric and microprobe analyses. Samples were 2 to 4 mm² in size. They were dark to very dark in appearance. A clean and flat surface was used for Raman scattering experiments. Careful examination of the samples before and after the experiments showed no damage to the sample surface from laser heating. For IR experiments, samples were cut into thin sections and then polished to a high degree. To achieve this, the samples were mounted onto a glass slide using Canada balsam and then coarsely ground using an Ingram thin section grinder. The sample was then mounted onto a lapping wheel (Logitech Model No. LP30) and the thickness cut further down to about 110 µm. The final polishing was carried out on a polishing wheel with 3 µm aluminum powder to the desired thickness. The thickness of the samples was carefully measured with a digital micrometer. The sample names and their measured thickness are given in Table 14.

Table 14: Name of the amphiboles, their thickness, chemical composition and observed vibrational bands . . .

Sample No.	Sample	Thickness(um)	H2O	F	MgO	FeO	TiO2	Raman	IR Freq(cm-1)	HW (cm-1)	Area
1	VT122377	101.40	1.578	0.070	14.99	7.68	3.86	3685.0	3677.0	81	17.140
2	salt lake	98.33	1.467	0.065	11.09	11.81	4.33	3670.0	3688.0	83	21.890
3	soda spring	57.83	1.180	0.093	9.46	15.45	5.03	3685.0	3680.0	73	11.800
4	HD106434	88.70	1.452	0.104	13.58	8.89	5.49	3677.0	3678.5	81	17.990
5	HD 134924	112.16	1.085	0.126	13.74	8.63	5.78	3675.0	3679.0	85	20.590
6	Peridot Mesa	101.40	1.003	0.115	10.84	12.62	4.77	3670.0	3663.0	82	18.260
7	LC	107.70	0.487	0.225	11.29	11.67	5.85			80	1.950
8	X-146	102.33	1.250	0.120	16.03	7.18	2.61	3688.0	3679.6	128	57.603
9	X-17	102.80	1.190	0.110	15.63	7.01	2.76	3683.0	3680.0	119	4.300
10	X-225	110.16	1.070	0.120	14.21	9.48	3.32	3677.0	3679.5	102	35.130
11	X-223	99.80	0.990	0.070	15.54	7.91	3.36		3678.0	90	19.654
12	X-178	103.40	0.840	0.160	13.39	10.20	4.50	3660.0	3672.0	88	22.250
13	X-178	102.70	0.900	0.320	12.95	10.96	3.30	3685.0	3678.0	86	22.740
14	X-166	97.00	1.170	0.310	15.81	8.81	2.78	3695.0	3678.0	101	32.164
15	M2	100.00	0.870	0.280	12.95	9.10	3.49	3685.0	3681.0	86	26.106

5.3 Theoretical analysis

As pointed out earlier, the amphibole structure has double chained tetrahedra extending to infinity and is parallel to the crystallographic c-axis (Fig. 70). There are five structural types of amphiboles although most of them belong to the monoclinic system and have a c2/m structural group. The general formula for amphiboles (Hawthorne, 1981) can be written as



where,

A = K, Na

C = Mg, Fe, Mn, Al, Fe³⁺, Ti

B = Na, Li, Ca, Mn, Fe²⁺, Mg²⁺

T = Si⁴⁺, Al⁴⁺

Factor group analysis for the c2/m structural type predicts the following number of vibrational modes in Raman and infrared (Wang et al., 1989):

$$\Gamma_{\text{total}} = 30 A_g(R) + 30 B_g(R) + 27 A_u(IR) + 33 B_u(IR) + A_u + 2B_u.$$

Out of these modes, one A_u mode and two B_u modes correspond to the acoustic modes and will not be active in the Raman or IR spectra. In the above equation, R and IR refers to Raman and IR active modes. If the A site in amphibole crystal structure is empty, then the number of modes change to 27 A_u and 33 B_u resulting in a total of only 120 vibrational modes. For an isolated $Si_4O_{11}(4^-)$ unit, with C_s symmetry, there are 39 vibrational modes each for Raman and IR.

$$\Gamma_{\text{internal}} (Si_4O_{11}^{4-}) = 20A_g(R) + 19 B_g(R) + 19 A_u(IR) + 20 B_u(IR).$$

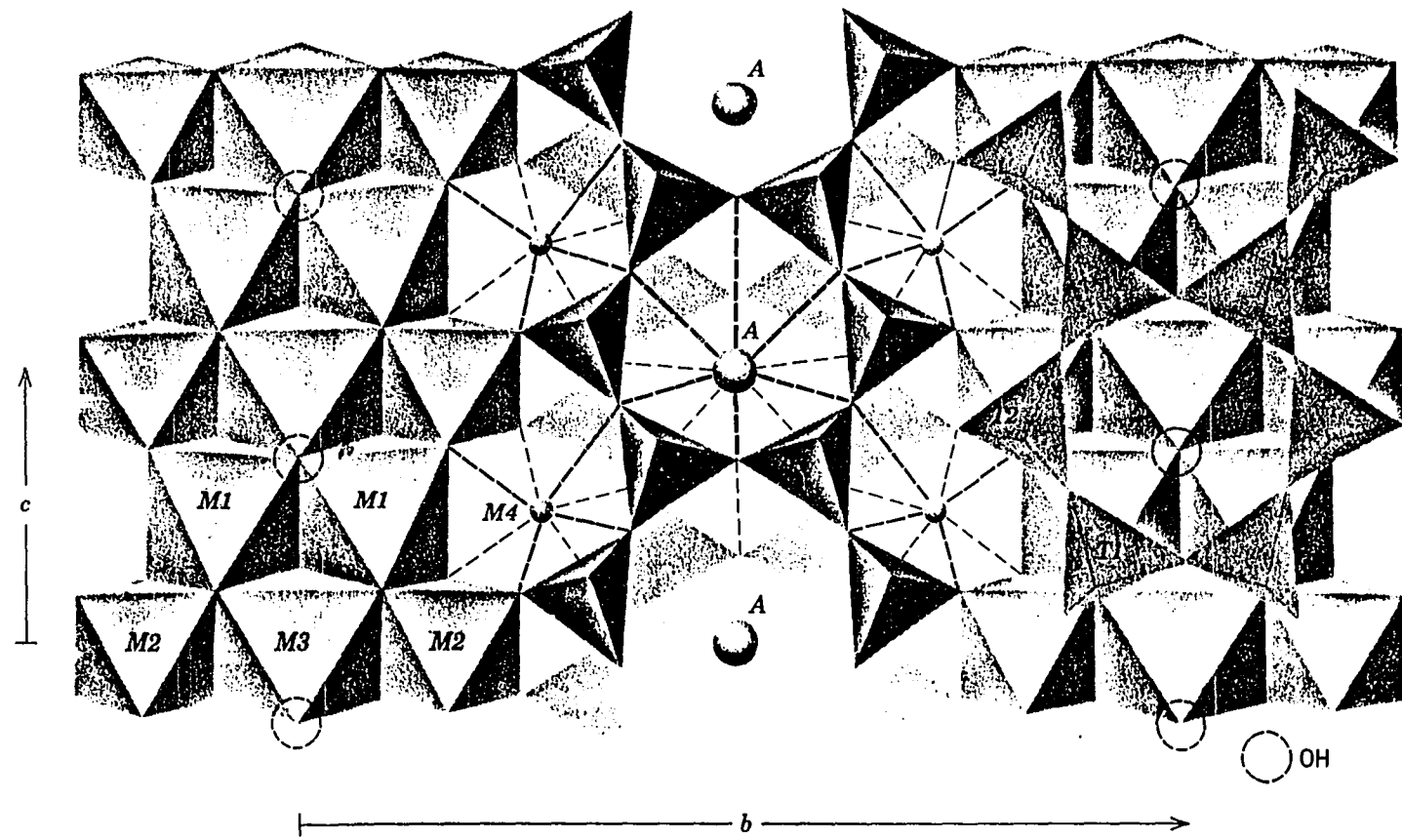


Figure 70. Crystal structure of monoclinic C₂/c amphibole projected on to *a* axis. (OH⁻) group is located at the center of the ring in the chain (after Dana, 1985).

In a primitive cell of a monoclinic amphibole there are two OH⁻ ions with their immediate neighbors being the M1 and M3 sites (Fig. 71). For an isolated OH⁻ ion there are only stretching modes. Therefore, the internal vibrational modes for these ions are

$$\Gamma_{\text{total}}(\text{OH}^-) = A_g(R) + B_u(IR).$$

The A_g stretching mode represent symmetric stretching motions of two OH⁻ ions and B_u represent their out-of-phase movements. Therefore, from the symmetry considerations, the same number of modes are observed in both Raman and infrared but at different frequencies.

The Raman bands of cummingtonite and actinolite in the OH⁻ stretching region are strong, distinctive, and resolvable. But, in the Ti-rich amphibole crystals from the Grand Canyon, the observed Raman and IR bands are broad and weak (see the discussion below).

5.4 Results and discussion

5.4.1 Raman spectra

Raman spectra of the amphibole samples were measured in two different regions: the low-frequency region (150-1100 cm⁻¹) and the high-frequency region (3000-4000 cm⁻¹). In the low-frequency region, wave numbers above 600 cm⁻¹ result from the internal mode of vibrations of tetrahedra. Below 600 cm⁻¹ the bands originate from angular distortions of the double chains and stretching vibrations of polyhedra containing cations from M and A crystallographic sites. In the 3000-4000 cm⁻¹ region (O-H) stretching vibrations are observed.

Raman spectra of two end member amphiboles, cummingtonite and actinolite, are presented in the frequency range 100-1100 cm⁻¹ in Fig. 72. The chemical composition

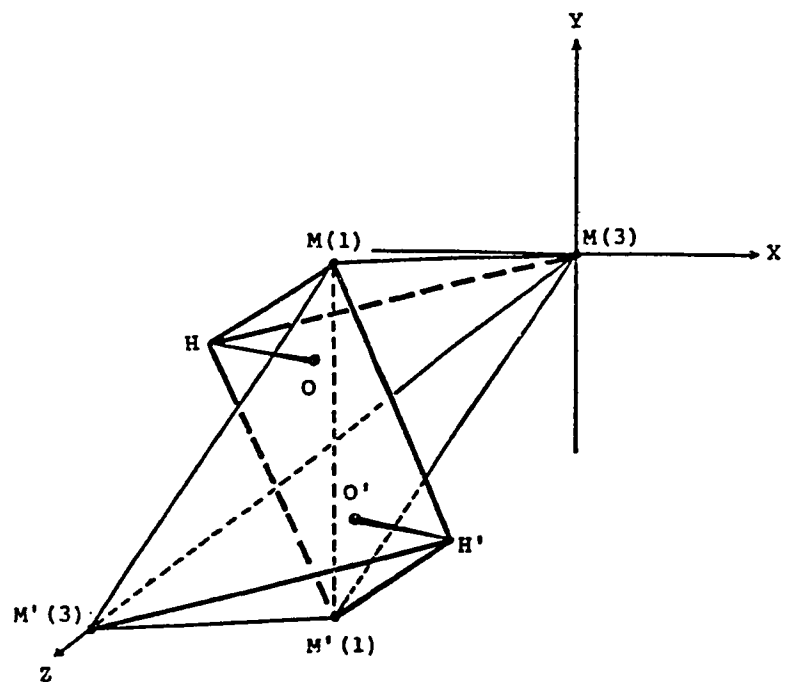


Figure 71. Detailed schematic diagram showing the location and direction of OH⁻ vector with respect to the M1 and M3 cations.

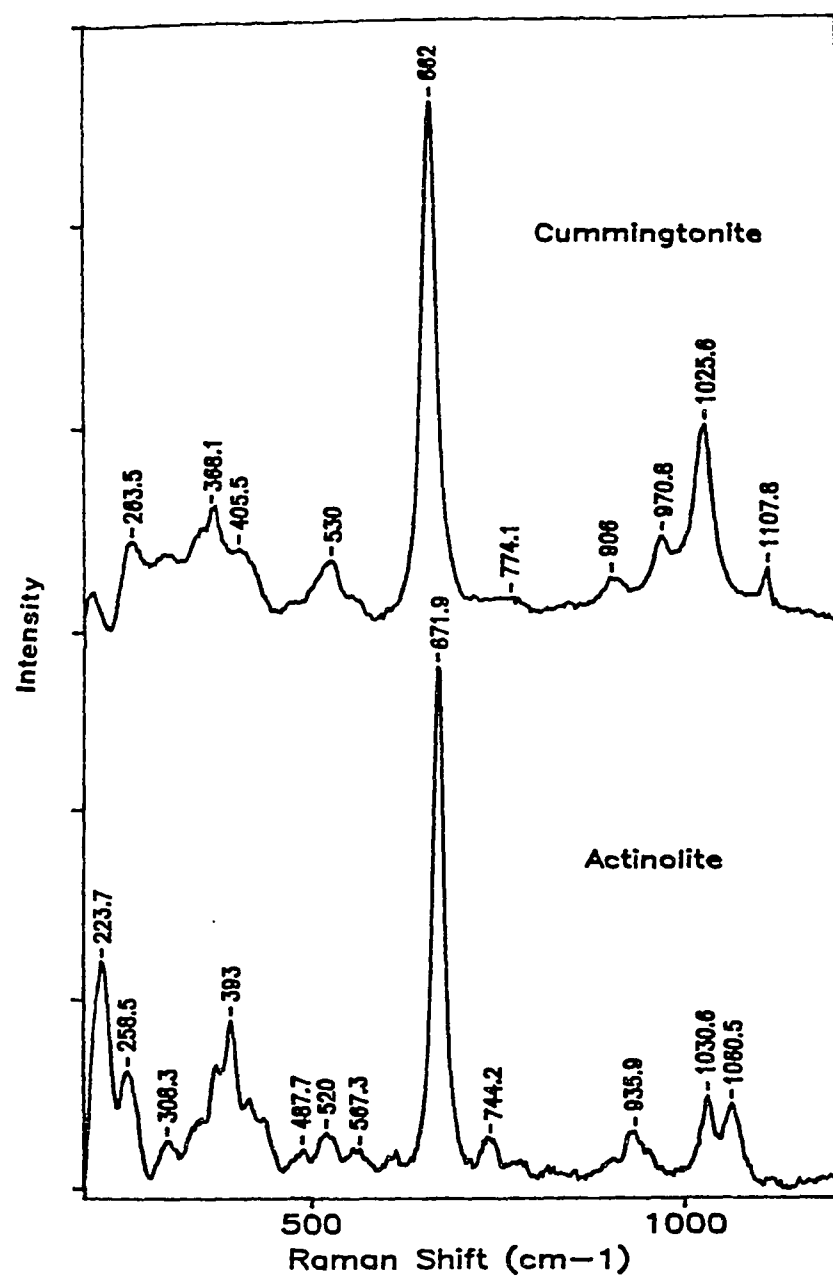


Figure 72. Raman spectra of cummingtonite and actinolite at room temperature.

of the end member amphiboles cummingtonite and actinolite are $Mg_7Si_8O_{22}(OH)_2$ and $Ca_2(Mg,Fe)_5Si_8O_{22}(OH)_2$, respectively. However, the microprobe analysis of these samples used for the Raman measurements indicated the following chemical compositions (elemental compositions are given in wt% and analysis for H_2O not included):

<u>Sample</u>	<u>Mg</u>	<u>Ca</u>	<u>Fe</u>	<u>Al</u>	<u>Na</u>	<u>K</u>	<u>Mn</u>	<u>Si</u>	<u>Ti</u>
Cummingtonite:	22.58	12.75	4.01	0.82	0.65	0.03	0.18	57.46	0.00
Actinolite:	8.19	0.12	38.68	0.41	0.08	0.02	0.59	50.22	0.06

In both spectra, the strongest band is assigned to the symmetric stretch ($\nu_1[A_g]$) of Si-O_b-Si vibrations. In cummingtonite A_g band appears at 662 cm^{-1} and for actinolite it is at 671.9 cm^{-1} . The bands above 800 cm^{-1} are attributed to the Si-O_b-Si and O_b-Si-O_b anti-symmetric stretching and Si-O_{n b} stretching vibrations. In amphiboles, bridging oxygen atoms are labelled O(5), O(6) and O(7), and the non-bridging oxygens are O(1) and O(2). In the spectrum of cummingtonite, a single strong band appears at 1025.6 cm^{-1} while in actinolite, there is a doublet consisting of bands at 1030.6 cm^{-1} and 1060.5 cm^{-1} (Fig. 73). Wang, et al., (1988) have measured the polarized Raman spectra of five amphibole crystals including cummingtonite and actinolite. Compared to the present data, the high-frequency bands in their spectra are very weak. However, the low-frequency bands are more distinctive and clear. In cummingtonite they have assigned 662 cm^{-1} and 1025 cm^{-1} bands to A_g modes. In actinolite the 672 cm^{-1} band is assigned to A_g mode and the bands above 672 cm^{-1} to B_g modes. In the spectrum of cummingtonite, bands below 600 cm^{-1} are broad and weak in contrast with the spectrum of actinolite in which the bands are more distinctive and sharper (Fig. 72).

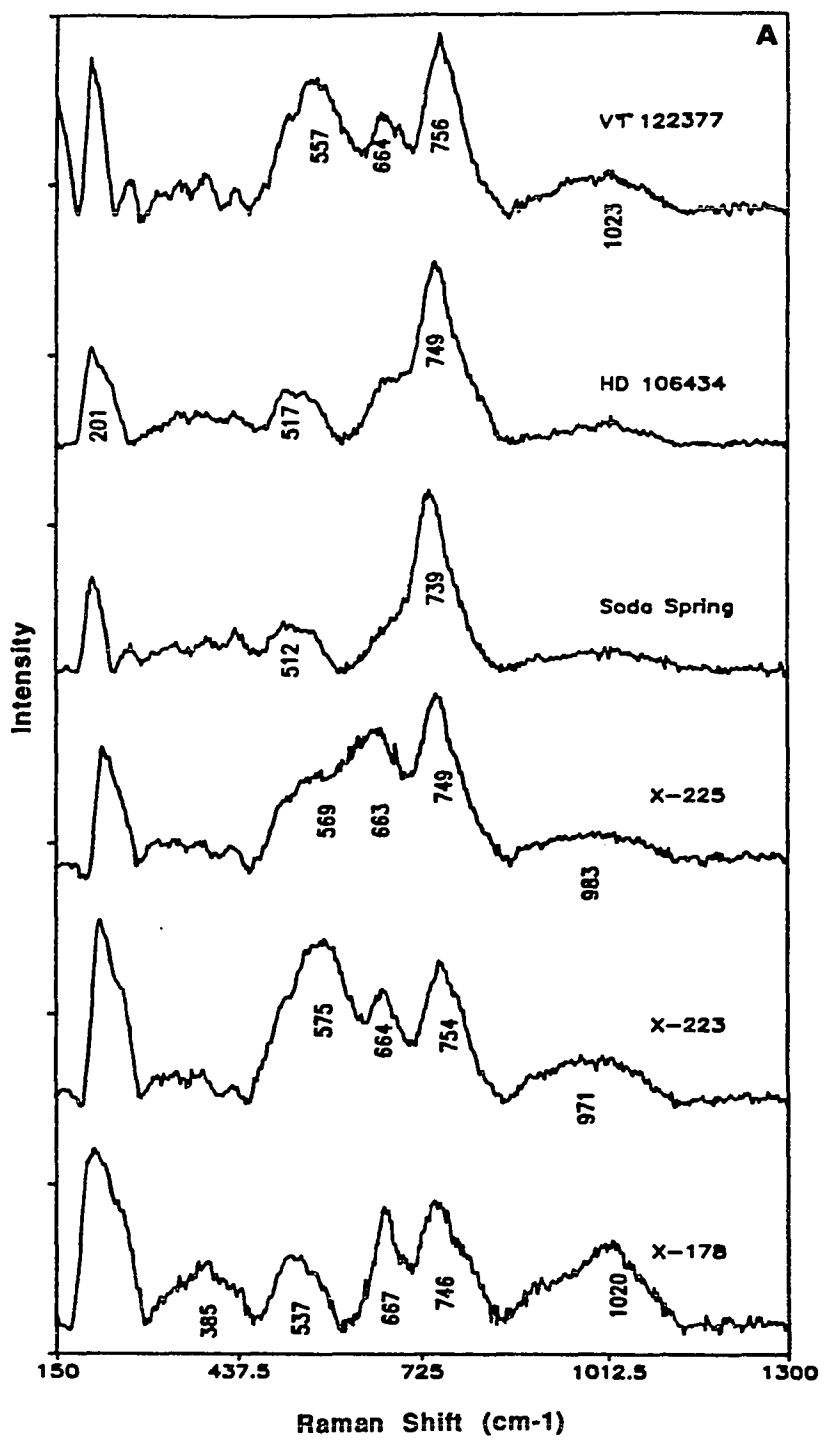


Figure 73. Raman spectra of the amphibole crystals in the frequency ($150\text{-}1300\text{cm}^{-1}$) region.

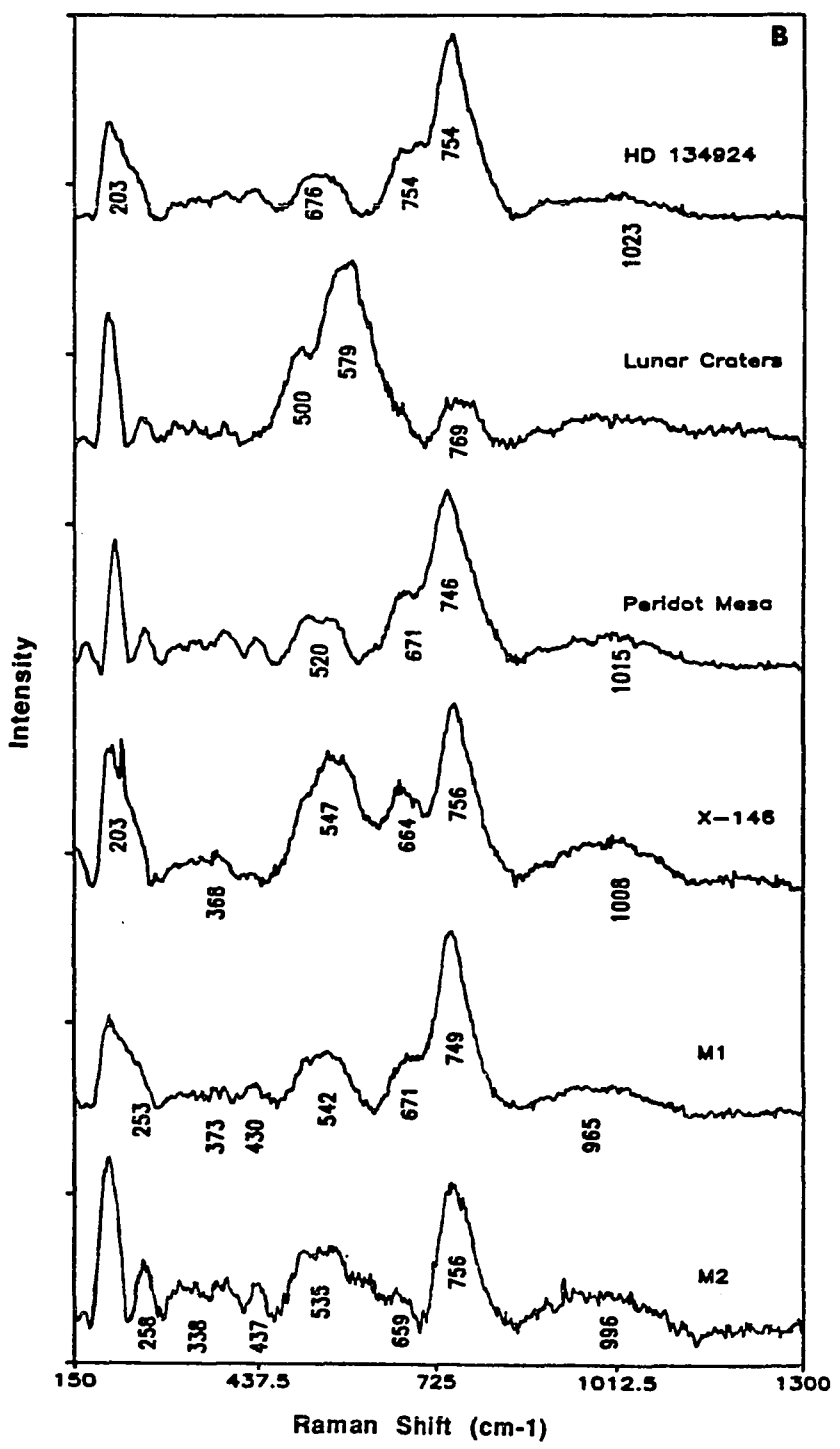


Figure 73. Raman spectra of the amphibole crystals in the frequency ($150\text{-}1300\text{cm}^{-1}$) region.

Raman spectra of twelve amphibole crystals including Ti-rich Keaersutite and Ferro-Keaersutite megacryst in the 150-1300 cm⁻¹ region are shown in Fig. 73. Their respective Raman frequencies are listed in Table 15. Compared to the end members cummingtonite and actinolite, these samples have very poor spectra. The strongest band appears at ~750 cm⁻¹, originating from the symmetric stretching of Si-O_b-Si bonds. A general observation of the spectra in the mid-frequency range, 500-800 cm⁻¹, reveals that all the twelve spectra can be grouped into three different types. Group one includes crystals with their strongest band appearing above 700 cm⁻¹. Group two has its strongest band between 500 cm⁻¹ and 600 cm⁻¹. Finally, group three has its strongest band below 600 cm⁻¹. This classification is only a general one because in most spectra there are multiple bands and they merge with each other in the 500-800 cm⁻¹ region. It is observed that the higher the Ti-content the lower the frequency of the symmetric stretching band. Also, the relative intensity of these bands increases with Ti content. Ventura, et al., (1991) have studied the substitutional effect of Ti in synthetic potassic richterite using X-ray diffraction studies and vibrational spectroscopy. They observed that in the mid-frequency region the intensity of the Raman band increases with increasing Ti content, but the number of bands remains the same. On the other hand, in the high-frequency region they reported the appearance of new bands. In the present work, the broad feature in the high-frequency region decreases considerably with Ti content. For example, in Soda Springs (Ti = 0.57 wt%) and HD 134924 (Ti = 0.63 wt%) samples, the high-frequency features (~1010 cm⁻¹) are barely visible. But in the X-178 (Ti = 0.37 wt%) and X-146 (Ti = 0.28 wt%) samples, the broad feature is very clearly visible. The changes in the intensity of the high-frequency band could be due to the presence of Ti⁴⁺ in the tetrahedral coordination. The Ti⁴⁺ substitution into the tetrahedra increases its distortion. At present, weak as well as broad spectral features along with the complex chemical constituents of the amphibole crystals make it very

Table 15: Observed Raman bands of Ti-rich amphiboles
in the 100-1200 cm⁻¹ region

Sample	Raman Frequency (cm ⁻¹)																			
	213.7	261.0	315.8	305.8	335.7	345.7	385.6	432.8	477.7	517.5	557.4	572.4	661.9	691.9	754.1	868.7	948.4	1013.1		
VT122377	(m)	(m)	(vw)	(vw)	(w)	(w)	(m)	(m)	(sh)	(sh)	(s)	(sh)	(s)	(sh)	(vs)	(vw)	(vw)	(w)		
BD106434	233.6	248.6	303.4	338.2	370.1	385.5	430.4	455.3	472.6	475.2	542.4	664.5	746.7	883.6	928.5	965.8	1025.5			
Soda Spring	(m)	(sh)	(vw)	(w)	(w)	(w)	(w)	(m)	(sh)	(s)	(sh)	(vs)	(vw)	(vw)	(vw)	(vw)	(vw)	(vw)		
BD134924	216.2	246.1	258.0	300.9	333.2	353.2	373.1	388.0	432.9	465.2	510.1	554.9	661.9	736.7	906.0	970.8	1010.6	1030.0		
(w)	(m)	(w)	(w)	(w)	(vw)	(sh)	(w)	(m)	(vw)	(m)	(vw)	(sh)	(vs)	(vw)	(vw)	(vw)	(vw)	(vw)		
(vw)	(w)	(vw)	(vw)	(sh)	(w)	(m)	(vw)	(m)	(w)	(m)	(sh)	(sh)	(vs)	(vw)	(vw)	(vw)	(vw)	(vw)		
Lunar Crater	211.2	253.5	283.4	308.3	338.2	353.2	370.6	397.9	432.9	505.7	587.3	669.5	744.2	759.1	893.6	980.8	1013.0	1062.0		
(m)	(m)	(vw)	(w)	(vw)	(vw)	(vw)	(w)	(sh)	(sh)	(sh)	(s)	(sh)	(m)	(m)	(w)	(vw)	(vw)	(vw)		
X-202	216.2	251.1	298.4	333.3	378.1	432.9	502.6	592.2	781.6	843.7	903.6	950.9	995.7	1050.4						
(m)	(m)	(vw)	(vw)	(w)	(w)	(sh)	(vs)	(m)	(vw)	(vw)	(vw)	(vw)	(vw)	(vw)						
X-255	233.6	253.6	305.9	333.2	373.1	380.6	427.9	515.0	564.9	627.1	652.0	689.4	751.7	988.2						
(s)	(s)	(w)	(vw)	(vw)	(vw)	(vw)	(vw)	(sh)	(sh)	(sh)	(m)	(wsh)	(vs)	(vw)						
X-223	213.7	261.0	310.8	345.7	388.0	432.9	512.6	559.8	564.9	659.4	759.1	816.4	868.7	906.0	953.4	1008.1				
(s)	(s)	(w)	(vw)	(s)	(m)	(sh)	(s)	(s)	(m)	(s)	(s)	(sh)	(w)	(vw)	(vw)	(vw)	(vw)			
X-178	226.2	256.0	310.8	388.0	427.9	520.0	557.4	669.5	699.3	746.7	779.0	893.6	908.5	1013.0		1018.1				
(w)	(m)	(sh)	(s)	(sh)	(s)	(sh)	(vs)	(sh)	(vs)	(sh)	(vw)	(vw)	(vw)	(sh)						
X-146	213.7	228.7	261.0	281.0	308.3	333.3	350.7	373.1	427.9	512.5	547.4	572.3	662.0	694.4	756.6	901.1	968.3	1013.1		
(w)	(m)	(w)	(vw)	(vw)	(vw)	(vw)	(vw)	(vw)	(w)	(sh)	(s)	(m)	(sh)	(vs)	(vw)	(vw)	(vw)	(vw)		
M2	231.1	256.0	315.8	333.2	350.7	368.1	385.5	405.5	432.9	575.0	547.4	567.3	679.4	751.6	898.6	968.3	1028.0			
(sh)	(vw)	(vw)	(vw)	(vw)	(vw)	(vw)	(vw)	(m)	(sh)	(s)	(sh)	(sh)	(vs)	(vw)	(vw)	(vw)	(vw)			
X-176	261.0	315.8	340.7	373.1	388.0	435.4	510.1	537.5	562.4	612.2	659.5	676.9	751.6	906.1	958.3	1000.6				
(w)	(vw)	(vw)	(vw)	(vw)	(m)	(wsh)	(vw)	(w)	(vw)	(w)	(vw)	(vw)	(vs)	(vw)	(vw)	(vw)	(vw)			
X-17	221.2	256.0	308.3	338.2	375.6	385.5	430.4	515.0	559.9	572.3	589.8	669.5	759.1	901.1	943.4	1018.1				
(w)	(m)	(w)	(vw)	(wsh)	(vw)	(m)	(sh)	(vw)	(s)	(s)	(vs)	(vs)	(vs)	(vw)	(vw)	(vw)				
Salt Lake	258.5	305.8	338.2	375.6	388.0	432.8	515.0	557.4	677.0	741.7	886.1	960.8	1013.0							
(w)	(vw)	(vw)	(vw)	(vw)	(m)	(m)	(m)	(sh)	(vs)	(vw)	(vw)	(vw)	(vw)							
Peridot Mesa	218.7	263.5	313.3	343.2	363.1	388.0	435.4	520.0	559.9	627.1	676.9	744.2	891.1	948.4	1010.6					
(m)	(m)	(vw)	(vw)	(vw)	(w)	(m)	(m)	(m)	(wsh)	(sh)	(vs)	(vw)	(vw)	(vw)						

Description of abbreviation: vw = very weak; w = weak; m = medium; wsh = weak shoulder; sh = shoulder; s = strong; vs = very strong

difficult to qualitatively analyze the nature of the cation distribution and its effect on the crystal structure through the spectroscopic data.

The high-frequency bands ($3000\text{-}4000\text{ cm}^{-1}$) are the result of the stretching vibrations of hydroxyl ions. In the case of pure liquid water three internal vibrational bands are expected: two bands in the $3000\text{-}4000\text{ cm}^{-1}$ region, and one band near 1600 cm^{-1} . The band $\sim 1600\text{ cm}^{-1}$ originates from the H-O-H bending v_2 mode. The broad feature near 3400 cm^{-1} (Aines and Rossman, 1984) is due to the overlap of the symmetrical stretch, v_1 mode, (3250 cm^{-1}) and anti-symmetric stretch, v_3 mode, (3420 cm^{-1}) of H-O-H bonds (Fig. 74). But, in minerals containing hydroxyls, the stretching mode appears near or above 3600 cm^{-1} because of the absence of hydrogen bonding in the crystal structure. The interaction of cations with the hydrogen shortens the OH- bond and thus the vibrational frequency increases.

In the spectrum of cummingtonite and actinolite, several distinctive bands are observed in the OH- stretching region (Fig. 75). For example, in cummingtonite, up to four sharp bands at 3667 , 3653 , 3637 , and 3619 cm^{-1} are clearly observed (Fig. 76). Wang et al. (1988) curve fitted the spectral features, demonstrated the presence of five O-H bands in their spectra, and assigned the major bands to the occupations of the divalent cations and the final one to the occupation of trivalent iron. The curve fitting results of our present cummingtonite sample suggests that there are at least six bands in this spectra. Even though ideally cummingtonite is a magnesium-containing mineral, microprobe analysis reveals that the present sample contains several other cations including calcium ($\text{CaO}=12\text{ wt\%}$) and iron ($\text{FeO} = 4.46\text{ wt\%}$).

The presence of a second cation in structural sites of amphiboles and its effect on vibrational spectra (IR spectra) has been demonstrated by Burns and Sterns (1966). Factor group analysis by Wang, et al., (1988) predicts up to 8, 20, and 42 bands in the hydroxyl region for binary, ternary, and quaternary system respectively. Termolite, a

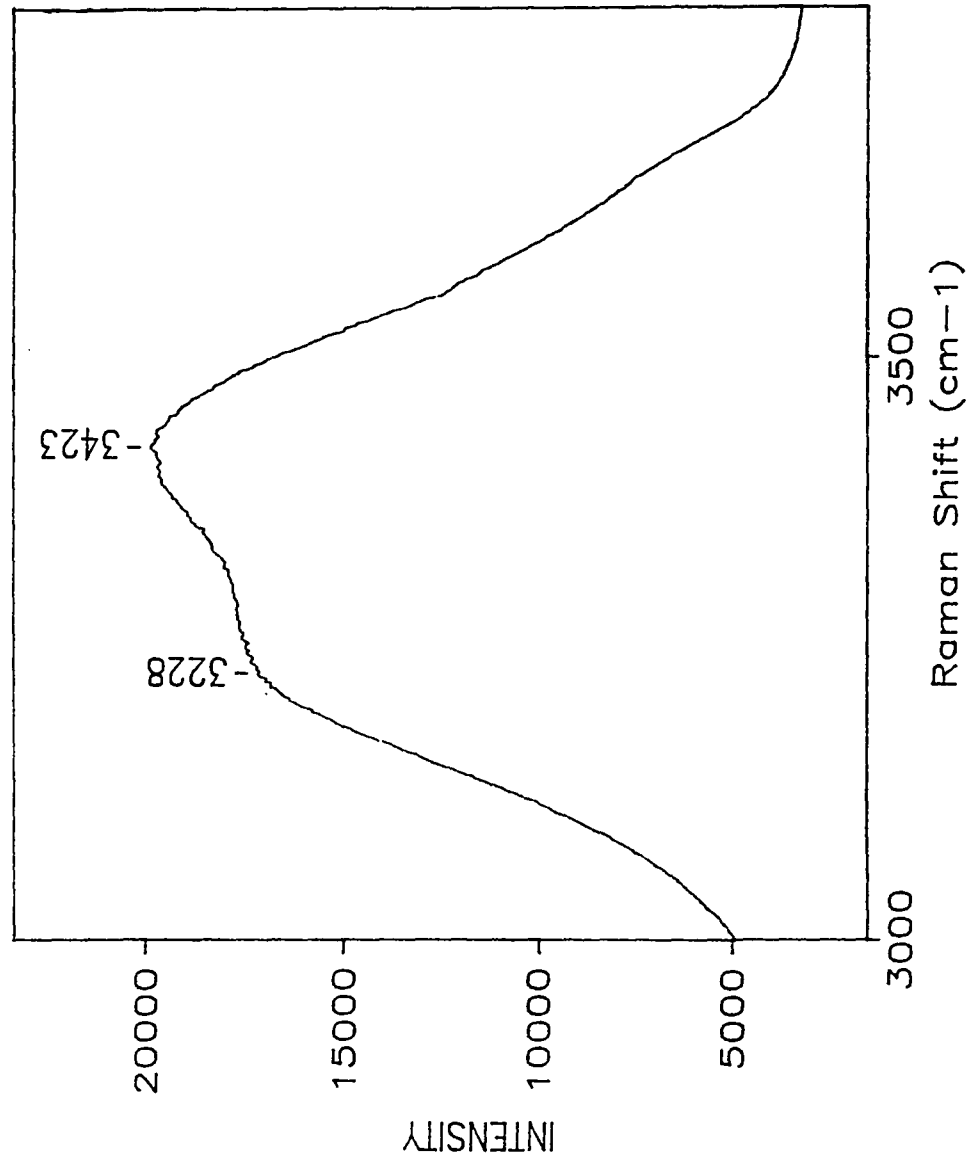


Figure 74: Raman spectra of water at room temperature

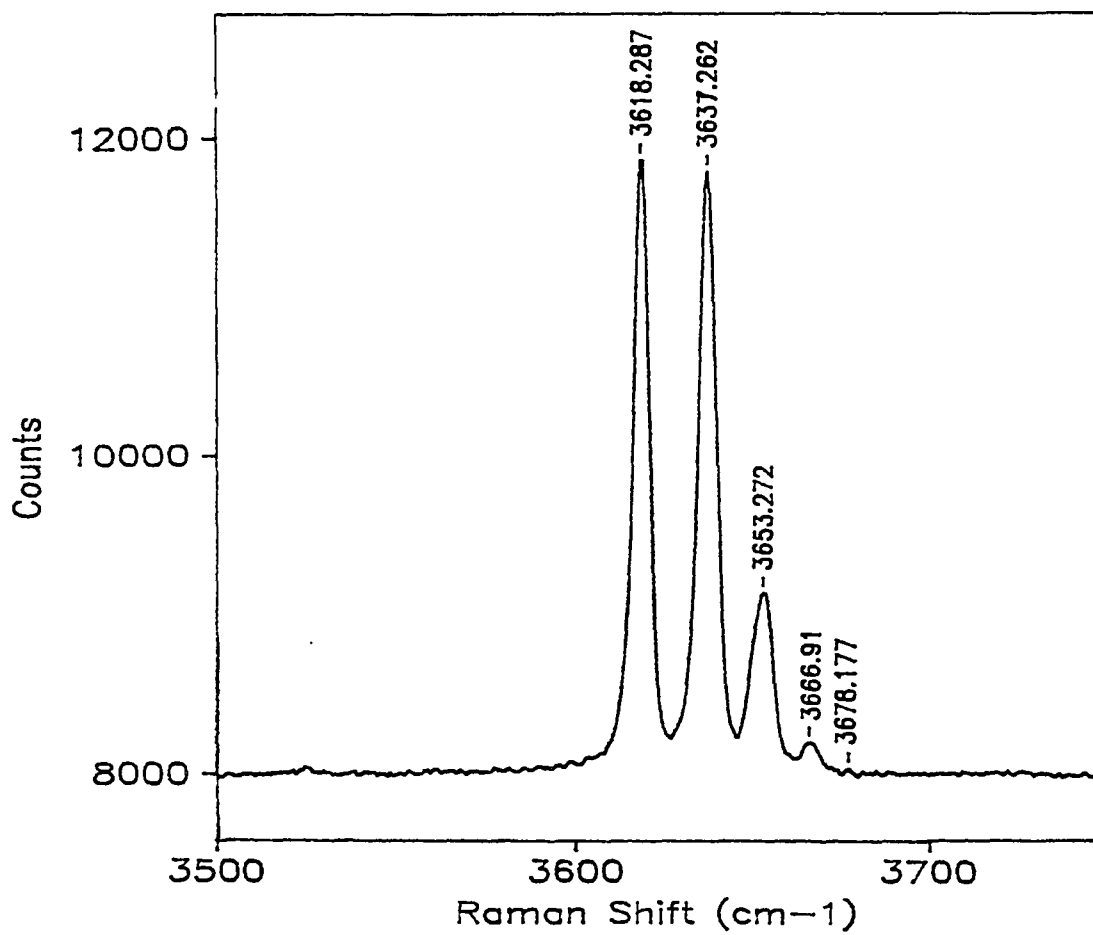


Figure 75. The hydroxyl stretching vibrations in cummingtonite crystal.
Up to four bands are clearly visible.

154

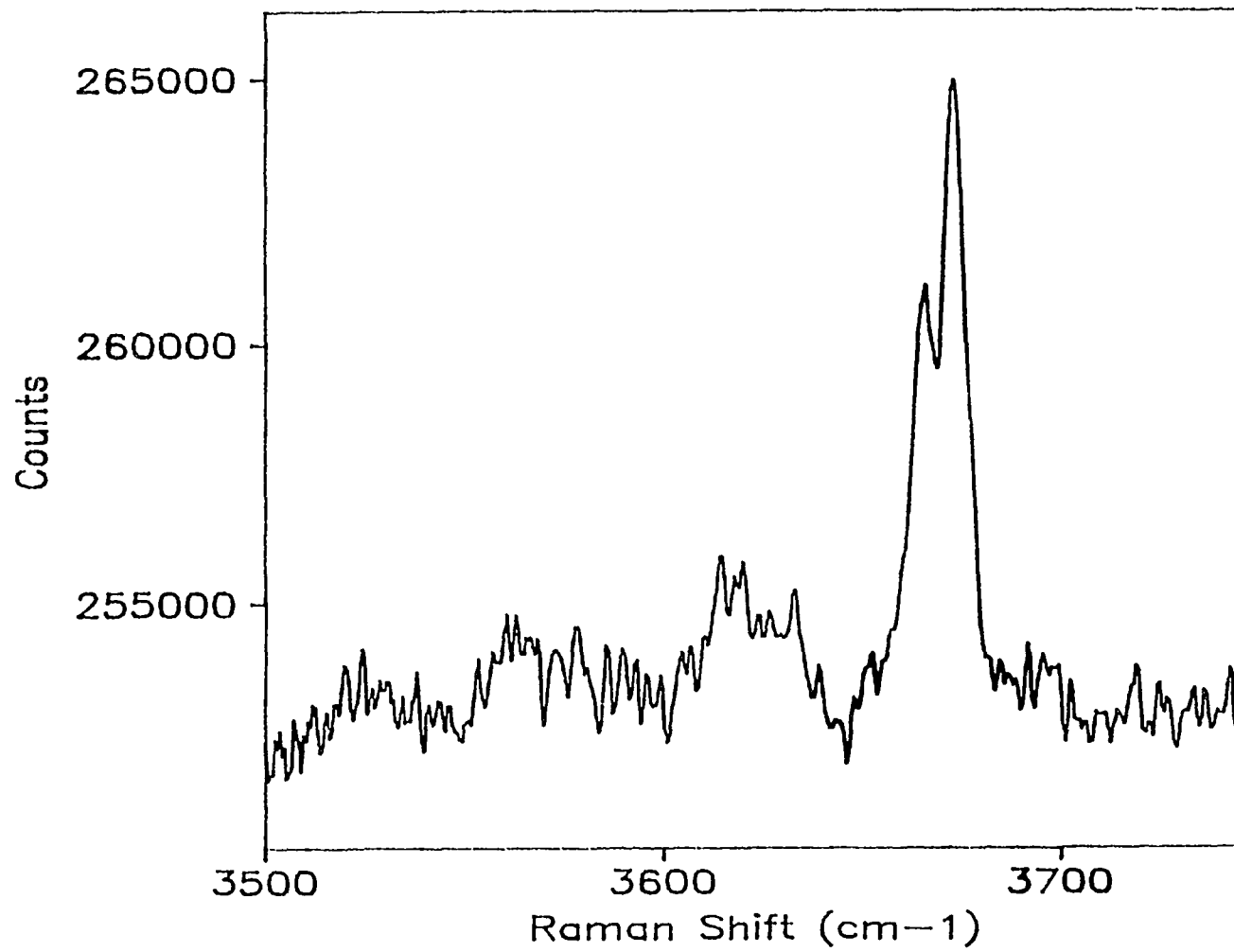


Figure 76. Raman spectra of termolite at room temperature. The peak at 3672 cm^{-1} is known as the termolite band.

magnesium containing amphibole, has one strong peak around 3672 cm⁻¹ and one small shoulder, indicating the presence of some iron (Fig. 76). Thus, the complexity in the spectrum of amphiboles increases with the number of cations present in the crystal.

Figure 77 shows the Raman spectra of six amphibole crystals in the frequency range 3500-3750 cm⁻¹. As mentioned earlier, it is extremely difficult to obtain a good Raman spectrum in the hydroxyl stretching regions even with a state-of-the-art spectrometer setup. All of the amphibole crystals measured have broad bands in comparison to the individual sharp bands in cummingtonite or actinolite. However, it is found that the intensity of this broad band decreases with decreasing OH⁻ content in the sample. Sample VT 122377 has the highest water content (H₂O = 1.578 wt%) and thus, the strongest Raman band. Lunar Crater sample has only 0.487 wt% water and the Raman band is not visible in this spectra. Therefore, with the present experimental setup (see chapter 2), detection limit on the hydroxyl band in amphibole is about 0.5 wt%. A plot of the observed Raman frequency vs MgO and FeO content in wt% shows that the Raman band decreases with FeO wt% and increases with MgO wt% (Fig. 78). This is in agreement with the observation of Burns and Sterns (1966) observation. However, the present data set shows a large scatter from a linear fit. This could be attributed to two factors: 1) the dependency of the Raman frequency on compositional elements other than Mg and Fe (the effect of cations such as K⁺ or Na⁺ is not well understood at the present time). 2) Statistical error in the experimental measurements (the resolution of the instrument was only 4 cm⁻¹).

The broad band is approximately 70 cm⁻¹ wide. An attempt was made to resolve the peaks into various components. But, without knowing the cation occupancy in various structural sites it is difficult to assess the total number of bands and their positions.

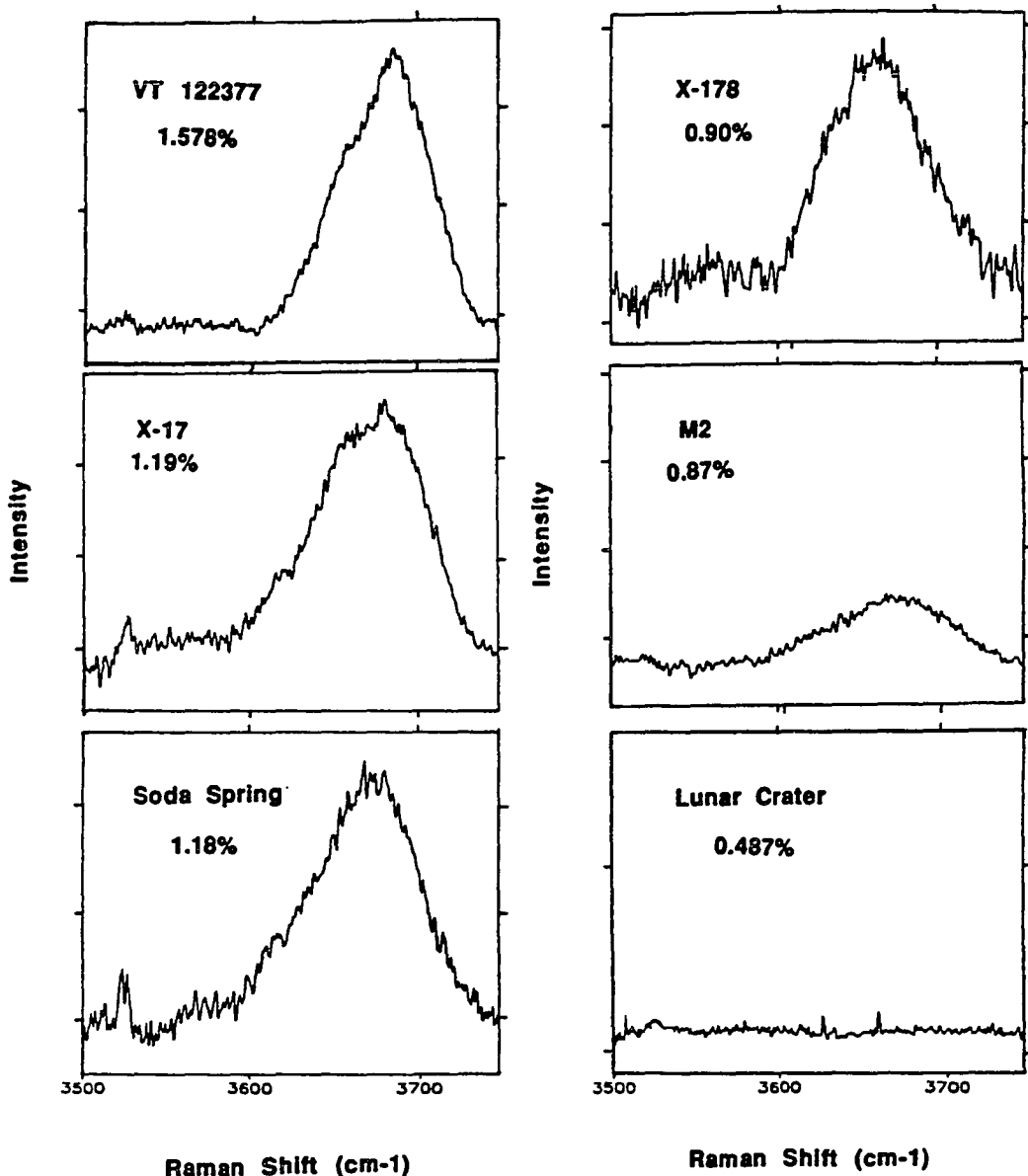


Figure 77. The hydroxyl stretching vibrations in Ti-rich amphibole

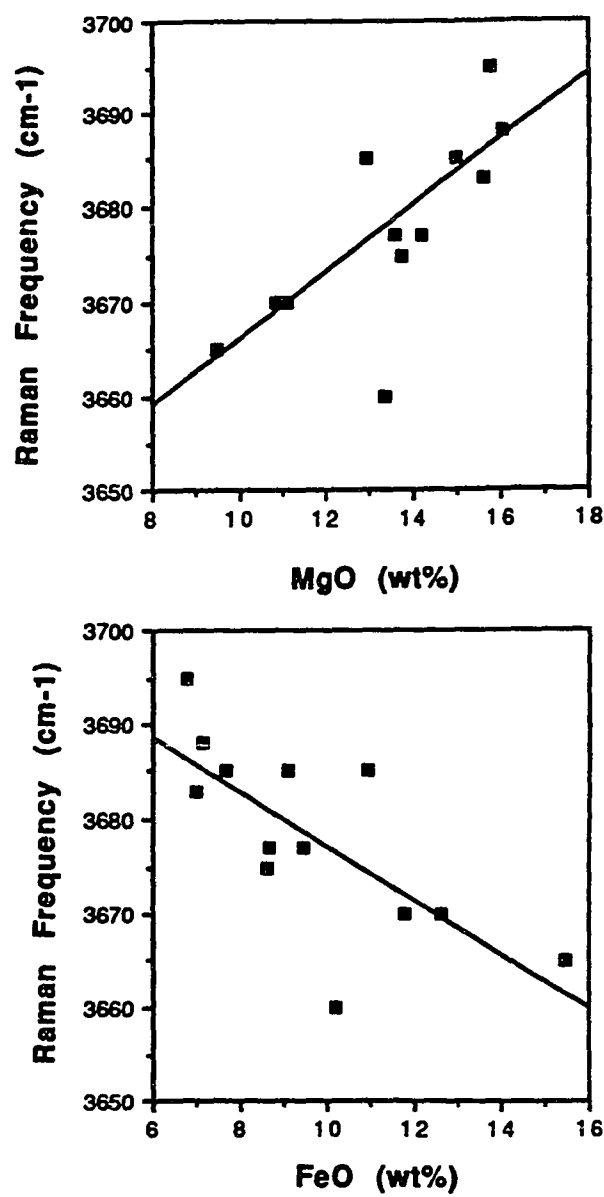


Figure 78. Variation of Raman frequency with MgO (wt%) and FeO (wt%).

5.4.2 Infrared spectra of amphibole crystals

Infrared spectra of the amphibole samples in the 3500-3800 cm⁻¹ region are given in Fig. 79. As in the Raman spectra, all of the amphibole samples give a broad band in the OH⁻ stretching region. Samples VT 122377 and X-223 show clearly the presence of doublets. Once again, the peak of the IR bands also show an increase in wavenumbers with increasing MgO and decreasing FeO content.

The hydroxyl stretching and hence its vibrational frequency is influenced by its nearest neighbors. The hydroxyl is located in the O₃ site and it is surrounded by nearest neighbors M₁, M₃, and A sites. A site is occupied by large alkali cations, such as K⁺, Na⁺, and sometimes left vacant. Variation of infrared frequency in the OH⁻ region for natural and synthetic samples has been discussed by several authors (Ventura, et al., 1991, Burns and Sterns, 1966). The variation of the frequency is attributed to factors such as a) cation substitution in the M₁ and M₃ sites; b) the presence of cations in the A site, and the physical properties, such as charge and size, of the cation that enters into these sites; c) the site location A(m) or A(2/m); and d) the occupancy of other volatiles such as F⁻ and Cl⁻. A single band that appears at 3673 cm⁻¹ in the Mg containing amphibole, termolite, is termed a termolite-type band (Fig. 80) and it originates from the vibrations of MgMgMg-OH⁻ configuration. In grunerite, all the sites are occupied by Fe²⁺, and consequently, a single band appears around 3615 cm⁻¹. Between the end member compositions, with a combination of Mg and Fe cations, IR spectra shows up to four bands (Fig. 80). Their frequency and intensity varies linearly with the composition. The variation of the IR frequency against FeO and MgO content is plotted in Fig. 81. The effect of cation substitution on the vibrational frequency is very clear from the above data.

In amphiboles, the A-site is very large and it is usually ten- to twelve-coordinated. It is occupied by large cations such as K⁺ and Na⁺. In some cases it is left

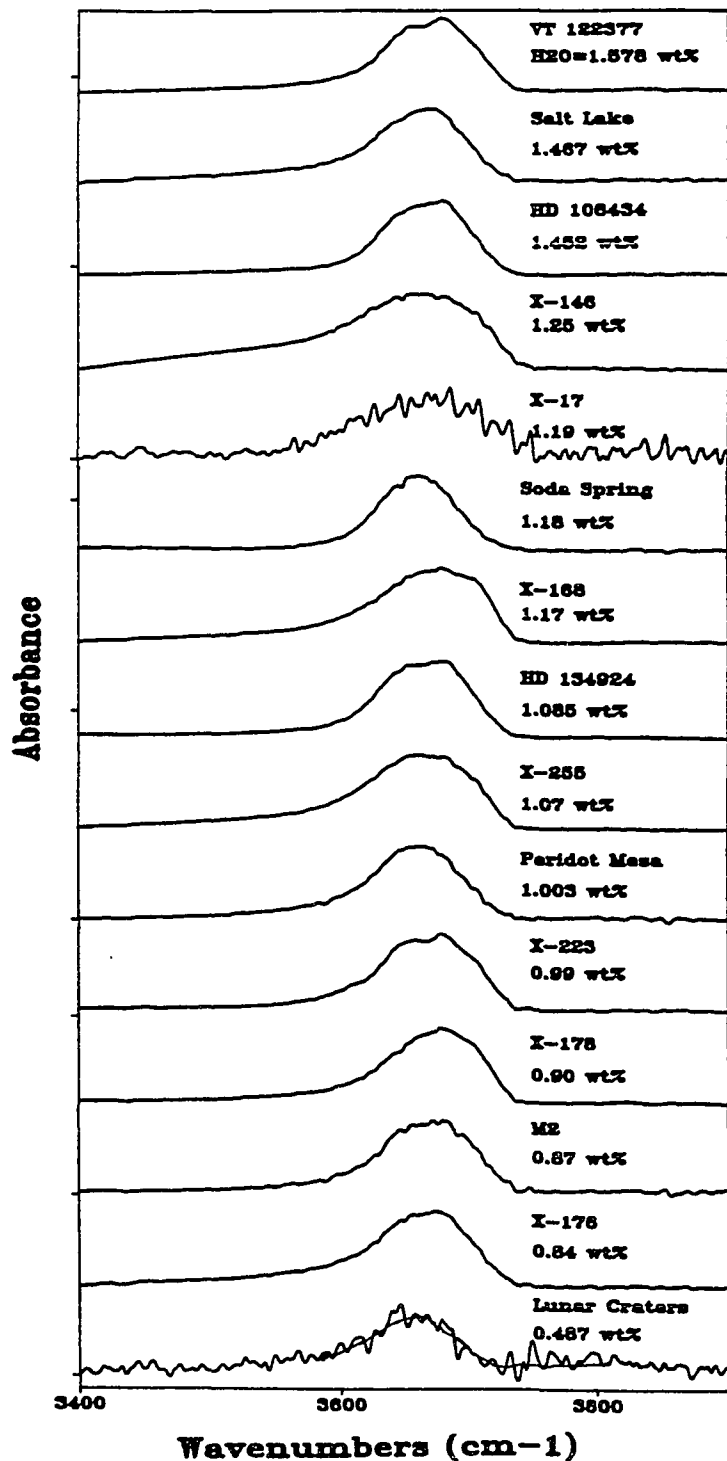


Figure 79. Infrared spectra of amphibole crystals in the hydroxyl region.

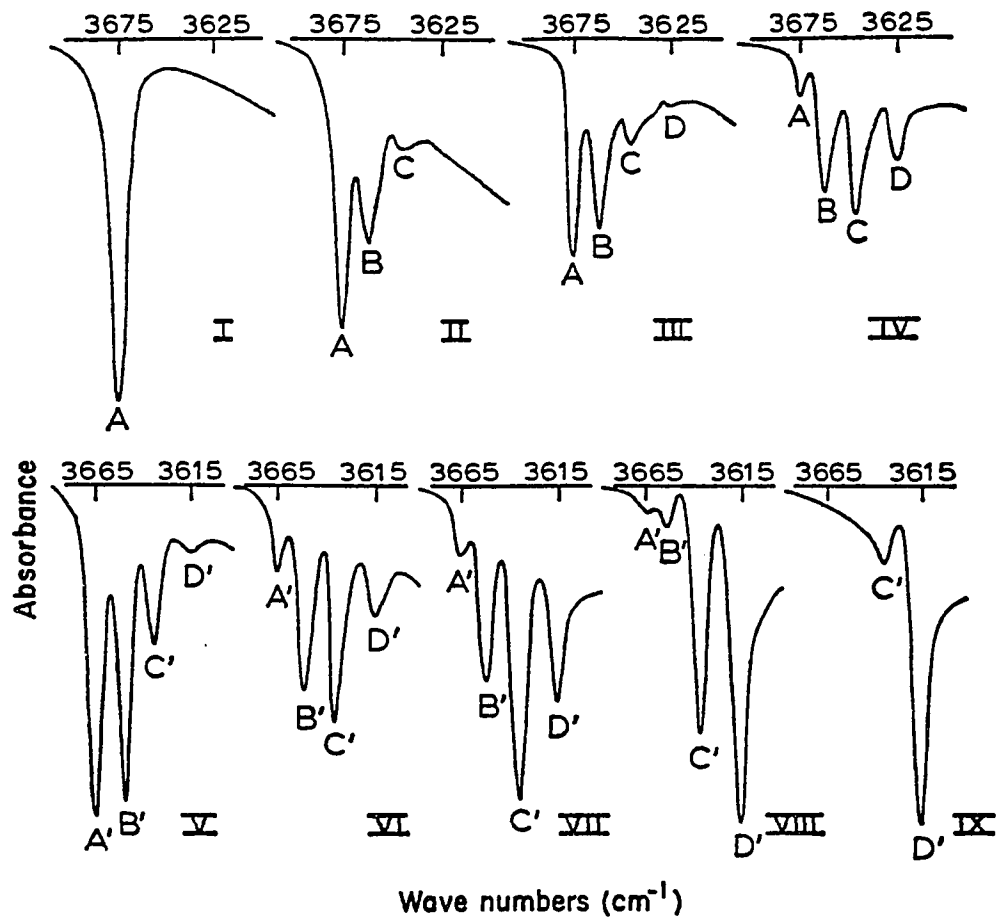


Figure 80. Infrared spectra of fundamental stretching bands in termolite-ferroactinolite and cummingtonite-grunerite series. The number of peaks and its intensity is a strong function of composition (after Burns and Sterns, 1966).

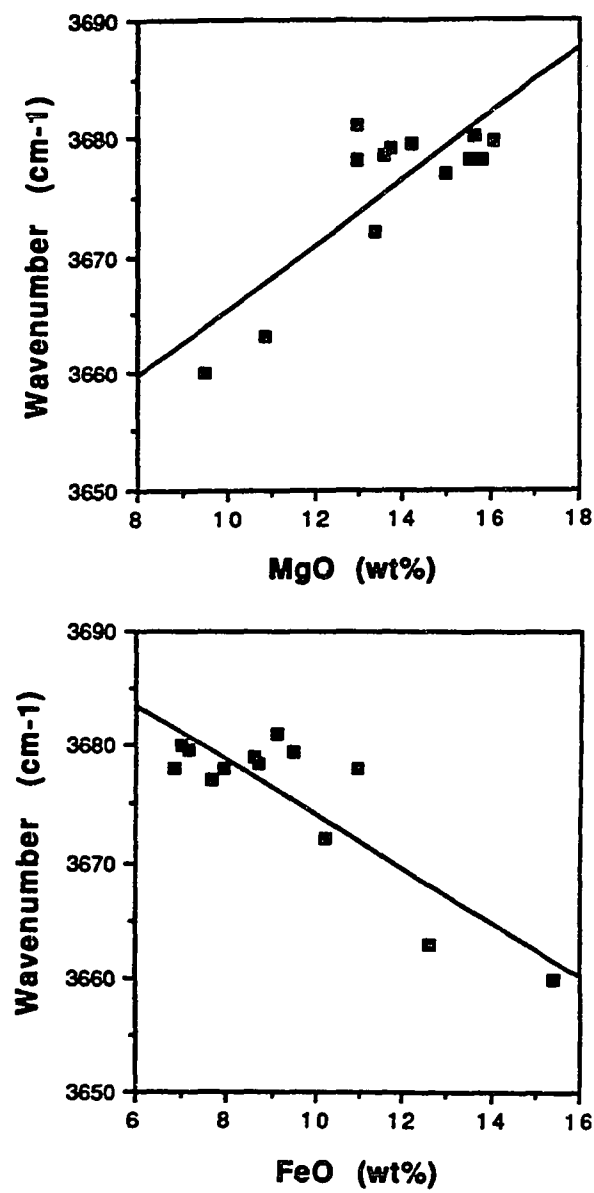


Figure 81. IR frequency also varies with the MgO and FeO content in the amphibole crystals.

vacant. Looking from the O₃ site the OH⁻ vector points towards A-site. The presence of large cations repel the hydrogen, resulting in shortening of the OH⁻ bond and consequently the vibrational frequency goes up. The effect of the A-site on the vibrational frequency is quite appreciable. In potassium- and sodium-richerite it has been shown that the termolite-type band at 3673 cm⁻¹ in the presence of cations in the A-site could increase the frequency to 3735 cm⁻¹ for K⁺ ions and 3730 cm⁻¹ for Na⁺ ions. Moreover, the frequency difference of up to 5 cm⁻¹ has been observed in the A(m) and A(2/m) configuration (Ventura, et al., 1991). Finally, it is found that systematic substitution of fluorine in K⁺ and Na⁺ richerite decreases the OH⁻ stretching frequency.

The stretching frequencies of the hydroxyl in most of the amphibole samples show a broad peak centered about 3670 cm⁻¹. Similar to Raman results, the ir frequency of these samples also shows an increase in the vibrational frequency with MgO content. The width of these bands is about 80 cm⁻¹, even though some samples have a full width to about 120 cm⁻¹. The great width of the bands could be explained as follows: most of the peak is centered around the termolite-type band, which is due to the magnesium in the structure. For more iron-rich samples the peak shift is towards the lower end of the frequency spectrum. The presence of large cations (K⁺ or Na⁺) in the A(m) or A(2/m) sites affects the high frequency. Thus, the vibrational frequency spreads from 3620 cm⁻¹ to 3735 cm⁻¹, resulting in a broad band. It is difficult to determine the contribution of each component to the resulting envelope. The initial results from our high-pressure and low-temperature measurements of the hydroxyl stretching region in the amphibole crystal suggest that the OH⁻ resides in a large site. They also suggest that the changes in the crystallographic volume do not appreciably affect the OH⁻ bonding (see the following sections).

The cummingtonite sample was chosen for the high-pressure experiments for the following three reasons: a) cummingtonite gives a very strong spectra in the low-frequency as well as in the hydroxyl stretching region; b) cummingtonite has a simpler chemical composition than other amphibole crystals; and c) high pressure data for cummingtonite does not exist at present time. Spectra in the low-frequency and high-frequency region are measured separately. In the 100-1300 cm⁻¹ region the spectra were measured up to 320 kbars (Fig. 82). The intensity of the hydroxyl bands, however, decreases rapidly with increasing pressure, so spectra in the OH region above 137 kbar were difficult to detect (Fig. 83).

A plot of observed Raman frequency vs applied pressure shows a linear relation to the applied pressure. The high-frequency band at 1022 cm⁻¹ originating from the symmetric stretch of the Si-O⁻ bonds shows a steeper slope, indicating shortening of the bond length. High-pressure experiments on silicate minerals suggest that the SiO₄ tetrahedra remains intact up to 320 kbar.

In cummingtonite, at ambient conditions, four hydroxyl stretching bands are clearly observed. At high-pressure only two bands are distinctive, and therefore only two bands are used for the data analysis. The bands at 3636 cm⁻¹ and 3617 cm⁻¹ show that the frequency of the OH band increases with pressure up to 60 kbar and then levels off (Fig. 84). Above 110 kbar, its frequency decreases. The increase in the Raman frequency indicates that with increasing pressure the structure become more compact and the distance from the hydroxyl to the cations in M1 and M3 sites decreases. This will decrease the OH⁻ bond length and results in higher vibrational frequency. The plateau in the curve above 60 kbar could represent the limit on incompressibility of the structure. Finally, the decrease in the final data point could be due to an artifact

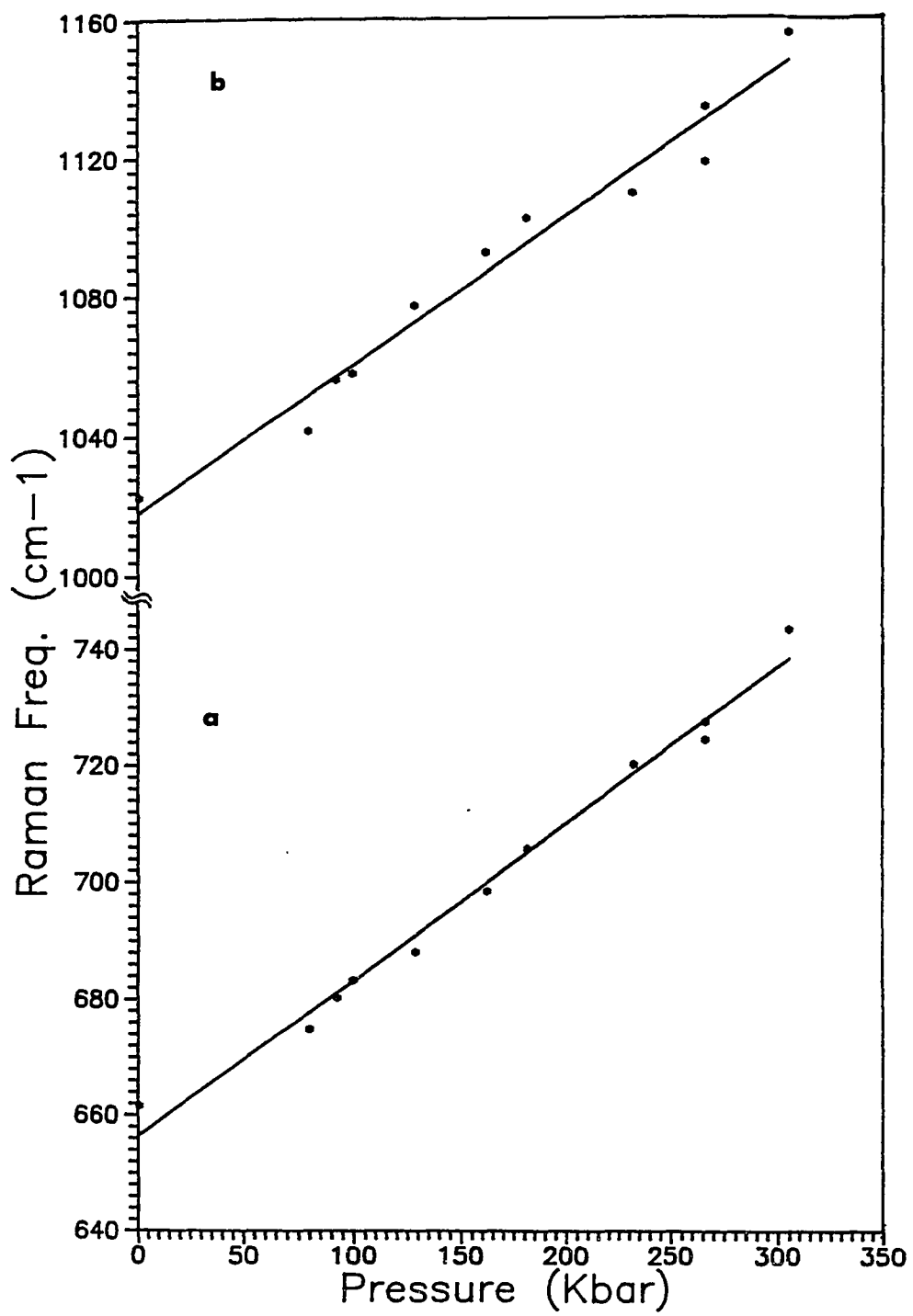


Figure 82. A plot of symmetric stretching band (a) and anti-symmetric stretching band (b) in cummingtonite with increasing pressure.

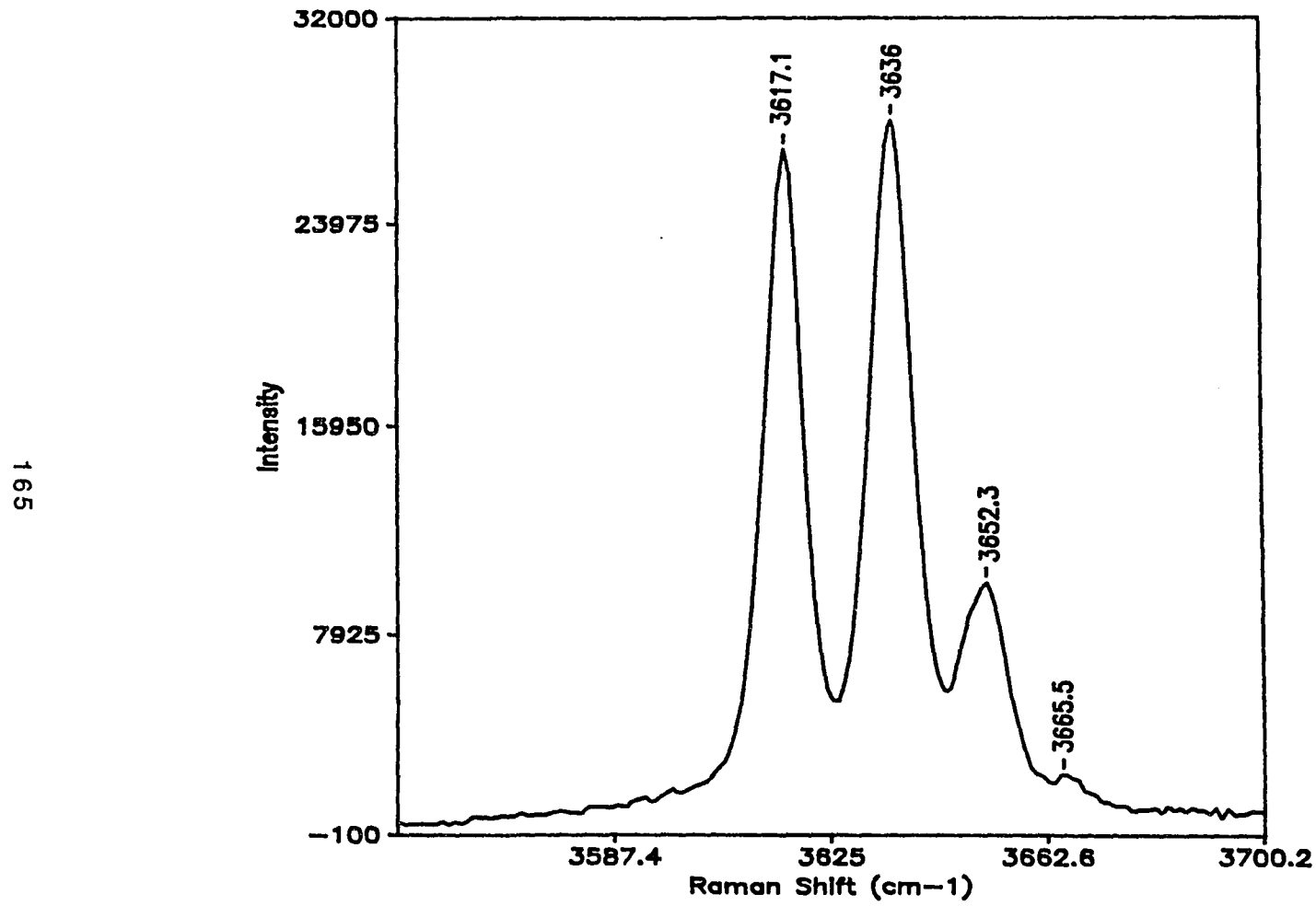


Figure 83. High-pressure Raman spectra of cummingtonite in the hydroxyl region.

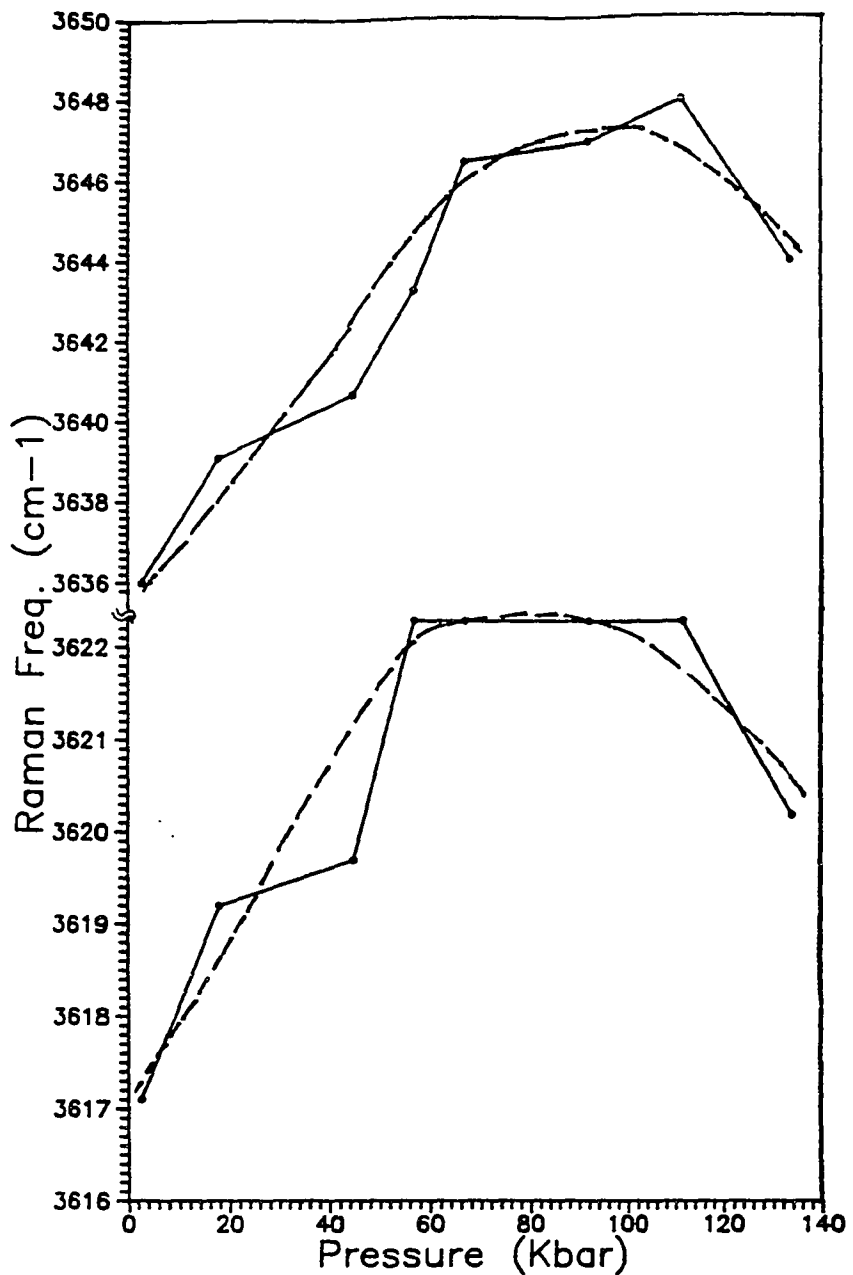


Figure 84. The behavior of hydroxyl stretching bands at 3617 cm^{-1} and 3636 cm^{-1} bands of cummingtonite with applied pressure.

resulting from the poor spectra. The increase in the hydroxyl frequency with applied pressure indicates that OH⁻ resides in a large site. The presence of such a large site easily helps to accommodate different size cations into the structural sites.

5.6 Suggestions for future work

Compared to other silicate minerals, amphiboles have complex crystal structures. It contains several cations in the crystallographic sites, and all of them vary in size and can be occupied by a wide range of cations. Therefore, a study of natural samples will be very difficult. In order to understand the effect of various crystallographic sites, their cation occupancies, and its effect on the crystal structure as a whole, a systematic compositional study is needed (ex. Ventura, et al., 1991). Finally, the observation by Wang, et al., (1988) on the increase in the hydroxyl frequency with decreasing temperature needs to be verified.

APPENDIX

Alignment of the micro-Raman spectrometer

The spectrometer along with the microscope has been properly aligned for the reception of weak scattered Raman signal and has been bolted down to avoid any physical movement during at any time of the experiment. Raman signal is very weak and it is extremely important that the laser beam, microscope and the spectrometer is in perfect alignment with each other. But in the event of any misalignment the following steps have to be performed to set the spectrometer for its best operation before any data collection.

Step 1. The laser beam from the laser has to be perfectly horizontal or parallel with the laser tube. This can be achieved by measuring the height of the beam from the ground using a meter scale at the laser head and the farthest point possible. The beam height can be adjusted by the four leveling screws on which the laser sits.

Step 2. The beam is then passed through the pre-monochromator to eliminate all the plasma lines from the laser. A light power meter is held at the output end of the pre-monochromator and pre-monochromator is tuned for maximum power. This will ensure plasma free laser beam. Finally, laser beam can be focused for parallel beam by focusing the out put beam at infinity using a convex lens.

Step 3. Using prisms and mirrors the laser beam from the pre-monochromator is directed towards the microscope. Prisms and mirrors are mounted on mounts with two degrees (X and Y) of freedom. At the microscope stage, the beam is scattered from the sample at two different geometries, 135 degrees (oblique) and 180 degrees (back scattering) with respect to the to the axis of the microscope. The initial alignment procedure has to done with 180 degree scattering geometry for the best results. 180

degree scattering geometry is necessary to ensure the parallelism between laser beam and microscope axis. After the initial alignment of the laser beam at the laser head (for the horizontality of the beam), the beam is tested for its horizontality after the addition of each optical component.

Step 4. The most important part of the optical alignment is at the microscope. It can be very tedious, time consuming and frustrating. At times, out of pure luck, perfect alignment is achieved in no time! However, the following procedure is taken to ensure good alignment of the at the microscope.

- a) 180 degree scattering geometry is selected for the alignment, because it ensure that the microscope is parallel with the laser beam.
- b) For 180 degree scattering geometry the beam spliter is inserted in to the given slot. It is then rotated through approximately 45 degree with the incident laser beam. It is made sure that the first reflection surface is facing the incoming beam. When the beam spliter is at the proper angle an intense laser beam is observed on a glass slide placed on the microscope stage. It is advised to take the microscope objective from its holder, to make sure that the incoming beam is not touching any parts of the microscope. With the microscope objective in its holder it is often difficult to check this.
- c) At this point the microscope objective is put back into its holder and the laser beam is focused on to the glass slide by moving the microscope stage up and down. If all the previous step has been performed carefully one should get a single and small laser focus with concentric ring (Newton's rings) around it. On moving the stage up and down more Newton's rings emerge from (or collapse into) the focus. Instead, upon moving the stage up and down, if two different focus moving in two different directions are observed with out concentric rings, it means that the alignment is not perfect.

d) From here on, to get good alignment only minute adjustments on the prisms, mirrors, or the beam splitter has to be performed. First, the movement of the spots are carefully studied by turning the X or Y screws of the prisms or mirrors by a small amount. Raise the microscope stage from the lowest point and bring the first laser focus into view on the glass slide. Now adjust the X or Y screw of one optical component (preferably a prism) so that the patch or halo of light (second focus) encircle the first focus. An image of the focus and the light around it can be seen on a piece of paper held in front of the entrance slit of the spectrometer. Now, the main focus might change little bit which can be brought back into view by adjusting the beam splitter. By going back and forth between the beam splitter and the prisms one can achieve the best laser focus and Newton's ring.

e) Step d is confusing, pain taking and frustrating. But, if above steps can be performed with one more person, especially when different optical components are across the table, it will make the alignment procedure very easy.

f) A video camera is mounted on to the microscope stage before the entrance slit of the spectrometer. The image of the sample can be viewed on this either in transmitted or reflected light mode. Using the same system, the image of the laser focus can be viewed.

REFERENCES

- Adams, D.M., Sharma, S.K., and Appleby, R. (1977) Spectroscopy at very high pressures 14: Laser Raman scattering in ultrasmall samples in a diamond anvil cell. *Applied optics*, 16, no.9, 2572-2575.
- Adams, G. E. and Bishop, F. C. (1982) Experimental investigation of Ca-Mg exchange between olivine, orthopyroxene, and clinopyroxene: potential for geobarometry. *Earth and Planetary Science Letters*, Vol. 57, pp 241-250.
- Adams, G.E. and Bishop, F.C. (1985) An experimental investigation of thermodynamic mixing properties and unit cell parameters of forsterite-monticellite solid solutions. *American Mineralogist*, 70, 714-722.
- Aines, R. D., and Rossman, G.R. (1984) Water in minerals: A peak in the infrared. *Journal of Geophysical Research*, 89, no.B6, 4059-4071.
- Akamatsu, T., Fujino, K. K., M., Fujimura, A., Kato, M., Sawamoto, H., and Yamanaka, T. (1988) Pressure and temperature dependence of cation distribution in Mg-Mn Olivine. *Phys Chem Minerals*, 16, 105-113.
- Bancroft, G. M. (1973) *Mossbauer Spectroscopy: An introduction for inorganic chemists and Geochemists*. Halstad Press, New York.
- Barr, G. M. (1962) *Introduction to molecular spectroscopy*. Chapter 2 and Chapter 4. McGraw-Hill, New York.
- Bassett, W. A., and Ming, L-C., (1972) Disproportionation of Fe₂SiO₄ to 2FeO+SiO₂ at pressures up to 250 kbar and temperatures up to 3000 C. *Phys. Earth Planet. Interiors* 6, 154-160.
- Besson, J.M., Pinceaux, J.P., and Anastopoulos, C. (1982) Raman spectra of olivine up to 65 kilobars. *J. Geo. Res.*, 87, no.B13, 773-775.
- Bigger, G. M. and O'Hara, M. J. (1969) Monticellite and forsterite crystalline solutions. *Journal of the American Ceramic Society*, 52, No. 5, 249-252.
- Bismayer, U. (1988) New developments in Raman spectroscopy on structural phase transitions. In *Physical properties and thermodynamic behavior of minerals*, ed. by Ekhard K. H. Salje., pp 143-181. D. Reidel Publishing Company, Dordrecht.
- Blaha J. J., Rosasco, G. J. (1978) Raman Microprobe Spectra of Individual Microcrystals and Fibers of Talc, Termolite and Related Silicate Minerals. *Analytical Chemistry* 50, No.7:892-896
- Brown, G. E. (1982) Olivines and silicate spinels. In P.H. Ribble Ed., *Orthosilicates, Reviews in Mineralogy*, Volume 5, Mineralogical Society of America, 275-381.

- Brown, G. E. and Prewitt, C. T. (1973) High temperature crystal chemistry of hortonolite. *American Mineralogist*. Vol. 58, pp 577-587.
- Buijs, H. (1989) Fourier transform Raman Spectroscopy -- an overview. *Spectroscopy*, 1, no.8.
- Burns, R. G. and Sterns, R. G. J. (1966) Infrared study of hydroxyl bands in clino amphiboles. *Science*, vol. 153, pp 890-892.
- Burns, R.G. and Huggins, F.E. (1972) Cation determinative curves for Mg-Fe-Mn olivines from vibrational spectra. *American Mineralogist*, 57, 967-985.
- Cameron, M. and Papike, J. J. (1980) Crystal chemistry of silicate pyroxenes. Chapter 2 in *Reviews in Mineralogy*, Vol. 7, Pyroxenes, Ed. by Charles T. Prewitt, Mineralogical Society of America, 5-92.
- Cameron, M., Sueno, S., Prewitt, C.T., and Papike, J.J. (1973) High-temperature crystal chemistry of acmite, diopside, hedenbergite, jadeite, spodumene, and ureyite. *American Mineralogist*, 58, 594-618.
- Chopelas, A. (1991) Single crystal Raman spectra of forsterite, fayalite and monticellite. *American Mineralogist*, 76, 1101-1109.
- Colthup, N. B., Daly, L. H., and Wiberley, S. E. (1964) Introduction to infrared and Raman spectroscopy. Chapter 1 and Chapter 2. Academic Press New York and London.
- Cooney, F.T. and Sharma, S.K. (1990) Structure of glasses in the systems Mg_2SiO_4 - Fe_2SiO_4 , Mn_2SiO_4 - Fe_2SiO_4 , Mg_2SiO_4 - $CaMgSiO_4$, Mn_2SiO_4 - $CaMnSiO_4$. *Journal of Non-crystalline Solids*.
- Deer, W. A., Howie, R. A., and Zussman, J. (1978) Rock-Forming Minerals. Volume 2A. Single-Chain Silicates: Pyroxenes. Second edition. A Halsted Press Book. John Wiley & Sons, New York, 3 -544.
- Docka, J. A., Post, J. E., Bish, D. L., and Burnham, C. W. (1987) Positional disorder of A-site cations in C2/M amphiboles: Model energy calculations and probability studies. *American Mineralogist*, 72, 949-958.
- Etchepare, J. (1972) Study by Raman Spectroscopy of crystalline and glassy diopside. *Amorphous Materials*, Douglas, R.W. and Ellis, B., eds., John Wiley and Sons, 337-346.
- Fadini, A. and Schnepel, F-M. (1989) Vibrational spectroscopy: methods and applications. Ellis Horwood series in analytical chemistry. John Wiley & Sons, New York.
- Farmer, V. C. (1974) The Infrared spectra of Minerals. Chapter 14. Mineralogical Society Monograph, 41 Queen's Gate, London, SW7 5HR, 4, 305-330.

- Finger, L. W. and Ohashi, Y. (1976) The thermal expansion of diopside to 800C and a refinement of the crystal structure at 700 C. *American Mineralogist*, 61, 303-310.
- Garcia, M. O., Muenow, D. W., Liu, N. W.K. (1980) Volatiles in Ti-rich amphibole megacrysts, southwest USA. *Am Mineral* 65, 306-312.
- Gardine, D. J. and Graves, P. R. (1989) Practical Raman Spectroscopy. Springer-Verlag.
- Gervais, F., Piriou, B., and Cabannes, F. (1973) Anharmonicity of infrared vibration modes in the Nesosilicate Be_2SiO_4 . *Phys. stat. sol.* 55, 143-154.
- Gillet, Ph., Reynard, B., Tequi, C. (1989) Thermodynamic properties of Gauophane new data from calorimetric and spectroscopic measurements. *Phys Chem Minerals* 16:659-667
- Graham, E.K. (1986) Recent developments in conventional high-pressure methods. *J. Geo. Research*, 91, no. B5, 4630-4642.
- Grasselli, J. G., Snavely, M. K., and Bulkin, B. J. (1981). Chemical Applications of Raman Spectroscopy. Chapter 1 and 2. John Wiley & Sons, New York.
- Green II, H. W. (1984) How and why does olivine transform to spinel? *Geophysical Research Letters*, 1,no.9, 817-820.
- Hawtharone, F. C. (1983) Quantitative characterization of site occupancies in minerals. *American Mineralogist*, 68, 287-306.
- Hawthorne, F. C. (1981) Amphiboles and other hydrous pyribiles-mineralogy. Chapter 1 and 2 in *Reviews in Mineralogy Volume 9A*, Ed. by David R. Veblen. Page 1-139. Mineralogical Society of America.
- Hazen, R. M. (1976) Effects of temperature and pressure on the crystal structure of forsterite. *American Mineralogist*. Vol. 61, pp 1280-1293.
- Hazen, R. M. and Finger, L. W. (1982) Comparative crystal chemistry, Wiley-Interscience, New York, 231.
- Hazen, R.M., and Prewitt, C.T. (1977) Effects of temperature and pressure on interatomic distances in oxygen-based minerals. *American Mineralogist*, 62, 309-315.
- Hemley, R. J., Bell, P. M., and MAo, H. K. (1987) Laser techniques in high-pressure geophysics. *Science*, vol 237, 605-612.
- Hemley, R. J., and Kubicki, J. D. (1991) Deep mantle melting. *Nature*, 349, 283-284.

Hemley, R. J., Bell, P. M., and Mao, H. K. (1987) Laser techniques in high-pressure geophysics. *Science*, 237, 605-612.

Herzberg, G. (1966) Molecular spectra and molecular structure. Vol. 2. Infrared and Raman spectra of polyatomic molecules. Chapter 3, D. Van Nostrand Company, Inc., Princeton, New Jersey, New York, 239-369.

Hofmeister, A. M., Xu, J. Mao, H. -K., Bell, P. M., Hoering, T. C. (1989) Thermodynamics of Fe-Mg olivines at mantle pressures: Mid-and far-infrared spectroscopy at high pressure. *American Mineralogist*, 74, 281-306.

Huggins, F. E. (1973) Cation order in olivines: Evidence from vibrational spectra. *Chemical Geology*, 11, 99-109.

Iishi, K. (1978) Lattice dynamics of forsterite. *American Mineralogist*, Vol. 63, 1198-1208.

Karr, Jr. C. (1975) Infrared and Raman spectroscopy of lunar and terrestrial minerals. Academic Press, New York.

Kieffer, S. W. (1985) Heat capacity and Entropy: Systematic relations to lattice vibrations. Chapter 3 in Microscopic to macroscopic, atomic environments to mineral thermodynamics. *Reviews in Mineralogy*, Vol 14, edited by S. W. Kieffer and A. Navrotsky.

Kieffer, S. W. (1985) Heat capacity and entropy: systematic relations to lattice thermodynamic properties. In Microscopic to Macroscopic- Atomic environments to Thermodynamic properties", *Reviews in Mineralogy*, Vol. 14, ed. by S.W. Kieffer and A. Navrotsky, Mineralogical Society of America, Washington, D.C.,65-126.

Klein, C. and Hurlbut, Jr., C.S. (1985) Manual of Mineralogy. 20th John wiely & Sons, New York.

Knittle, E., and Jeanloz, R. (1991) Earth's core-mantle boundary: Results of experiments at high pressures and temperatures. *Science*, 251, 1438-1443.

Krishnan, R. S. (1978) Raman Effect: Discovery and After. National Physical Laboratory, New Delhi.

Kubicki, J.D., Hemley, R.J., and Hofmeister, A.M. (1992) Raman and infrared study of pressure-induced structural changes in $MgSiO_3$, $CaMgSi_2O_6$, and $CaSiO_3$ glasses. *American Mineralogist*, 77, 258-269.

Kudoh, Y. and Takeuchi, Y. (1985) The crystal structure of forsterite Mg_2SiO_4 under high pressure up to 149 kb. *Zeitschrut fur Kristanograpme*, 111, 291-302.

- Lager, G. A., and Meagher, E.P. (1978) High-temperature structural study of six olivines. *Am. Mineral.*, 63, 365-377.
- Lam, P.K., Yu, R., Lee, M.W. and Sharma, S.K. (1990) Relationship between crystal structure and vibrational mode in Mg_2SiO_4 . *American Mineralogist*, 75, 109-119.
- Lazerev, A. N. (1972) Vibrational spectra and structure of silicates, Consultants Bureau: New York.
- Levien, L. and Prewitt, C. T. (1981) High-pressure structural study of diopside. *American Mineralogist*, 66, 315-323.
- Lumkin, G. R., Ribbe, P. H. and Lumpkin, N. E. (1983) Composition, order-disorder and lattice parameters of olivines: determinative methods for Mg-Mn and Mg-Ca silicate olivines. *American Mineralogist*, 68, 1174-1182.
- Matson, D. W., Muenow, D. W., and Garcia, M. O. (1984) Volatiles in amphiboles from xenoliths, Vulcan's Throne, Grand Canyon, Arizona USA. *Geochim Cosmochim Acta* 48, 1629-1636.
- Matsui, M. and Busing, W. R. (1984) Calculation of the elastic constants and high-pressure properties of diopside, $CaMgSi_2O_6$. *American Mineralogist*, 69, 1090-1095.
- McMillan, P. (1985) Vibrational Spectroscopy in the mineral sciences. *Reviews in Mineralogy*, Vol. 14, Microscopic to Macroscopic Atomic Environments to Mineral Thermodynamics. Ed. S.W. Kieffer & A. Navrotsky. Mineralogical Society of America.
- McMillan, P., and Akaogi, M. (1987) Raman spectra of β - Mg_2SiO_4 (modified spinel) and c- Mg_2SiO_4 (spinel). *Am. Mineral.* 72, 361-364.
- McMillian, P. (1984) Structural studies of silicate glasses and melts applications and limitations of Raman Spectroscopy. *American Mineralogist*, 69, 622-644.
- McMillian, P. F. and Hofmeister, A. M. (1988) Infrared and Raman spectroscopy. Chapter 4 in *Spectroscopic methods in mineralogy and geology*. *Reviews in Mineralogy*, Vol. 18. Edited by Frank C. Hawthorne, Mineralogical Society of America.
- Montana, A. and Griffin, W. L. (1986) Crystal chemistry of two coexisting K-richterites from St. Marcel (Val d'Aosta, Italy). *Am. Mineral.* 71, 1426-1433.
- Newton, R. C. and Wood, B. J. (1980) Volume behavior of silicate solid solutions. *American Mineralogist*, Vol. 65, 733-745.
- Paques-Ledent, M. Th. and Tarte, P. (1973) Vibrational studies of olivine-type compounds-I. The i.r. and Raman spectra of the isotopic species of Mg_2SiO_4 . *Spectrochimica Acta*, Vol. 29A, 1007-1016.

Pathak, K. N. (1965) Theory of anharmonic crystals. Physical Review, Vol. 139, No. 5A, 1569.

Pirou, B. and McMillian, P. (1983) The high frequency vibrational spectra of vitreous and crystalline orthosilicates. American Mineralogist, 68, 426-443.

Price, G.D., and Parker, S.C. (1984) Computer simulations of the structural and physical properties of the olivine and spinel polymorphs of Mg_2SiO_4 . Phys Chem Minerals, 10b, 209-216.

Price, G.D., Parker, S.C., and Leslie, M. (1987) The lattice dynamics of forsterite. Mineralogical Magazine, 51, 157-170.

Raman, C. V. and Krishnan, K. S. (1928) A new type of secondary radiation. Nature, March, Vol. 121, 501-502.

Rao, D. R., Chaplot, S. L., Choudhury, N., Ghose, S., and Price, D. L. (1987) Phonon density of states and specific heat of forsterite, Mg_2SiO_4 . Science, 236, 64-65.

Raudsepp, M., Turnock, A. C., Hawthorne, F. C., Sheriff, B. L., Hartman, J. S. (1987) Characterization of synthetic parasitic amphiboles ($NaCa_2Mg_4M^{3+}Si_6Al_2O_{22}(OH,F)_2$; M^{3+} = Al,Cr, Ga,Sc In) by infrared spectroscopy, Revised structure refinement, and ^{27}Al , ^{29}Si , and ^{19}F MAS NMR spectroscopy. Am Mineral 72:580-593.

Richards, W. G. and Scott, P. R. (1985) Structure and Spectra of Molecules. Chapter 1 and Chapter 5. John Wiley & Sons, Chichester.

Robert Jean-Louis, and Kodama, H. (1988) Generalization of the correlations between hydroxyl-stretching wave number and composition of Micas in the system $K_2O-MgO-Al_2O_3-SiO_2-H_2O$: A single model for trioctahedral and dioctahedral micas. Am J Science 288-A, 196-212.

Robert Jean-Louis, Ventura, G. D., Thauvin Jean-Jouis (1989) The infrared OH-stretching region of synthetic richterites in the system $Na_2O-K_2O-CaO-MgO-SiO_2-H_2O-HF$. Eu. J. Mineral. 1, 203-211.

Rossi, G., Smith, D. C., Ungaretti, L., and Domeneghetti, M. C. (1983) Crystal-chemistry and cation ordering in the system diopside-jadeite: A detailed study by crystal structure refinement. 83, 247-458.

Rossmann, G. R. (1980) Pyroxene Spectroscopy. Chapter 3 in Reviews in Mineralogy, Vol. 7, Pyroxenes, Ed. by Charles T. Prewitt, Mineralogical Society of America, 93-115.

Sekita, M., Ohashi, H., and Terada, S. (1986) Raman spectroscopic study of clinopyroxenes in the system CaScAlSiO₆-CaAl₂SiO₆. *Phys Chem Minerals*, 17, 149-156.

Servoin, J. L. and Piriou, B. (1973) Infrared reflectivity and Raman scattering of Mg₂SiO₄ single crystal. *Physica Status Solidi (b)*, Vol. 55, 677-686.

Servoin, J. L. and Piriou, B. (1973) Infrared reflectivity and Raman scattering of Mg₂SiO₄ single crystal. *Phys. Stat. Sol. (b)* 55, 677-686.

Sharma, S. K. (1990) Applications of Raman spectroscopy in earth and planetary sciences. Reprinted from *Mantle to Meteorites*, Edited by K. Gopalan, Vinod K. Gaur, B. L. K. somayajulu and J. D. Macdougall, Indian Academy of Sciences, Bangalore, India.

Sharma, S. K., and Urmos, J.P. (1987) Micro-raman spectroscopic studies of materials at ambient and high pressures with CW and pulsed lasers. San Francisco.

Sharma, S. K. and Simons, B. (1981) Raman study of crystalline polymorphs and glasses spodumene composition quenched from various pressures. *American Mineralogist*, 66, 118-126.

Sharma, S.K. and Urmos, J.P. (1987) Micro-Raman spectroscopic studies of materials at ambient and high pressures with cw and pulse lasers. In Roy H. Geiss (ed.), *Microbeam Analysis*, San Francisco Press Inc, 113-136.

Sharma, S. K., Mao, H. K., Bell, P. M., and Xu, J. A. (1985) Measurement of stress in diamond anvils with micro-Raman Spectroscopy. *J. Raman Spectroscopy*, 16, no.5, 350-351.

Sharma, S. K., Pandya, N., and Muenow, D. W. (1988) Calibration of a multichannel micro-Raman Spectrograph with plasma lines of argon and Krypton ion lasers. *Microbeam Analysis*, Newbury, D.E., Ed. San Francisco Press, Inc., San Francisco, CA. 171-174.

Skogby, H and Rossman, G. R. (1991) The Intensity of amphibole OH bands in the infrared absorption spectrum. *Phys Chem Minerals*, 1864-1868.

Skogby, H. and Rossman, G. R. (1991) The intensity of amphibole OH bands in the infrared absorption spectrum. *Phys Chem Minerals*, 18, 64-68.

Smyth, J. R. (1969) Orthopyroxene-high-low clinopyroxene inversions. *Earth and planetary science letters*, 6, 406-407.

Smyth, J.R. (1971) Proto-enstatite: a crystal-structure refinement at 1100C. *Zeitschrift Fur Kristallographie*, Bd. 134, S. 262-274.

Sterns, R. G., (1974) The common chain, ribbon, and ring silicates. Chapter 14 in The infrared spectra of minerals Ed. by V. C. Farmer, Mineralogical Society, 41 Queen's Gate, London, SW7 5HR, 305-330.

Sueno, S., Cameron, M., and Prewitt, C. T. (1976) Orthofeerosilite: high temperature crystal chemistry. American Mineralogist, 61, 38-53.

Symth, J. R. and Hazen, R. M. (1973) The crystal structures of forsterite and hortonolite at several temperatures up to 900 0C. American Mineralogist, Vol. 58, 588-593.

Tarte, P. (1963) Etude infra-rouge des orthosilicates et des orthogermanates-II Structures du type olivine et monticellite. Spectrochimica Acta, Vol. 19, pp 25-47.

Tomisaka, T. and Iishi, K. (1980) Some aspects of the lattice dynamics of diopside. Mineralogical Journal, 10, no.2, 84-96.

Veblen DR (1981) Amphiboles and other hydrous pyroboles -Mineralogy in Reviews in Mineralogy Volume 9A. Series Editor Ribbe, Paul, H. Mineralogical Society of America.

Ventura, G. D., Robert Jean-Louis, Beny, and Jean-Michael (1991) Tetrahedrally coordinated Ti⁴⁺ in synthetic Ti-rich potassic richterite: Evidence from XRD, FTIR and Raman Studies. Am Mineral 76, 1134-1140.

Vogt. H. (1987) Soft-mode spectroscopy in ferroelectrics by hyper-raman scattering.

Volfinger, M., Robert, J. L., Vielzeuf, D., Neiva, A. M. R (1985) Structural control of the chlorine content of OH-bearing silicates (mica and amphiboles). Geochim Cosmochim Acta 49, 37-48.

Wang A., Dhamelincourt, P., Turrell, G. (1988) Infrared and Low temperature micro-Raman spectra of the OH stretching vibrations in cummingtonite. Appl Spectrosc. 42, No. 8, 1451-1457.

Wang, A., Dhamelincourt, P., Turrell, G. (1988) Raman Micro spectroscopic Study of the cation Distribution in Amphiboles. Appl Spectrosc 42, No. 8, 1441-1450

Warner, R. D., and Luth, W. C. (1973) Two-phase data for the join monticellite (CaMgSiO₄)-forsterite (Mg₂SiO₄): Experimental results and Numerical analysis. Am. Mineral, 58, 998-1008.

White, W. B. (1975) Structural interpretation of Lunar and Terrestrial Minerals by raman Spectroscopy, in Infrared and Raman spectroscopy of Lunar and terrestrial minerals, Ed. by Clarence Karr, Jr., Academic Press, New York, 299-358.

White, W. B. (1974) Order-disorder effects. The Infrared Spectra of Minerals. Farmer, V. C., Ed. in Mineralogical Society Monograph 4, 87-110.

Winter, J. K., Ghose, S., and Okamura, F. P. (1977) A high temperature study of the thermal expansion and the anisotropy of the sodium atom in low albite. American Mineralogist, Vol. 62, 921-931.

Xu, J. A., Mao, H. K., and Bell, P. M. (1986) High-pressure ruby and diamond fluorescence: Observations at 0.21 to 0.55 Terapascal. Science, Vol. 232, 1404-1406.

Xu, J. A., Mao, H. K., Bell, P. M. (1986) High-pressure ruby and diamond fluorescence: Observations at 0.21 to 0.55 terapascal. Science, 232, 1404-1406.